Optoelectronic Properties of InP/AlGaInP Quantum Dot Laser Diodes

by

Mohammed Saad Al-Ghamdi

Cardiff University

a thesis for the degree of Doctor of Philosophy

in the School of Physics and Astronomy

December 2009

Acknowledgements

All gratitude is due to ALLAH the Almighty who aided me to complete this work. He says in the Holy Quran (*and above every one possessed of knowledge is the All-knowing one*) 12:76.

I would like to express my gratitude towards my supervisors Professor Peter Blood and Professor Peter Smowton for all their enthusiasm, advice and for supporting and guiding me through this work.

Thanks also must go to Drs Gareth Edwards, Angela Sobiesierski and Ian O' Driscoll for supporting me through some of the theoretical part of this work and they were very helpful with their experimental skills.

Thanks to all members of the optoelectronics group for the friendly and supportive working environment. Thanks goes also to all my colleagues in the School of Physics and Astronomy for their extremely welcoming and supportive environment.

I would like to express my deepest gratitude to my family for their love and support and I dedicate my work to them.

Abstract

The aim of this thesis is to understand and optimise the optoelectronic properties of InP quantum dot laser diodes which operate in the range around 730*nm* required for various application such as the photodynamic therapy. The properties of wafers with two barrier widths, 8 and 16*nm*, each grown at different temperatures, 690, 710, 730 and 750°*C*, and consisting of 5 layers of dots forms from different quantity of deposited material, 2, 2.5 and 3*ML*, are described and investigated. The laser and multisection devices of these structures are used to determine threshold current density, lasing wavelength, modal absorption, modal gain and spontaneous emission spectra.

The modal absorption spectra show three different dot size distributions, small, large and very large dots. Their variation with growth temperature results in a blue shift accompanied by an increasing number of states while the variation with quantity of deposited material shows only an increase to the number of states. The lasing wavelength variation with growth temperature covers a range between 715-745*nm*. The threshold current density as a function of temperature for 2000μm long laser devices grown at temperature of 750°*C* exhibits a distinctive dependence on the operating temperature and becomes less pronounced when the growth temperature reduces. This is explained in terms of the carrier distributions in the quantum dot and quantum well states without invoking an effect from Auger recombination.

The optimisation of threshold current density can be reached by using structures with higher barrier width grown at low temperature and deposited with high quantity of quantum dot material to minimise both the affect of the very large dot, which contain a number of defects associated with them, and carrier leakage from quantum dot to quantum well states. This reduces the room temperature threshold current density to 150$A.cm^{-2}$ for 2*mm* long lasers with uncoated facets.

Contents

CHAPTER 2

Principles of Semiconductor Quantum Dot Lasers

2.1 Introduction

This chapter gives a general overview of the physical principles of semiconductor quantum dot lasers. The chapter starts by introducing some concepts of semiconductors including bandstructure, the Fermi-Dirac distribution and density of states. The chapter then describes the fundamentals of lasers such as emission, absorption, population inversion, the feedback process and threshold conditions. The chapter then outlines some physical properties of semiconductor lasers such as optical gain, gain-current relations and separate confinement heterostructures. The chapter then describes the quantum dot system outlining its nature, self-assembled formation and broadening of spectra. The chapter next describes recombination in quantum dots including modal gain, absorption, spontaneous emission and nonradiative recombination. The chapter finishes with the quantum dot properties including carrier distribution and gain-current relation.

2.2 Some Concepts of semiconductors

This section considers some concepts of semiconductors which are necessary to understand the behaviour of carriers within semiconductor devices.

2.2.1 Semiconductor Bandstuctures

The energy bandstructure of the electrons is controlled by the semiconductor crystals in which their atoms are connected by covalent bonds. The carriers of the connected atoms can occupy a number of energy states depending on the number of these atoms. This means that if there are N atoms connected to each other then a band of N energy states will be formed for each energy level. These energy bands fall into two groups, one of them is determined when the carriers are with free energy which representing the higher level and the other is determined when the carriers are tightly bound to the atomic nuclei of the material which represent the lower level [1].

The two most significant bands are the valence band and the conduction band. The valence band will be full in all of its states while the conduction band will be empty in all of its states if the temperature is equal to zero K. Adding thermal energy or any other energy to the system will excite the electrons from the valence band to the conduction band creating holes in the valence band and electrons in the conduction band. Any transition of electrons from the conduction band to the valence band is controlled by the conservation of energy and momentum. This can be illustrated on the plot of electron energy E versus wavenumber vector k for a

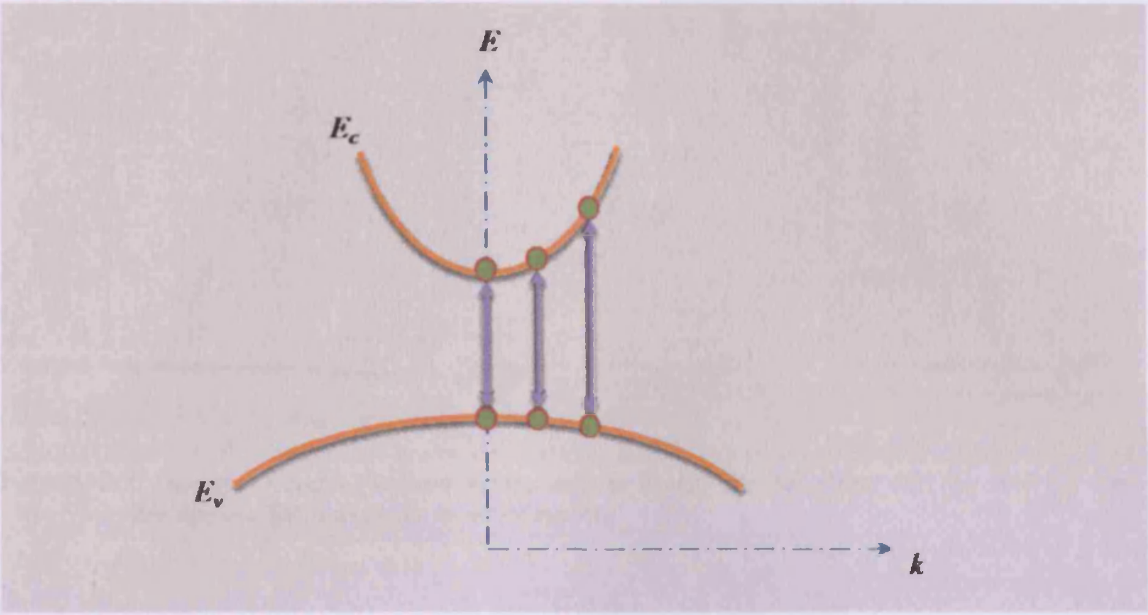

Figure 2.1 *Plot of electron energy verses wavenumber vector in semiconductor materials showing only vertical transitions between valence and conduction bands.*

semiconductor materials, which is shown in Figure 2.1. When the incident photon interacts with an electron it has very small momentum which can be negligible compared with electron momentum [1]. This means the transition between the conduction band and valence band must have the same wavenumber vector *k*, so the only transitions that appear on this diagram are the vertical transitions as shown in Figure 2.1.

2.2.2 Fermi-Dirac Distribution

In order to understand how the carriers fill the energy states in a semiconductor, the state occupation probability $f(E)$ at a given energy E should be known. The Fermi- Dirac distribution [1] shown in Equation 2.1 is the appropriate function for electrons in solids such as semiconductors.

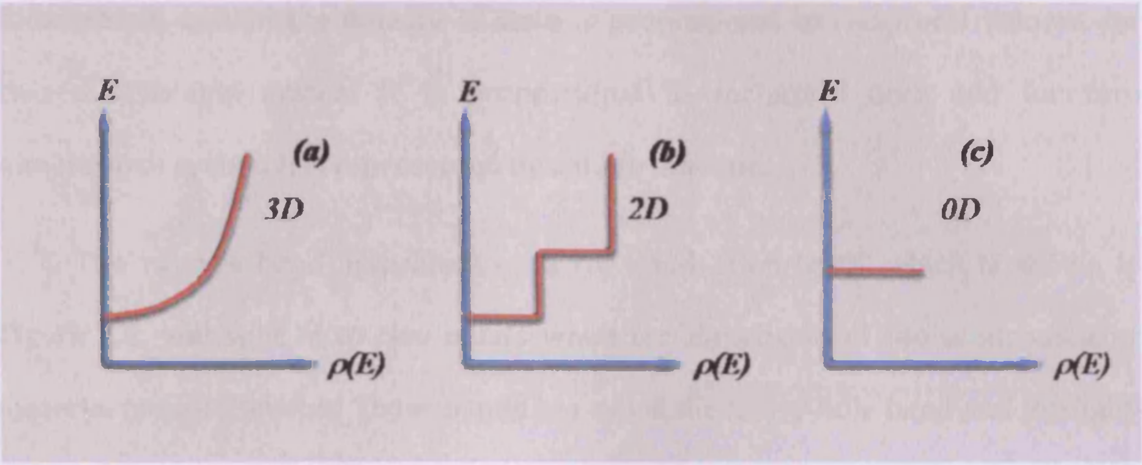

Figure 2.2 *Density of states function verses carrier energy for (a) three, (b) two and (c) zero-dimensional semiconductor material systems.*

$$f(E) = \frac{1}{e^{(E-E_f)/kT} + 1} \tag{2.1}$$

where E is the energy of the carrier, E_f is the Fermi energy, k is the Boltzmann constant and T is the temperature. When $E = E_f$ the probability $f(E)$ is equal to one-half.

2.2.3 Density of States in Semiconductors

The density of states $\rho(E)$ at any particular energy E is defined as the number of electronic states per unit volume per unit energy. It is a significant parameter for calculating the distribution of electrons and holes in the conduction and valence bands. This is important for understanding the optical properties of a semiconductor material such as absorption and gain.

The density of state function verses state energy is shown in Figure 2.2 for three, two and zero-dimensional semiconductor material systems. For three dimensional system the density of state is proportional to reciprocal volume, for two dimensional system it is proportional to reciprocal area and for zero dimensional system it is represented by a delta function.

The valence band associated with the conduction band, which is shown in Figure 2.2, will split in to two bands when the dimension of the semiconductor material became smaller. These bands are called the heavy-hole band and the light-hole band. The heavy-hole is the only considered case in the valence band.

2.3 Fundamental of Lasers

This section describes the fundamentals of laser operation, considering the optical transitions which take place in two level systems in general. The section also describes the conditions at which lasing will occur.

2.3.1 Emission and Absorption

There are three processes that take place within the atom associated with the interaction between photons and electrons. These processes are called absorption, spontaneous emission and stimulated emission. They depend on the incident photon energy $h\nu$ and the difference between the two energy levels that the electrons could move between, E_h - E_l and they relate to each other according to conservation of energy as shown in Equation 2.2.

$$E_h - E_l = h\nu \tag{2.2}$$

In the absorption process the energy of the incident photon will be absorbed by an electron, which has a lower energy state E_l. This will make the electron move from that energy state to a higher energy state E_h. This can be seen in Figure 2.3(a) as movement from E_l to E_h. In the spontaneous emission process the electron in a higher energy state E_h can lose its energy, after a certain time, and move to a lower energy state E_l. This loss of energy will come out as a photon with energy of $h\nu$. This can be seen in Figure 2.3(b) as movement from E_h to E_l. In the stimulated emission process the incident photon triggers the electron, which is in a higher energy state E_h, into emitting a photon with energy of $h\nu$. As a result of this process the electron

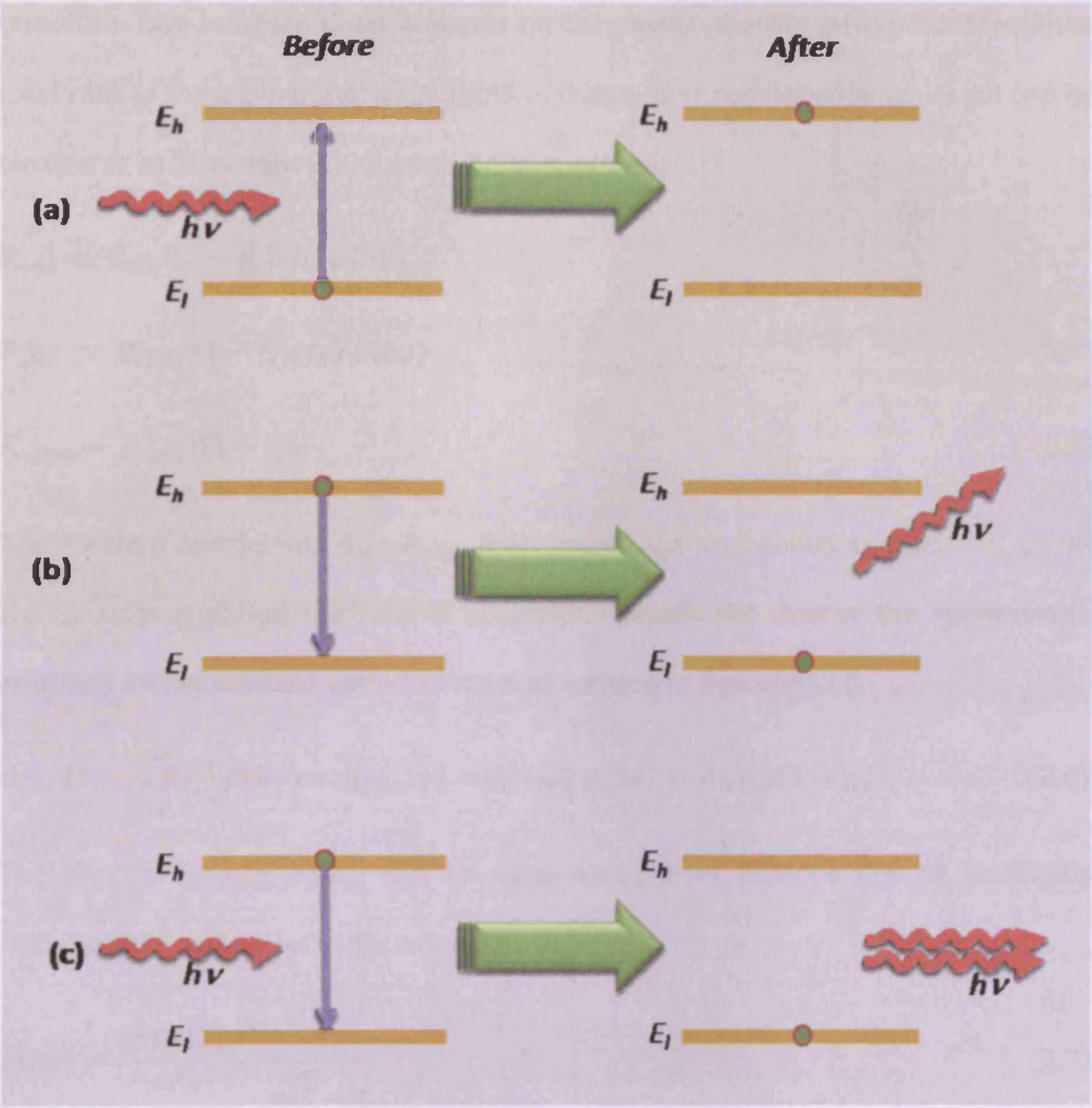

Figure 2.3 *Energy level diagram showing the three processes which occur in the atom due to the interaction between photons and electrons. (a) absorption, (b) spontaneous emission and (c) stimulated emission.*

moves in to a lower energy state E_l and two emitted photons have the same direction, frequency and phase. This can be seen in Figure 2.3(c).

Each of these processes occurs at a certain rate that depends upon a constant which is called Einstein coefficient, the population of the states is f_l, f_h and the transition rate between them depends on the photon density $\rho(h\upsilon)$. Therefore the total rate of the absorption, stimulated emission and spontaneous emission can be written as in Equations 2.3, 2.4 and 2.5 respectively.

$$R_{abs} = B_{abs}\,(1 - f_h)(f_l)\,\rho(h\upsilon) \tag{2.3}$$

$$R_{stim} = B_{stim}\,(1 - f_l)(f_h)\,\rho(h\upsilon) \tag{2.4}$$

$$R_{spon} = A\,(f_h)(1 - f_l) \tag{2.5}$$

The Einstein coefficients B_{abs}, B_{stim}, A are called the probability coefficients. In the steady state situation the rate of absorption equals the sum of the spontaneous emission and stimulated emission rates as written in Equation 2.6.

$$B_{abs}\,(1 - f_h)(f_l)\,\rho(h\upsilon) = B_{stim}\,(1 - f_l)(f_h)\,\rho(h\upsilon) + A\,(f_h)(1 - f_l) \tag{2.6}$$

The photon density $\rho(h\upsilon)$ can be determined from Planck's law of blackbody radiation [2] as written in Equation 2.7.

$$\rho(h\upsilon) = \frac{8\pi n^3 (h\upsilon)^2}{h^3 c^3} \frac{1}{e^{\frac{h\upsilon}{kT}} - 1} \tag{2.7}$$

where n is the refractive index and c the speed of light. The Einstein coefficients A and B can be related to each other by comparing Equations 2.6 and 2.7. It can be shown that $B_{abs} = B_{stim} = B$ and

$$A = \frac{8\pi n^3 (h\upsilon)^2}{h^3 c^3} B \tag{2.8}$$

The increase of the stimulated emission rate will cause an amplification of light within the cavity of the laser medium. This can be done by increasing the photon density, which makes the stimulated emission rate greater than spontaneous emission rate, and by making electrons in the higher state more than electrons in the lower state, which makes the stimulated emission rate greater than absorption rate, this called population inversion.

2.3.2 Population Inversion and Feedback Process

The population inversion can be created if there are more electrons in the higher state than the lower state. This means that the rate of the stimulated emission is higher than the absorption rate. In semiconductors the two level system that is shown in Figure 2.3 is replaced by two energy bands. The higher level is the conduction band and is normally almost empty of electrons. The lower level is the valence band and is normally almost full of electrons. Population inversion in semiconductor occur when the number of electrons in the conduction band increases and the number of electrons in the valence band decreases. This can be done by using a forward biased p-n junction.

The photon energy density has to be increased or the net stimulated emission rate has to be greater than spontaneous emission rate in order to have an amplification of light within the cavity of the laser medium along with the population inversion. The method that used to do so is called optical feedback. Some percentage of the generated photons are fed back into the laser medium. This can be done by using two mirrors, one at each end of the cavity. The optical feedback in the cavity of the semiconductor laser medium can be achieved by creating partially reflecting mirrors formed from the refractive index difference

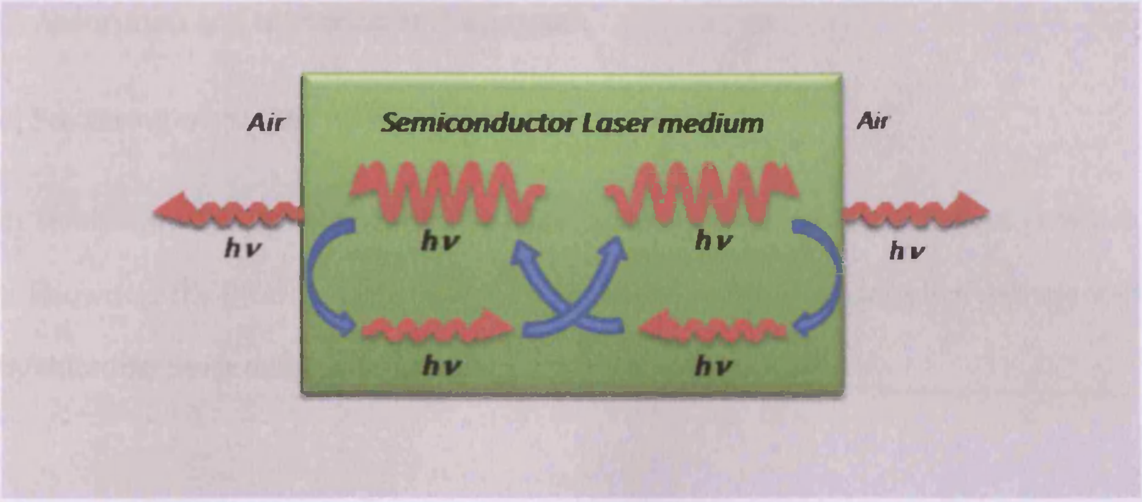

Figure 2.4 *Schematic diagram of semiconductor laser medium with refractive index different from the refractive index of the air causing loss and reflection of light at each interface between them.*

at the interface between the laser medium and the air as shown in Figure 2.4. The percentage of reflected light from a given mirrors is called the reflectivity of the mirrors *R*. It depends upon the refractive index of the two media that create these mirrors, n_1, n_2 and represented by Equation 2.9.

$$R = \frac{(n_1 - n_2)^2}{(n_1 + n_2)^2} \tag{2.9}$$

where n_1 is for the semiconductor material and n_2 is for the air which equal to one.

2.3.3 Threshold Condition

The threshold condition for laser action in the medium is reached when the value of modal gain within the cavity matches the value of the total cavity loss. The total cavity loss of the system is due to the following reasons:

a) Transmission at the mirrors.

b) Absorption and scattering at the mirrors.

c) Scattering within the waveguide.

In semiconductor lasers the third reason is represented by the coefficient α_i which is known as the internal optical mode loss while the other reasons are represented by the reflectivity of the mirrors R.

2.4 Semiconductors Lasers

The section describes a laser made of semiconductor materials and derives a relationship between the cavity length, which is the actual length of the laser device, and the gain required for laser action. The section also describes the confinement of the light and carriers within these semiconductor materials.

2.4.1 Optical Gain in Semiconductor Lasers

The gain in semiconductor lasers occurs when the stimulated emission rate is greater than absorption rate and for coherent emission the stimulated emission rate must be greater than the spontaneous emission rate within the laser cavity. Therefore optical feedback and population inversion are necessary. The optical gain at threshold should match the optical loss. This optical loss is caused by the mirrors reflectivity R and by the internal optical scattering process at rate α_i per unit length. In Figure 2.5 the initial intensity of light which produced by spontaneous emission is I_0, when this light reaches the first edge of the laser medium it will have an intensity of I_1. When the light reflected from mirror at the first edge of the laser medium it will have an intensity of I_2. When the light reaches the second edge of the laser medium it will have an intensity of I_3. When the light is reflected from the mirror at the second edge of the laser medium it will have an intensity of I_4 which is given in Equation 2.10.

$$I_4 = R^2 I_0 \exp[2(G_{th} - \alpha_i)L_c] \tag{2.10}$$

where G_{th} is the modal gain at threshold. For a conserved coherent emission $I_4 = I_0$,

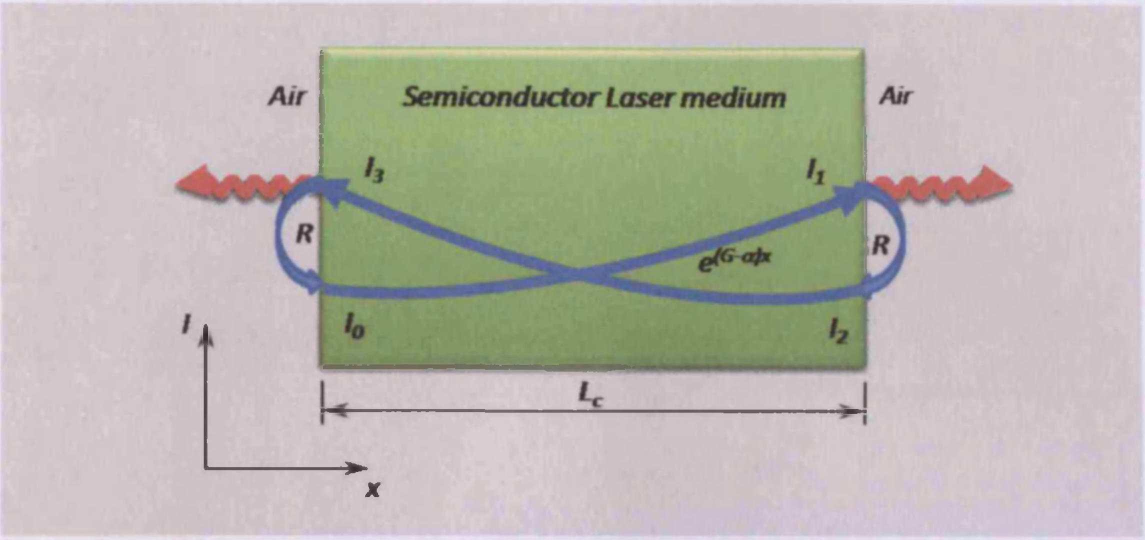

Figure 2.5 *Schematic diagram of the optical intensity in a semiconductor laser medium with cavity length of L_c and reflectivity R.*

Equation 2.10 can be written as

$$1 = R^2 \exp[2(G_{th} - \alpha_i)L_c] \tag{2.11}$$

Rearranging Equation 2.11, the threshold modal gain can be written as

$$G_{th} = \alpha_i + \frac{1}{L_c}\ln(R^{-1}) \tag{2.12}$$

Figure 2.6 shows the spontaneous emission spectra and absorption/gain spectra at two quasi-Fermi level separations, ΔE_{f1}, ΔE_{f2}, for a semiconductor. It shows that the increasing of quasi-Fermi level separation will cause the bands to be filled with more carriers and the curve of r_{spon} will expanded. For photon energy less than quasi-Fermi level separation there will be a population inversion in the semiconductor material which will provide an optical gain whereas at higher photon energy the semiconductor material will absorb the light. The increasing of

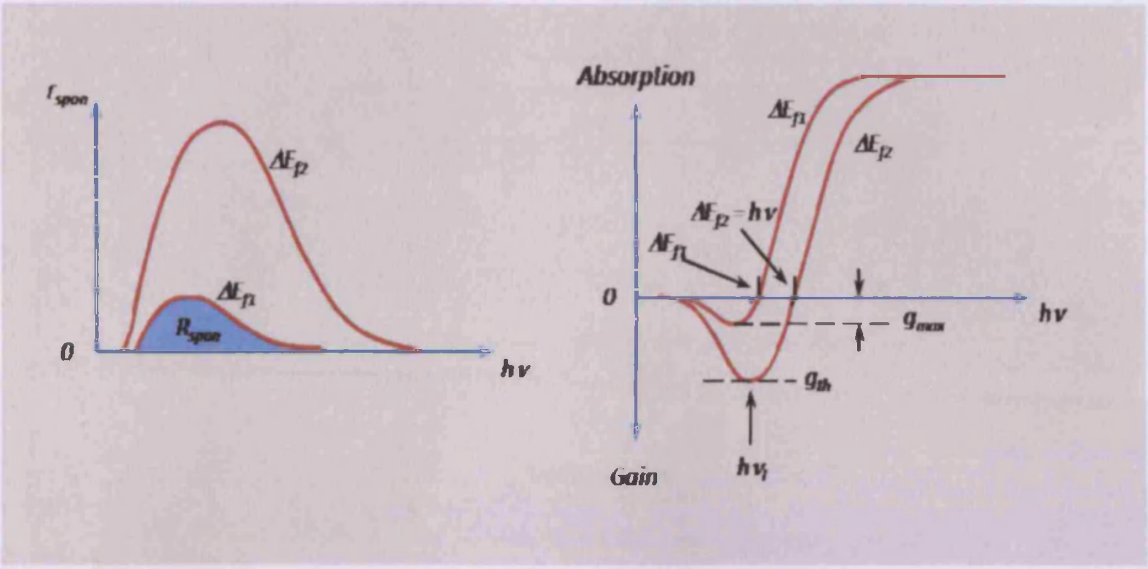

Figure 2.6 *The spontaneous emission and absorption/gain spectra illustration at two quasi-Fermi level separations for a semiconductor.* [3]

quasi-Fermi level separation will make the gain expanded over a range of photon energy and cause an increase to the peak gain g_{max} which called the material gain. This can reach the lasing point at photon energy $h\upsilon_l$ when the peak gain reaches g_{th} which called the threshold local gain [3].

2.4.2 Separate Confinement Heterostructure

The lasers constructed with a double heterostructure have improved the confinement of the carriers and photons. It is more effective than the lasers which only consist of the p-n junction because it can keep the photons in the same region as the carriers. It consists of two different semiconductor materials, one with low bandgap energy and the other with high bandgap energy. The separate confinement heterostructure is used to optimise the confinement of the carriers and the optical field within the laser. It is different from the double heterostructure which has 3

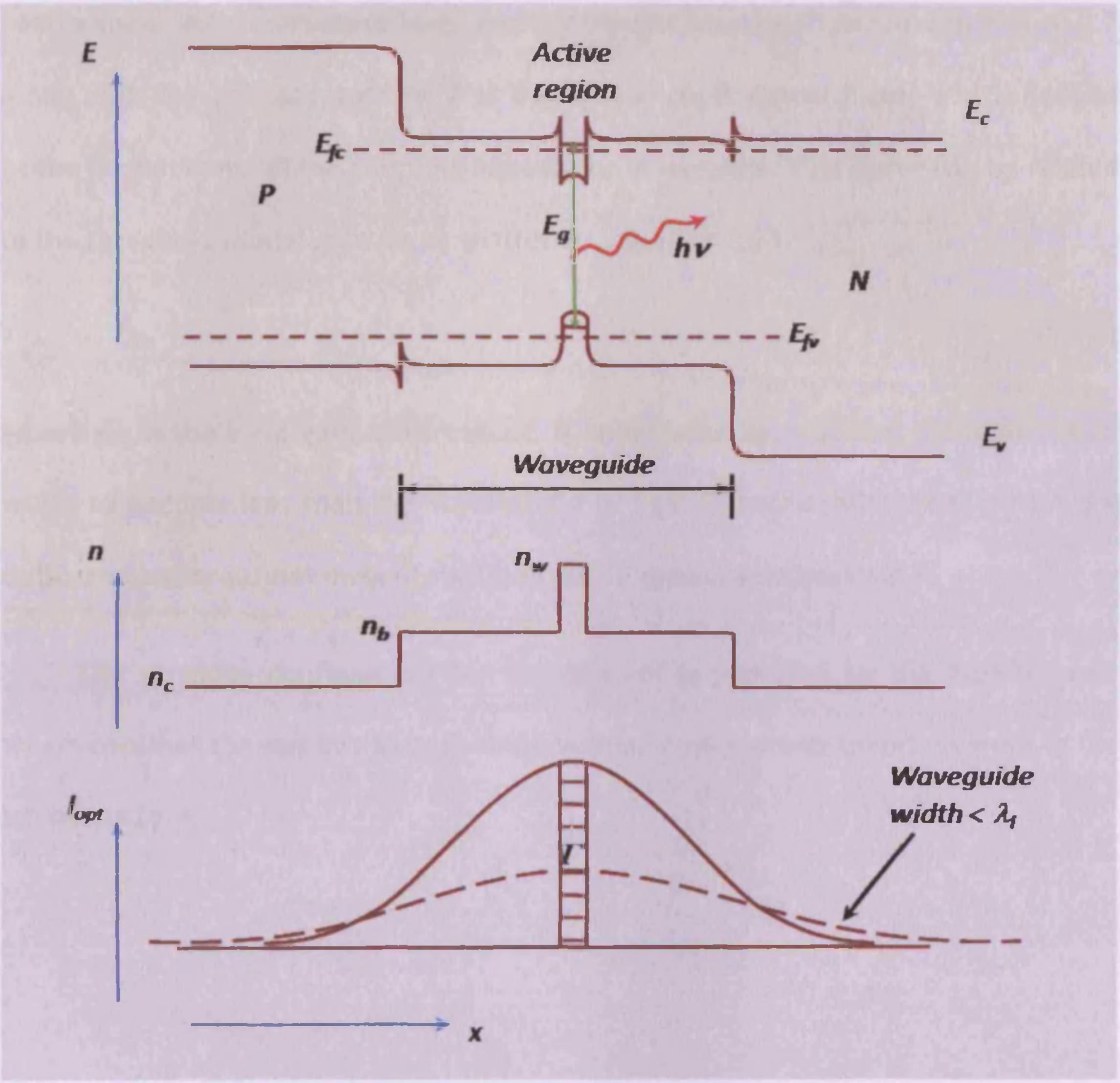

Figure 2.7 *Diagram illustrating the energy bandgaps, refractive index profiles and optical intensity for a separate confinement heterostructure under forward bias.*

layers of semiconductor material. It has 5 layers as seen in Figure 2.7. This means that on each side of the active region there will be two bandgap steps representing two different regions. These different regions are required to confine effectively the carriers and the optical field.

The energy bandgaps and the refractive index profiles for a separate confinement heterostructure laser under forward bias are illustrated in Figure 2.7 along with the optical intensity. Γ is the optical confinement factor which defined as the proportional of the coupling light to the waveguide. This factor can be related to the threshold modal gain G_{th} as written in Equation 2.13.

$$\Gamma g_{th} = G_{th} \tag{2.13}$$

where g_{th} is the local gain at threshold. It shows that by reducing the active layer width to become less than the wavelength of light in semiconductor material, the optical intensity cannot be well confined which means a decrease in Γ.

The separate confinement for the carriers is provided by the middle layer which confines the carriers to very small volume and to create quantum wells in the bandstructure.

2.5 Quantum Dot System

This section describes quantum dot systems by studying their nature and underlying physics. The section also describes how these dots form and discusses advantages and disadvantages of using quantum dots. The section ends by describing one of the main disadvantages in quantum dot systems, which is the broadening.

2.5.1 The Nature of Quantum Dots

Quantum dots can be described as the confinement of the carriers in all three spatial dimensions to a very small region, which has a scale of 1–10nm. These dimensions are smaller than the de-Broglie wavelength of the electrons. This means that the electronic states are confined within these quantum dots causing high discrete energy levels [4] as shown in Figure 2.2. The energy levels obtained by solving the Schrödinger equation for the electron within rectangular box with infinitely high potentials in all three directions are given by Equation 2.14.

$$E_{n_x,n_y,n_z} = \frac{\hbar^2\pi}{2m^*}\left[\left(\frac{n_x}{l_x}\right)^2 + \left(\frac{n_y}{l_y}\right)^2 + \left(\frac{n_z}{l_z}\right)^2\right] \tag{2.14}$$

where n_x, n_y, n_z are a positive numbers, l_x, l_y, l_z are the length of the rectangular box and m^* is the effective mass of the electron. In an ideal quantum dot the electron is localized and it has a standing wave inside the dot. The energy level separation given by Equation 2.14 is increased when the lengths of the rectangular box decrease. This has an advantage of reducing the unwanted thermal population to

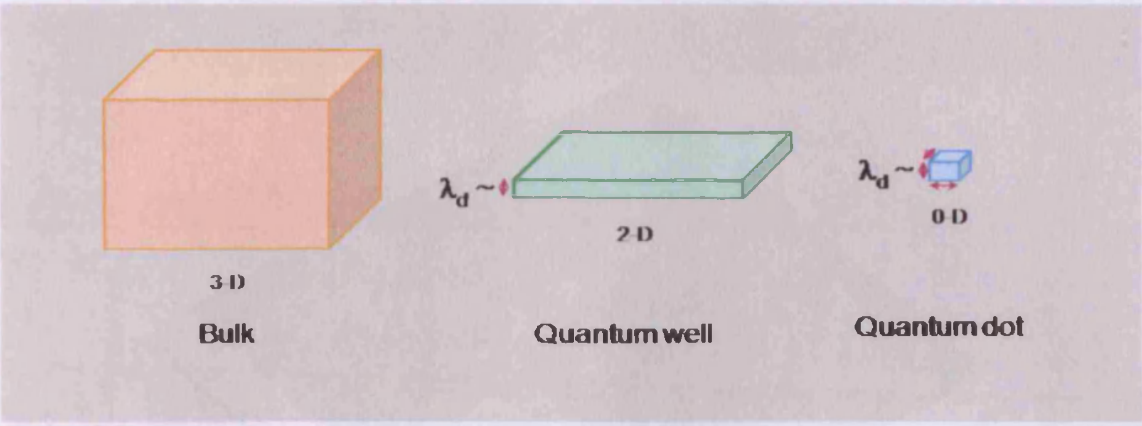

Figure 2.8 *Diagram illustrating the quantum confined structures.*

higher states. The widely spaced discrete density of states produce sharp absorption and emission spectra but in practice this does not appear due to homogeneous and inhomogeneous broadening which will be discussed later in this section.

The carriers in quantum dots are confined in three dimensions as shown in Figure 2.8. This will improve some of physical properties because the energy range over which the carriers are distributed is decreased due to the higher confinement. The improvement in physical properties that can be observed include low threshold current density, high differential gain, narrower band width and temperature insensitivity of the lasing threshold current density.

2.5.2 Self-Assembled Quantum Dots

There are several methods available to form quantum dots. One of these methods is the Stranski-Kranstanow Self-Assembled growth technique which is commonly used. It was proposed by Tabuchi et. al. in 1992 [5] and it can be

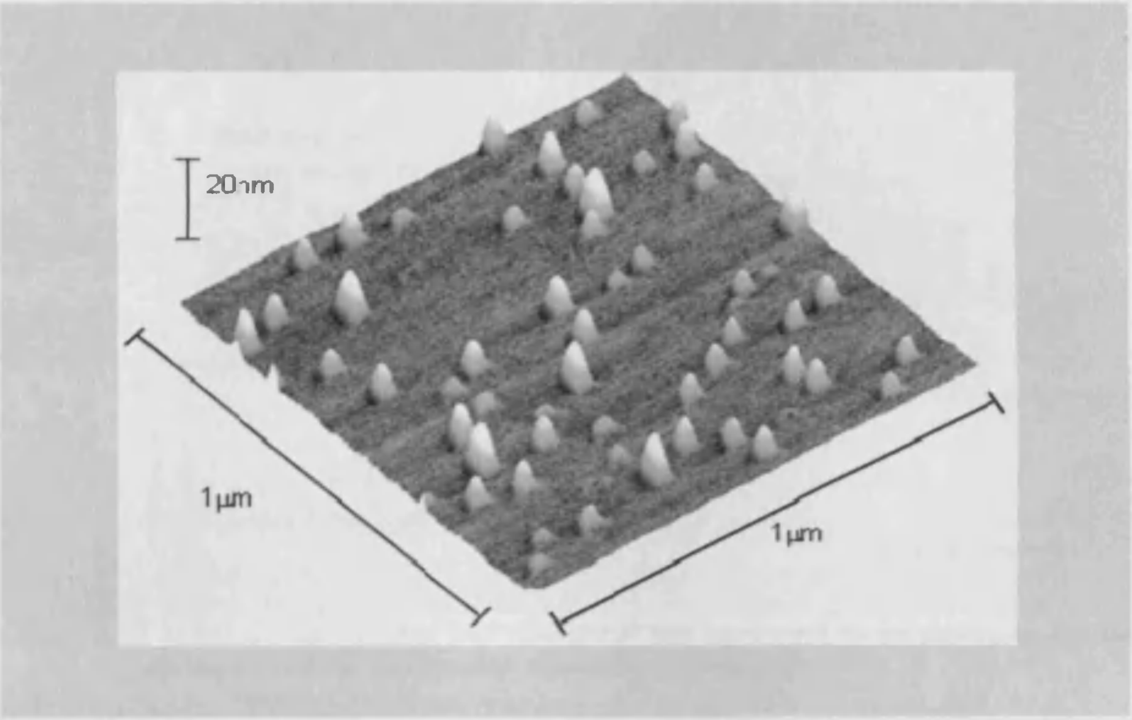

Figure 2.9 *AFM image of uncapped InP QDs grown on AlGaInP at 690 °C.* [7]

described as the growth of a semiconductor material layer on top of another one which has a slightly smaller lattice constant than the top one. This growth technique has the ability to grow a strained layer of semiconductor material on top of another one. The top semiconductor layer starts to buckle due to the stress of having the lattice constant slightly different in size between the top and the bottom semiconductor materials [6]. The size, shape and material composition are different from one dot to another. This is due to the difficulty in controlling the growth conditions of the quantum dots. Some growth conditions can have an effect on the size, density and material composition of the dots in general and these are the width of the layers between the dots, the growth temperature and the quantity of material deposited.

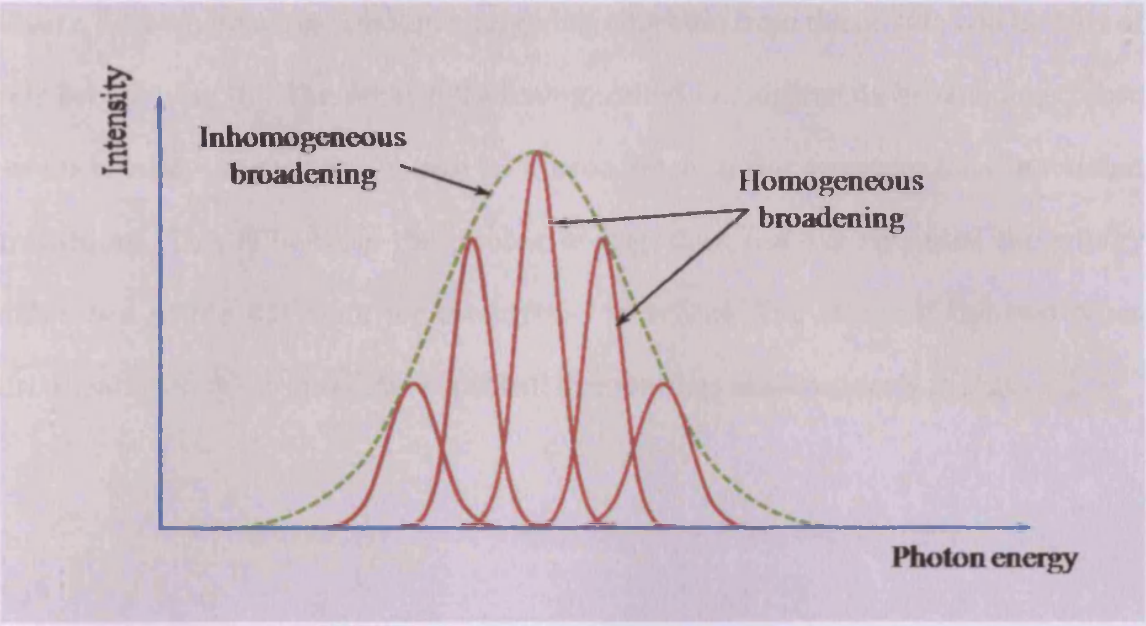

Figure 2.10 *Emission from individual and from overall dots represented by the continuous and the dashed line respectively caused by broadening in QD system.*

The quantum dot structures are usually grown by Molecular Beam Epitaxy (MBE) or Metal-Organic Vapour Phase Epitaxy (MOVPE). The structures described in this thesis were grown by MOVPE which is discussed in detail in the next chapter.

2.5.3 Broadening in Quantum Dot Lasers

The Atomic Force Microscopy (AFM) image of uncapped InP quantum dot grown on AlGaInP at temperature of 690°C is shown in Figure 2.9 [7]. This shows different dot sizes and the difficulty in controlling the growth conditions of the quantum dots will cause a variation in energy levels between the dots due to the quantisation of the energy levels within the individual dots, which is known as inhomogeneous broadening. This broadening cause an energy shift to the spectral peak emitted from each dot and forms from dots with different size as shown in

Figure 2.10 where at any photon energy the emission from these dots will be part of this broadening [8]. The other broadening, called homogeneous broadening, cause an uncertainty in each dot shown as a broadened in the quantum dots individual transitions. This is because the photon energy does not exactly equal the energy difference of the dot state for interaction to accrue. The effect of the two types broadening on the ground state spectral line width is shown clearly in Figure 2.10.

2.6 Recombination in Quantum Dot

This section describes the rate equations from Section 2.3 to produce expressions for the modal absorption and modal gain in quantum dot using the approach of Blood (2009) [9]. The section also presents the spontaneous emission and nonradiative recombination processes which can be taken place within the quantum dot along with the radiative processes.

2.6.1 Modal Absorption

The optical absorption for light incident normal to layer of dots can be represented by the fraction of light absorbed by a number of dots N per unit area as seen in Equation 2.15.

$$\frac{\Delta\Phi(h\upsilon)}{\Phi_0} = N\,[\sigma(E_i, h\upsilon)] = N\,[\sigma_0(E_i)L(E_i, h\upsilon)] \tag{2.15}$$

where $\sigma\,(E_i, h\upsilon)$ is the optical cross section at photon energy $h\upsilon$, $\sigma_0\,(E_i)$ is area under the cross section peak and represents the total absorption strength of a single dot, $L\,(E_i, h\upsilon)$ is the normalised probability of absorption occurring for a photon energy $h\upsilon$ per unit energy interval and E_i is the energy separation of the dot states. The term in the bracket [ ] represents the gain/absorption cross section of a single dot. The area under optical cross section of dot $\sigma_0\,(E_i)$ and the normalised probability of absorption $L\,(E_i, h\upsilon)$ are given by Equations 2.16 and 2.17 respectively.

$$\sigma_0 = \left[\frac{2\times 2h}{cn\varepsilon_0 h\upsilon}\left(\frac{e}{2m_0}\right)^2 M^2 \left\{\int_{dot} F_l(\mathbf{r})F_h(\mathbf{r})d\mathbf{r}\right\}^2\right] \tag{2.16}$$

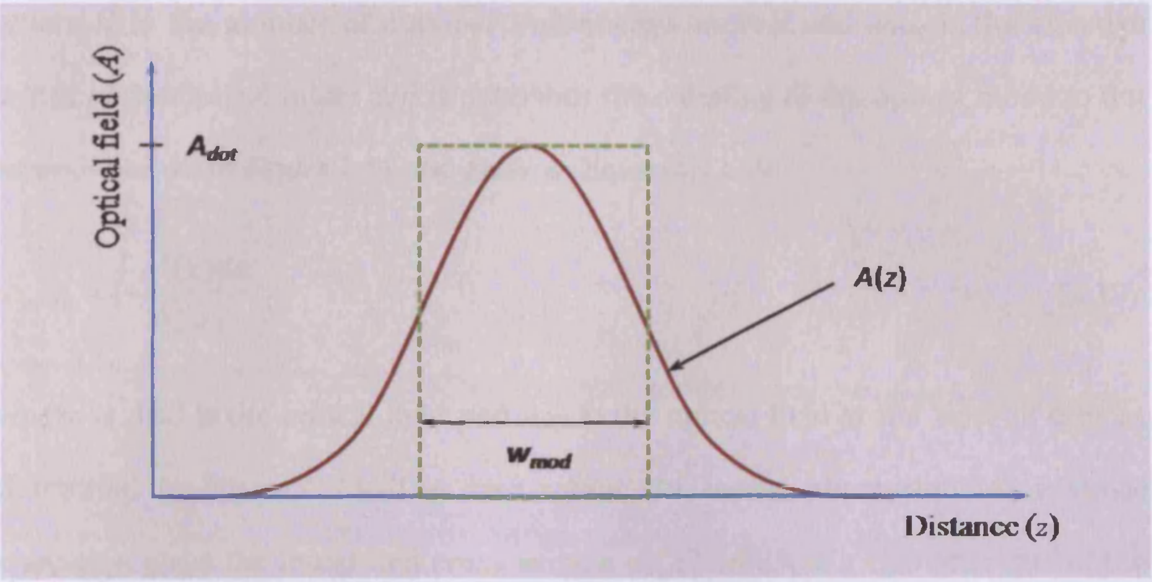

Figure 2.11 *Diagram of the optical field versus distance showing how to obtain the effective mode width.* [9]

$$L(E_i, h\nu) = \left[\frac{1}{\pi} \frac{\Delta E_{hom}}{(h\nu - E_i)^2 + (\Delta E_{hom})^2}\right] \tag{2.17}$$

where h is Plank constant, n is the refractive index, c the speed of light, ε_0 is the permittivity of free space, e is the electron charge, m_0 is the electron mass, M is the transition matrix element within a unit cell of the dot material, $F_h(\mathbf{r})$ and $F_l(\mathbf{r})$ are the envelope functions of the higher and lower confined states respectively and ΔE_{hom} is the homogeneous Lorentzian linewidth.

The modal absorption A_m cross section at any photon energy of an optical mode propagating along the waveguide if the homogeneous linewidth is smaller than the inhomogeneous linewidth is given in Equation 2.18.

$$A_m(h\nu) = \frac{N_i}{w_{mod}} \sigma(E_i, h\nu) \tag{2.18}$$

where N_i is the number of dots per unit energy interval and w_{mod} is the effective width of the optical mode and it describes the coupling of the optical mode to dot layer as shown in Figure 2.11 and given in Equation 2.19.

$$w_{mod} = \frac{\int A^2(z)dz}{A_{dot}^2} \tag{2.19}$$

where is $A(z)$ is the optical field and A_{dot} is the optical field at the layer of dots as illustrated in Figure 2.11. The area under the modal absorption for a single transition gives the integrated cross section $\sigma_0(E_i)$ which is a characteristic of the dot and does not depend on the homogeneous broadening.

$$\int A_m(h\nu)\, d(h\nu) = \frac{N}{w_{mod}} \sigma_0(E_i) \tag{2.20}$$

2.6.2 Modal Gain

The modal gain for propagation along a layer of N number of dots per unit area is given in Equation 2.21.

$$\mathrm{G}(h\nu) = N\, \sigma(E_i, h\nu) \frac{1}{w_{mod}} (f_h - f_l) \tag{2.21}$$

where f_h and f_l are the probabilities that the upper and lower states are occupied with electrons.

2.6.3 Spontaneous Emission

The spontaneous emission rate $R_{spon}(h\nu)$ is proportional to the Einstein coefficient A and the population of the states f_l, f_h as seen in Equation 2.5. The spontaneous emission occurs in all directions and in quantum dot structures, when the spontaneous emission is propagating normal to the layer of dots and not amplified, it can be used to characterise the spontaneous emission spectra. However, the propagation along the dots layer will cause an amplified spontaneous emission. Both the spontaneous and amplified spontaneous emissions are measured in this thesis where the amplified spontaneous emission will be used to find the optical gain and absorption practically as discussed in the next chapter. This will be accompanied with the equations for optical absorption and gain discussed previously in this section. However the unamplified spontaneous emission is measured directly and that should also be accompanied by the equation for spontaneous emission rate discussed previously in section 2.3.

2.6.4 Nonradiative Recombination

Nonradiative recombination takes place in quantum dot when the carriers in the conduction and valence bands recombine nonradiatively which mean no light will be emitted from this process. This will increase the required current needed to achieve lasing which makes it not acceptable and needs to be minimised. The measurements of the nonradiative recombination cannot be done with a direct method because photons are not emitted. They can be measured indirectly by different methods such as measuring the spontaneous emission spectra at different temperatures.

There are two types of nonradiative recombination, Auger recombination and recombination at defects. In Auger recombination processes, the energy which is released from the electron-hole recombination is absorbed by another electron and this electron is excited to a higher energy state then when it start to lose it energy in order to reach thermal equilibrium. The lost energy will be transferred in to phonon or lattice vibration. However, recombination at a defect is described as a number of states, created by the defects in the localized region, at which the carriers recombine nonradiatively through these states.

2.7 Quantum Dot Properties

This section describes some properties of quantum dots showing how the carriers are distributed within quantum dot systems and describing the physics behind that. The section also describes the theory which is used to fit the gain–current relation of a quantum dot system.

2.7.1 Carrier Distributions

The self-assembled quantum dots are separated from each other, therefore the carriers occupying an energy state in one dot cannot occupy an energy state in another dot. The dots in reality form with a distribution of sizes and compositions, therefore their energy levels and conduction band offsets differ. This will cause an inhomogeneous broadening of the spectral emission.

Grundmann et al (1997) [10] describes how the broadening of the spectrum can be a result of random capture of carriers. The thermal distribution, which is defined as the distribution of carriers according to Fermi-Dirac statistics, means that the electrons can be excited thermally out of each dot into the wetting layer. The switch between thermal and non-thermal distributions can be observed in some quantum dot laser structures by studying their lasing threshold at different temperatures. The time for the redistribution process in the quantum dot system must be quicker than the recombination rate in order to satisfy the condition for a thermal distribution. The carriers can recombine radiatively from one dot and the photon emitted could be reabsorbed elsewhere by another dot.

2.7.2 Gain-Current Relation

In order to consider the gain-current characteristic for quantum dot lasers we must include some factors representing the existence of higher energy states and inhomogeneous broadening [11]. The relation for the modal gain-current characteristic including these factors was approximated [12] in Equation 2.22.

$$G_{modal} = G_{sat}\left(1 - e^{-\gamma \frac{J-J_t}{J_t}}\right) \tag{2.22}$$

where G_{sat} represents the saturated modal gain for the dot spectrum, J_t stands for the transparency current density and γ is a dimensionless fitting parameter which accounts for the interaction between the quantum dot states and the inhomogeneous broadening. Equation 2.22 will be used for fitting the gain-current curves in Chapters 4 and 6 to help in their comparison.

2.8 Summary

The general overview of the physical principles of semiconductor quantum dot lasers was given in this chapter. The chapter started by introducing some concepts of semiconductors including bandstructure, the Fermi-Dirac distribution and the density of states. The chapter described the fundamentals of lasers such as emission, absorption, population inversion, feedback processes and the threshold condition. The chapter outlined some physical properties of semiconductor lasers such as optical gain, gain-current relations and separate confinement heterostructures. The chapter described the quantum dot system, describing its nature, self-assembled formation and spectral broadening. The chapter described the recombination in quantum dots including modal gain, absorption, spontaneous emission and nonradiative recombination. The chapter finished with the quantum dot properties including carrier distribution and gain-current relation.

References

[1] L. A. Coldren and S. W. Corzine, "*Diode laser and photonic Integrated circuits*", *Wiley and Sons*, New York, (1995).

[2] H. C. Casey and M. B. Panish, "*Heterostructure Lasers, Part A*", Academic Press, pp. 115-116, (1978).

[3] P. Blood, "*Physics and technology of heterojunction devices, Chapter 7*", edited by D. Vernon Morgan and Robin H. Williams, Peter Perigrinus Ltd., London, UK, (1991).

[4] D. Bimberg, M. Grundmann, N. N. Ledentsov, "*Quantum dot heterostructures*", Wiley Publications, ISBN: 0471973882 (1999).

[5] M. Sugawara, "*Self-Assembled InGaAs/GaAs Quantum Dots*", Volume 60 of Semiconductor and Semimetals, Academic Press, San Diego (1999).

[6] Mowbray D J, Skolnick M S, "*New physics and devices based on self-ssembled emiconductor quantum dots*", Journal of Physics D: Applied Physics, 38, pp. 2059-2076 (2005).

[7] P. M. Smowton, J. Lutti, G. M. Lewis, A. B. Krysa, J. S. Roberts, P. A. Houston, "*InP-GaInP quantum-dot lasers emitting between 690-750nm*", IEEE Journal of Selected Topics in Quantum Electronics, 11, 3 pp. 808- 818 (2009).

[8] P. Borri, W. Langbein, S. Schneider, U. Woggon, R. L. Sellin, D. Ouyang, and D. Bimberg, "*Ultralong Dephasing Time in InGaAs Quantum Dots*", Physical Review Letters, 87, 15,157401 (2001).

[9] P. Blood, "*Gain and recombination in quantum dot lasers*", IEEE Journal of Selected Topics in Quantum Electronics, 15, 5 pp.1035- 1040 (2005).

[10] M. Grundmann and D. Bimberg, "*Theory of random population for quantum dots*", Physical Review B, 55, P9740-9745 (1997).

[11] V. M. Ustinov, A. E. Zhukov, A. Y. Egorov and N. A. Maleev, "*Quantum dot lasers*", Oxford University Press, ISBN: 0198526792 (2003).

[12] A. E. Zhukov, A. R. Kovsh, A. Yu. Egorov, N. A. Maleev, V. M. Ustinov, B. V. Volovik, M. V. Maksimov, A. F. Tsatsul.nikov, N. N. Ledentsov, Yu. M. Shernyakov, A. V. Lunev, Yu. G. Musikhin, N. A. Bert, P. S. Kop.ev and Zh. I. Alferov, "*Photo-and electroluminescence in the 1.3-μm wavelength range from quantum-dot structures grown on GaAs substrates*", Semiconductors, 33, 2, P153-156 (1999).

CHAPTER 3

Structures and Experimental Procedures

3.1 Introduction

This chapter presents the device structures which were used for measurements in this thesis. The chapter begins by introducing the materials used to construct these structures. The chapter describes the device preparation to transform these structures into working laser or multisection devices. The chapter illustrates how these devices can be mounted in order to make them suitable for testing which is the last step required for checking how good these devices are.

The chapter also presents the experimental procedures and equipment used in this thesis to obtain the data presented in the following chapters. These include experiments for measuring the threshold current and spontaneous emission spectra by using the laser device, the optical gain and absorption by using the multisection device. In fact, all the experiments are done in pulsed mode in order to avoid heating effects during measurements.

3.2 Device Materials

The semiconductor materials required to construct the device structures used in this thesis contain two binary compounds, which are GaAs and InP, two ternary alloys, which are $Al_{0.51}In_{0.49}P$ and $Ga_{0.51}In_{0.49}P$, and one quaternary alloy, which is $(Al_{0.3}Ga_{0.7})_{0.51}In_{0.49}P$. The significant advantage in using these materials is they emit light in the wavelength range around 730*nm* required for the various applications mentioned in the motivation in Chapter 1. Another advantage, excluding $Al_{0.51}In_{0.49}P$, is that they have a direct bandgap energy, which means they can be used to emit light efficiently, and this will make them useful for optoelectronic devices such as laser diodes, whereas $Al_{0.51}In_{0.49}P$ has an indirect bandgap energy. Figure 3.1 shows a laser structure with InP as the quantum dot material, $Ga_{0.51}In_{0.49}P$ as the quantum

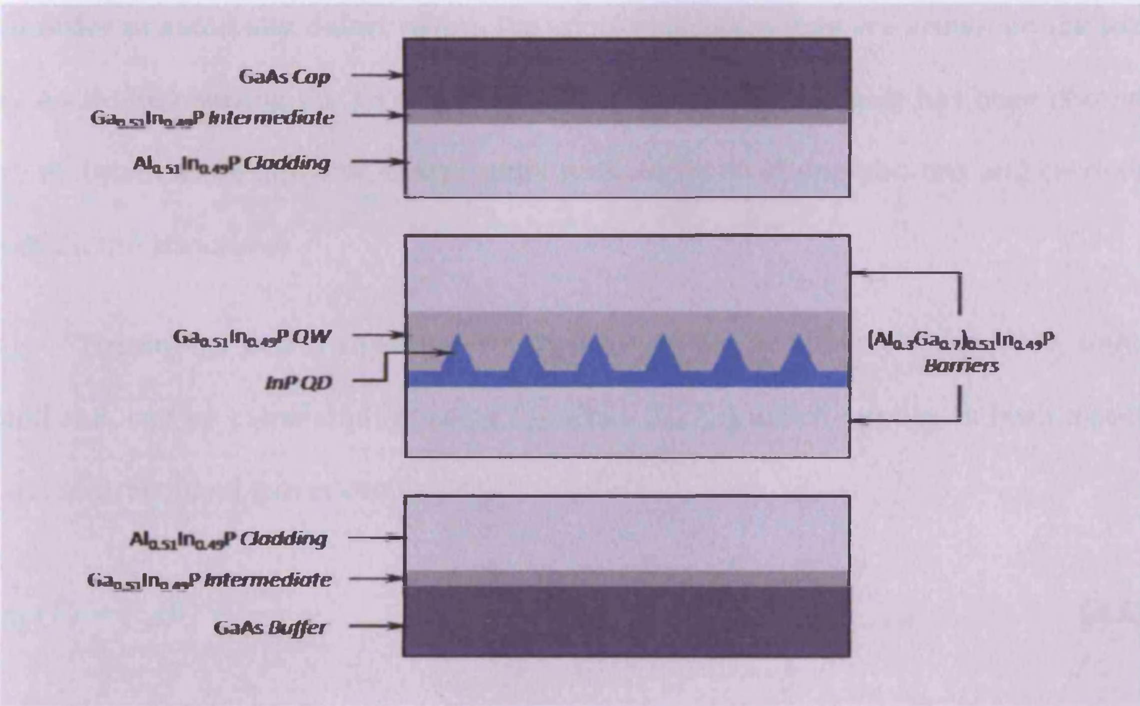

Figure 3.1 *Structure diagram built by using certain semiconductor materials.*

Semiconductor material	$E_g(0)$ (eV)	α ($meV.K^{-1}$)	β (K)
GaAs *direct*	1.519	0.5405	204
GaAs *indirect*	1.981	0.460	204
InP *direct*	1.4236	0.363	162
InP *indirect*	2.384	0.363	≈ 0
AlP *direct*	3.63	0.5771	372
AlP *indirect*	2.52	0.318	588
GaP *direct*	2.886	0.5771	164
GaP *indirect*	2.35	0.5771	372

Table 3.1 *Summary of some binary semiconductor materials and its associated values which used to calculate the energy bandgap at any temperature.*

well material, $(Al_{0.3}Ga_{0.7})_{0.51}In_{0.49}P$ as the barrier material and $Al_{0.51}In_{0.49}P$ as the cladding layers. The composition x in the ternary alloys $Al_{0.51}In_{0.49}P$ and $Ga_{0.51}In_{0.49}P$ are chosen to be equal to 0.51 as this will make these alloys lattice-matched to GaAs in order to avoid any defect within the structures when they are grown on the top of each other during the growth operation. The composition also has been chosen to maintain these alloys at energy gaps suitable for confining photons and carriers within the structures.

The energy gap at any temperature T for the studied binary compounds, GaAs and InP, can be calculated by using Equation 3.1 [1] which applies to both direct and indirect band gap energies

$$E_g(T) = E_g(0) - \frac{\alpha T^2}{T + \beta} \tag{3.1}$$

where $E_g(0)$ is the energy gap at $T = 0K$, α and β are adjustable parameters. These

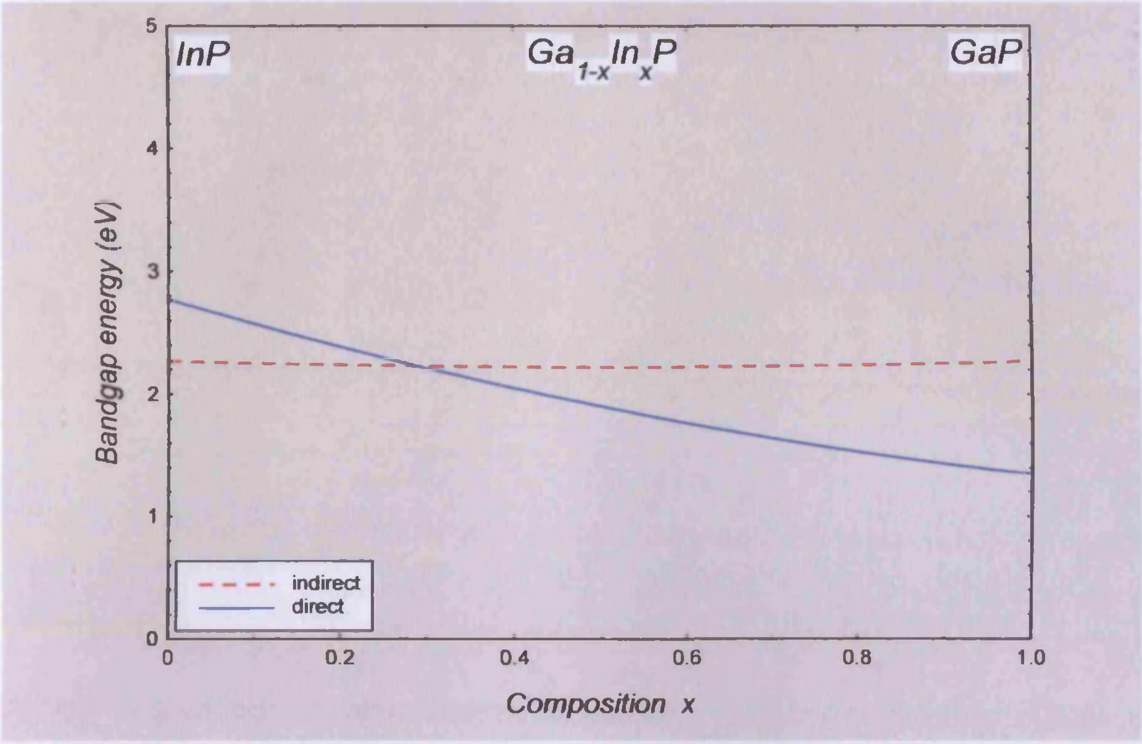

Figure 3.2 *Direct and indirect energy gap for $Ga_{1-x}In_xP$ alloy at temperature of 300K.*

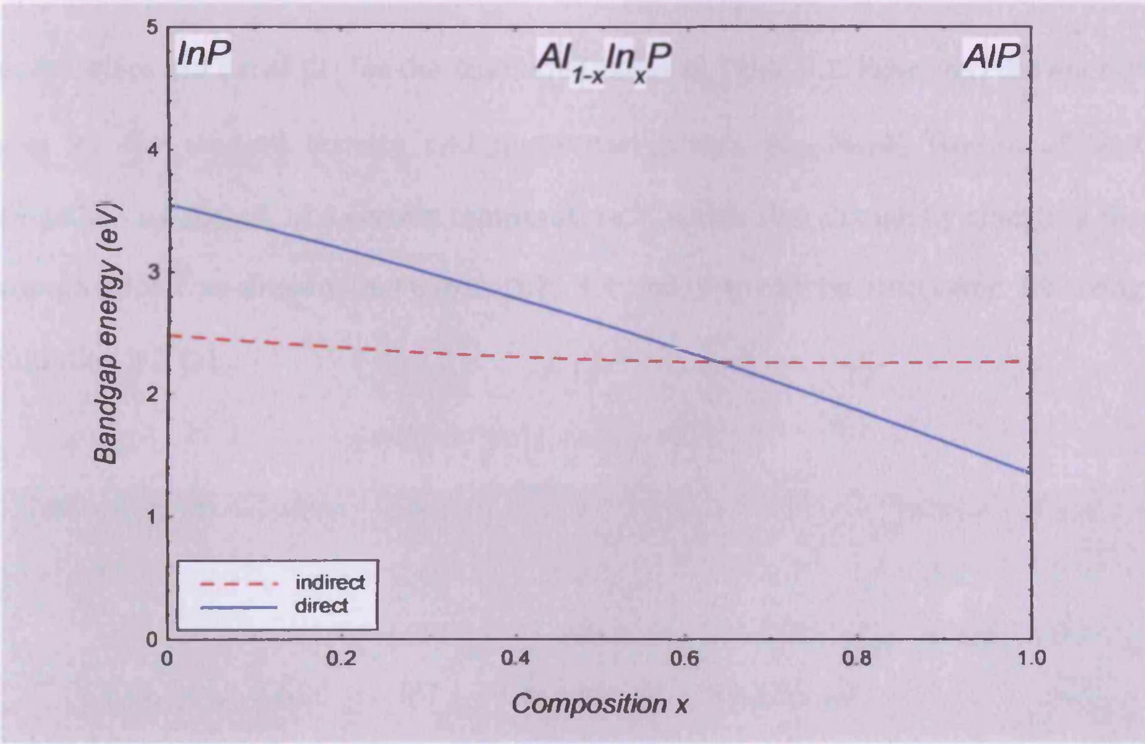

Figure 3.3 *Direct and indirect energy gap for $Al_{1-x}In_xP$ alloy at temperature of 300K.*

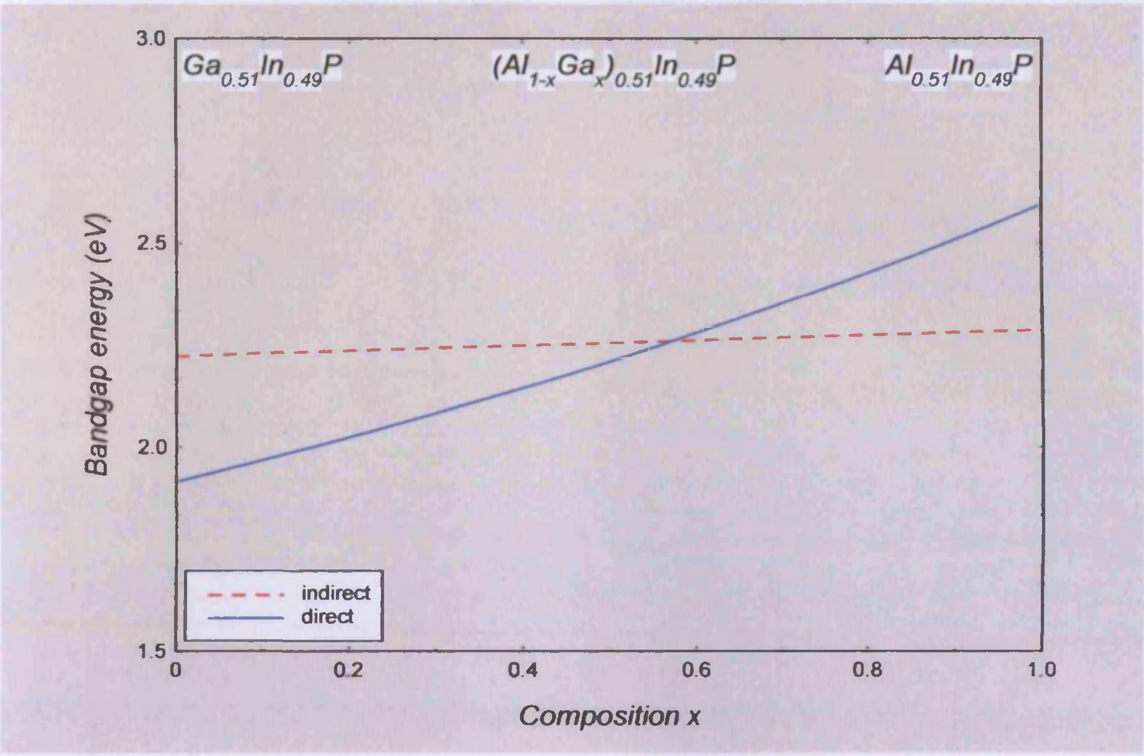

Figure 3.4 *Direct and indirect energy gap for $(Al_{1-x}Ga_x)_{0.51}In_{0.49}P$ alloy at temperature of 300K.*

parameters are listed [2] for the studied binaries in Table 3.1. However, the energy gap for the studied ternary and quaternary alloys, $Al_{0.51}In_{0.49}P$, $Ga_{0.51}In_{0.49}P$ and $(Al_{0.3}Ga_{0.7})_{0.51}In_{0.49}P$, at a certain temperature *T*, which also change by changing the compositions as shown in Figures 3.2, 3.3 and 3.4, can be calculated by using Equation 3.2 [2].

Semiconductor material	*x*	*A*	*B*	*C* direct	*C* indirect
$Ga_{0.51}In_{0.49}P$	0.49	GaP	InP	0.65	0.20
$Al_{0.51}In_{0.49}P$	0.49	AlP	InP	-0.48	0.38
$(Al_{0.3}Ga_{0.7})_{0.51}In_{0.49}P$	0.7	$Ga_{0.51}In_{0.49}P$	$Al_{0.51}In_{0.49}P$	0.18	≈ 0

Table 3.2 *Summary of some ternary and quaternary semiconductor materials and their associated values which were used to calculate the energy bandgap at a certain temperature.*

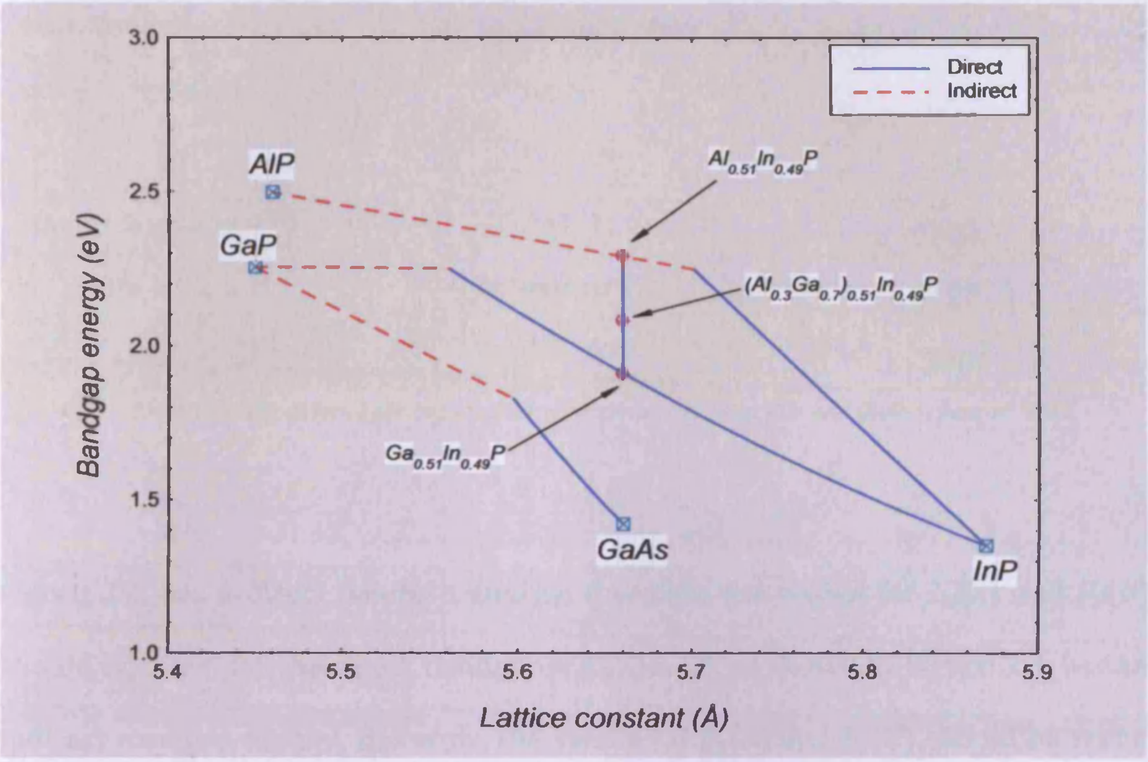

Figure 3.5 *Relationship between the lattice constant and bandgap energy for some semiconductor materials at a temperature of 300K.* [3]

$$E_g(A_{1-x}B_x) = (1-x)E_g(A) + xE_g(B) - x(1-x)C \tag{3.2}$$

where A and B represent the binary compounds or the ternary alloys which are the basis for a given ternary or quaternary alloys respectively, x is the composition between the two A and B binaries or ternaries, $E_g(A)$ and $E_g(B)$ representing the energy bandgap for the binary compounds or ternary alloys A and B respectively at certain temperature T and C is the bowing parameter, which is responsible for the curvature of the line between $E_g(A)$ and $E_g(B)$. Most of these parameters are listed [2] for the studied ternary and quaternary alloys in Table 3.2. The unlisted parameters, $E_g(A)$ and $E_g(B)$, can be calculated depending on the ternary or quaternary alloys bandgap energy type. For example, $Ga_{0.51}In_{0.49}P$, as shown in

Semiconductor material	***Energy bandgap type***	E_g **(300*K*) (*eV*)**
$GaAs$	*Direct*	1.42
InP	*Direct*	1.35
$Ga_{0.51}In_{0.49}P$	*Direct*	1.92
$Al_{0.51}In_{0.49}P$	*Indirect*	2.29
$(Al_{0.3}Ga_{0.7})_{0.51}In_{0.49}P$	*Direct*	2.08

Table 3.3 *Energy bandgap types for the studied semiconductor materials and their values at 300K.*

Figure 3.2, has a direct bandgap energy, therefore the values for $E_g(A)$ and $E_g(B)$ should be taken for the direct bandgaps; $Al_{0.51}In_{0.49}P$, as shown in Figure 3.3, has an indirect bandgap energy, therefore the values for $E_g(A)$ and $E_g(B)$ should be taken for the indirect bandgaps and $(Al_{0.3}Ga_{0.7})_{0.51}In_{0.49}P$, as shown in Figure 3.4, has a direct bandgap energy, so the values for $E_g(A)$ and $E_g(B)$ should be taken for the direct bandgaps. As a result of all this, the energy bandgap for the studied semiconductor materials at temperature of 300K are listed in Table 3.3 and illustrated in Figure 3.5 [3] which shows the relationship between the lattice constant and bandgap energy for the studied semiconductor materials.

3.3 Device Preparation

The semiconductor materials described in the previous section were used to form device structures using the growth methods and fabrication processes described in this section.

3.3.1 Growth Mechanism

The device structures used in this thesis were designed by Peter M. Smowton in the School of Physics and Astronomy, Cardiff University and grown by Andrey B. Krysa in the EPSRC National Centre for III-V Technologies, University of Sheffield. The growth method used to grow the structures was Metal Organic Vapour Phase Epitaxy (MOVPE) which has become the dominant process for the manufacture of

Structure Name	W_b (nm)	T_g (°C)	M_d (ML)
MR2315	8	690	2.0
MR2316	8	690	2.5
MR2317	8	690	3.0
MR2318	8	710	2.0
MR2320	8	730	2.0
MR2321	8	750	2.0
MR2523	16	710	2.5
MR2524	16	730	2.5
MR2528	16	730	2.0
MR2530	16	730	3.0
MR2525	16	750	2.5

Table 3.4 *Summary of structures used and associated growth conditions, giving the barrier width, growth temperature and quantity of deposited quantum dot material.*

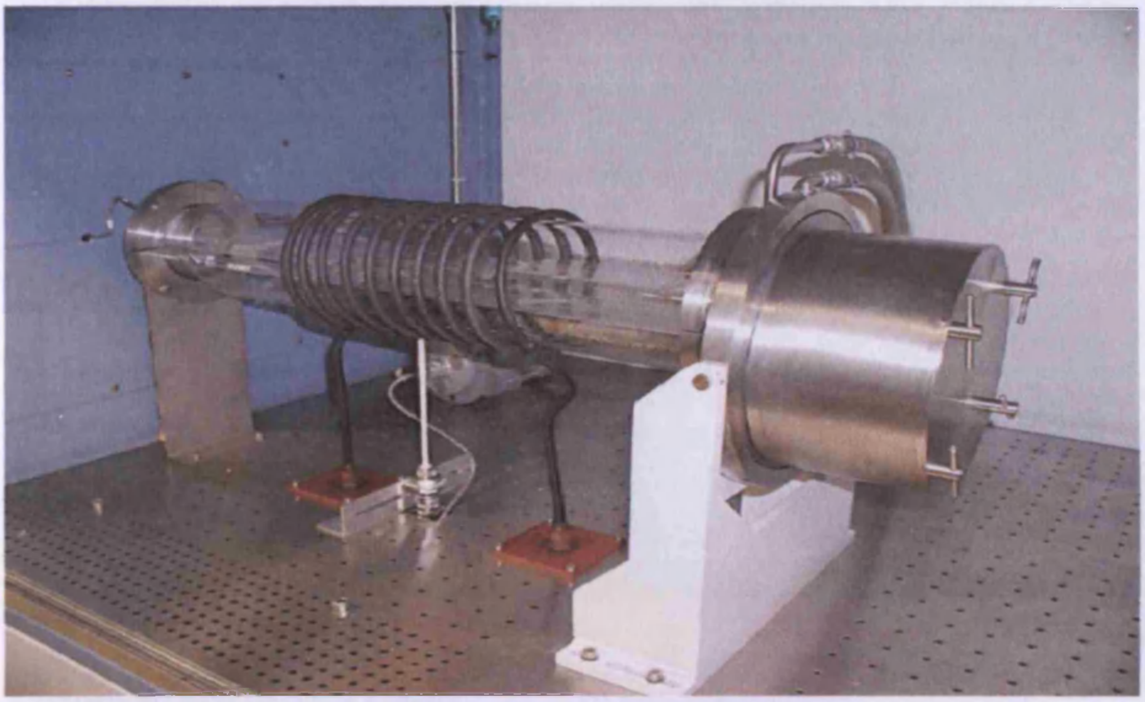

Figure 3.6 *MOVPE growth reactor (MR350).* [4]

laser diodes, solar cells, and LEDs. In this method, the growth of crystals is by chemical reaction not by physical deposition as in Molecular Beam Epitaxy (MBE). The MOVPE reactor shown in Figure 3.6 [4] uses a low pressure 150*Torr* horizontal flow which is necessary to create controllable epitaxial layered structures by chemical reaction over a substrate material placed on a graphite susceptor and heated in a reaction vessel. The semiconductor materials are grown in a hydrogen atmosphere and then form epitaxial layers on the substrate as they decompose.

There are many structures used in this thesis and these are similar but with differences in the growth conditions such as growth temperature T_g, barrier width W_b and quantity of deposited quantum dot material M_d. These growth conditions are given in detail in Table 3.4. In the studied structures, the substrates are made of

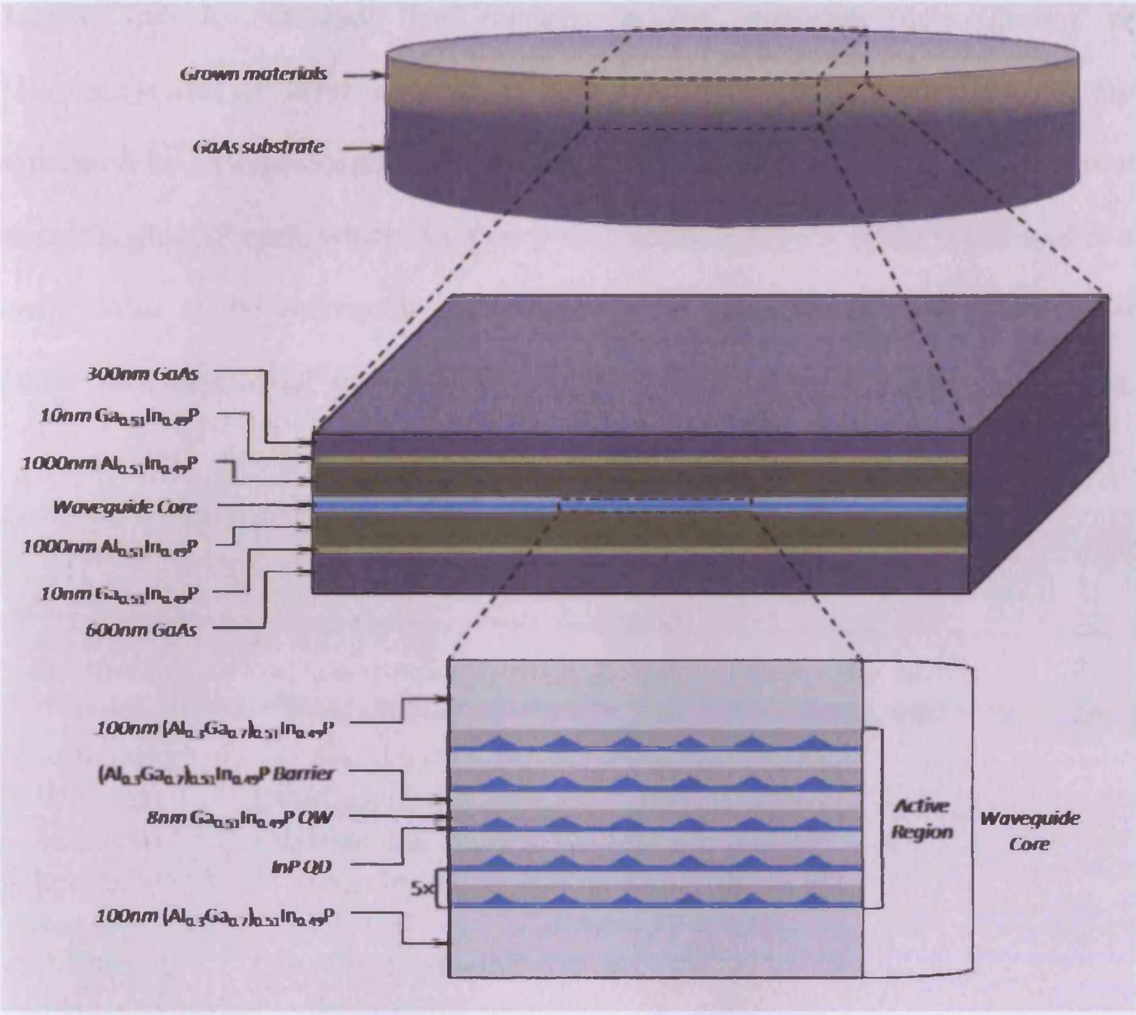

Figure 3.7 *Device Structure diagram grown by MOVPE.*

n-doped GaAs with the growth plane of (100) oriented by 10° off towards (111). The MOVPE reactor grows the semiconductor materials on the substrate by using trimethyl precursors for the group III elements and arsine AsH_3 and phosphine PH_3 as precursors of the group V elements. The device structure was grown at temperature of $690°C$ with a waveguide core grown at one of the given growth temperatures listed in Table 3.4. The waveguide core, as illustrated in Figure 3.7, consists of an active region placed in between $100nm$ thick $(Al_{0.3}Ga_{0.7})_{0.51}In_{0.49}P$

layers and it contains five repeats of InP quantum dots grown on $(Al_{0.3}Ga_{0.7})_{0.51}In_{0.49}P$ layer, covered by 8*nm* thick $Ga_{0.51}In_{0.49}P$ quantum wells and separated by $(Al_{0.3}Ga_{0.7})_{0.51}In_{0.49}P$ barriers. The cladding layers consist of 1000*nm* thick $Al_{0.51}In_{0.49}P$ each, which is either *p* or *n* doped using Zn at the upper and Si at lower sides of the waveguide core respectively. The intermediate layers are of 10*nm* thick $Ga_{0.51}In_{0.49}P$ each, which are *p* and *n* doped at the upper and lower sides

Layer	Material Type	Thickness (*nm*)	Carrier density (*cm*$^{-3}$)	Dopant
Cap	GaAs	300	1×10^{18}	Zn
Intermediate	$Ga_{0.51}In_{0.49}P$	10	1×10^{18}	Zn
Cladding	$Al_{0.51}In_{0.49}P$	950	5×10^{17}	Zn
Cladding	$Al_{0.51}In_{0.49}P$	50		
Barrier	$(Al_{0.3}Ga_{0.7})_{0.51}In_{0.49}P$	86		
Barrier	$(Al_{0.3}Ga_{0.7})_{0.51}In_{0.49}P$	8 or 16		
Quantum well	$Ga_{0.51}In_{0.49}P$	8		
Quantum dots	InP	0.6 or 0.75 or 0.9		
Barrier	$(Al_{0.3}Ga_{0.7})_{0.51}In_{0.49}P$	8 or 16		
Quantum well	$Ga_{0.51}In_{0.49}P$	8		
Quantum dots	InP	0.6 or 0.75 or 0.9		
Barrier	$(Al_{0.3}Ga_{0.7})_{0.51}In_{0.49}P$	8 or 16		
Quantum well	$Ga_{0.51}In_{0.49}P$	8		
Quantum dots	InP	0.6 or 0.75 or 0.9		
Barrier	$(Al_{0.3}Ga_{0.7})_{0.51}In_{0.49}P$	8 or 16		
Quantum well	$Ga_{0.51}In_{0.49}P$	8		
Quantum dots	InP	0.6 or 0.75 or 0.9		
Barrier	$(Al_{0.3}Ga_{0.7})_{0.51}In_{0.49}P$	8 or 16		
Quantum well	$Ga_{0.51}In_{0.49}P$	8		
Quantum dots	InP	0.6 or 0.75 or 0.9		
Barrier	$(Al_{0.3}Ga_{0.7})_{0.51}In_{0.49}P$	100		
Cladding	$Al_{0.51}In_{0.49}P$	1000	5×10^{17}	Si
Intermediate	$Ga_{0.51}In_{0.49}P$	10	1×10^{18}	Si
Buffer	GaAs	600	2×10^{18}	Si

Table 3.5 *Device structure details.*

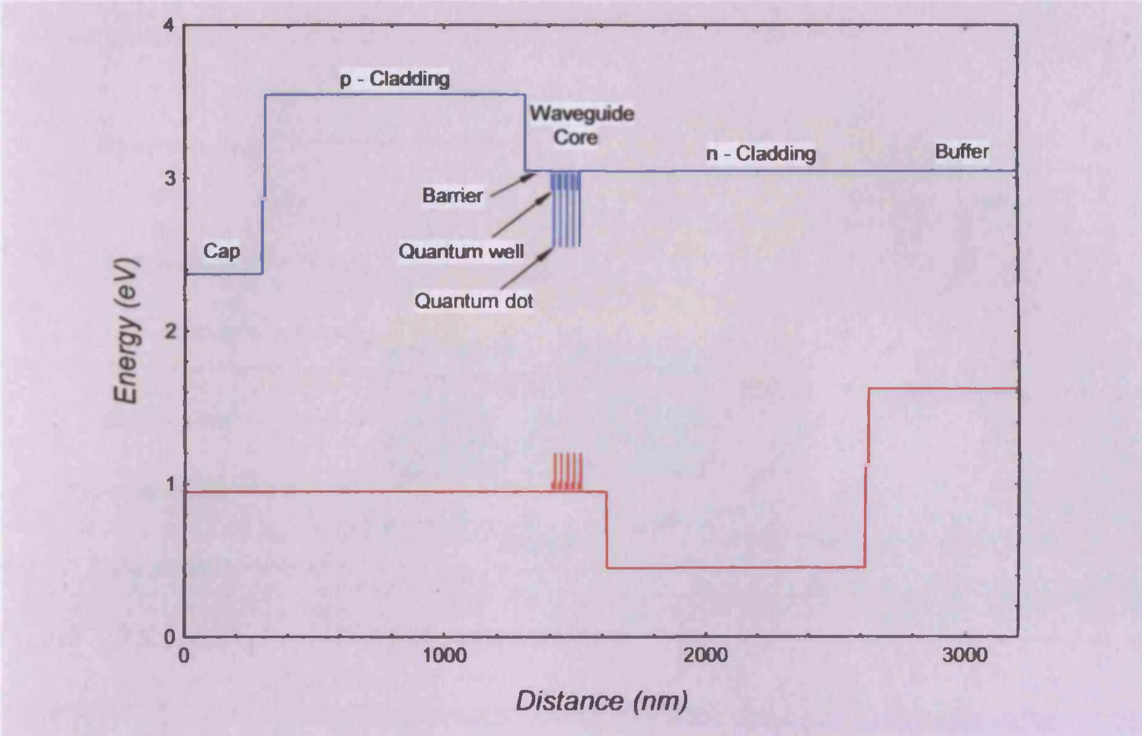

Figure 3.8 *Energy bandgap diagram for a typical structure under forward bias.*

of the cladding layers respectively. It is formed to reduce the high difference in energy gaps between the cladding layers and the cap or buffer layers. The cap and buffer layers are formed to decrease the contact resistance. They consist of 300*nm* thick *p* doped GaAs for the cap layer and 600*nm* thick *n* doped GaAs for the buffer layer. The device structure details are listed in Table 3.5 and a structure diagram is shown in Figure 3.7. The bandgap energy versus growth thickness is shown in Figure 3.8 and this related to a typical structure.

3.3.2 Device Fabrication

All studied structures are fabricated and processed into laser and multisection devices in the cleanroom facilities of the School of Physics and Astronomy, Cardiff

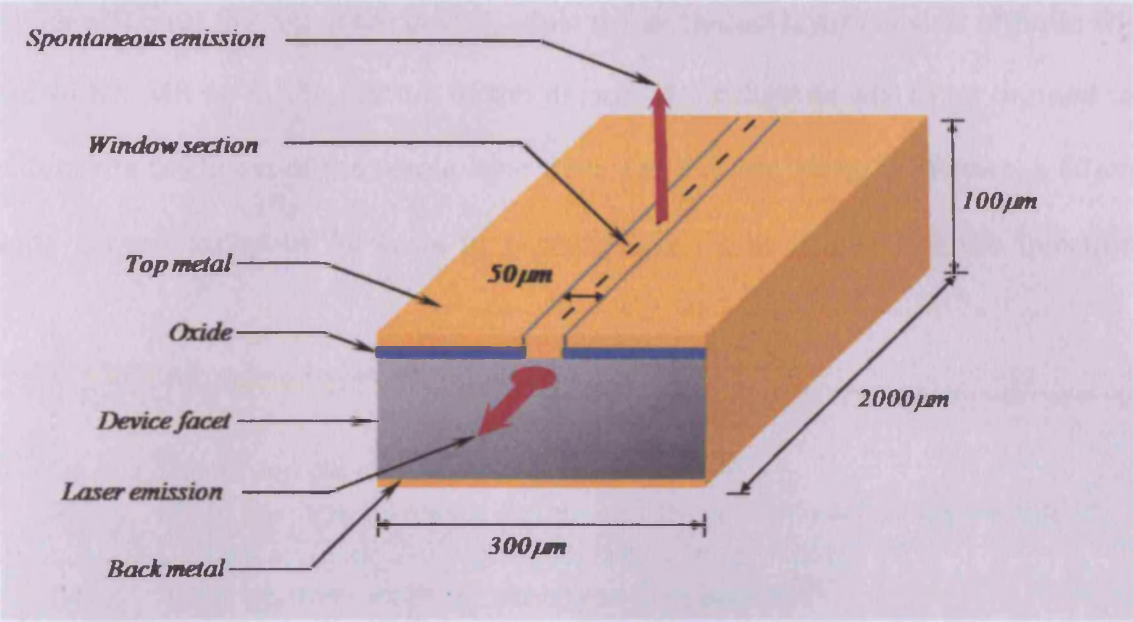

Figure 3.9 *Schematic diagram of oxide stripe laser device.*

University by the cleanroom staff. The processing of the structures is *n* side down the semiconductor materials were grown on *n* type substrate. The processing methods into laser and multisection devices are known as oxide stripe laser and multisection device respectively. These two processing methods will be described in detail in the following.

Oxide stripe laser

The oxide stripe laser processing method with top widows is used to fabricate laser devices for experimental measurements such as threshold current and spontaneous emission to characterise these structures. In Figure 3.9 a typical oxide stripe laser is shown, the processing procedures are listed with details in Table 3.6 starting from scribing a small piece from the structure and ending with cleaning the laser devices after demounting them. The *p*-metalisation layer consists of Au-Zn, which will be at the top of the device, while the *n*- contact layer consists of AuGe-Ni-Au, which will be at the bottom of the device. The substrate has to be thinned to reduce the thickness of the whole laser device to 100μm. Along the device, a 50μm wide contact stripe of Au-Zn is in between the oxide stripes and the injection

Step No.	Step Description
01	Scribe and cleave the structure.
02	Clean the structure with chemicals using cotton bud then De-oxide it.
03	Deposit an oxide SiO_2 on the structure then bake it.
04	Apply photoresist to the structure then bake it.
05	Expose the photoresist using 50μm stripe mask.
06	Develop the photoresist then bake it.
07	Etch the oxide SiO_2 using wet etching.
08	Remove the photoresist then clean it with chemicals.
09	Evaporate the metals Au:Zn.
10	Apply photoresist then bake it.
11	Expose the photoresist using 50μm stripes mask (between the stripes).
12	Develop the photoresist then bake it.
13	Etch the Zn:Au in 50μm stripe using wet etching.
14	Etch the oxide SiO_2 using wet etching.
15	Remove the photoresist then clean it with chemicals.
16	Apply photoresist to the structure then bake it.
17	Expose the photoresist using window mask.
18	Develop the photoresist then bake it.
19	Etch the Zn:Au in small whole short etch using wet etching.
20	Remove the photoresist then clean it with chemicals.
21	Anneal Zn:Au then etch GaAs under the windows.
22	Mount the structure for lapping then lapp it to 100μm then polish it.
23	Demount the structure then clean it with chemicals.
24	Evaporate the metals AuGe:Ni:Au then anneal it.
25	Mount the structure on moly foil sheet.
26	Scribe shortly to determine the facets then cleave it.
27	Scribe for 2*mm* long devices and cleave it into laser devices.
28	Demount the laser devices then clean them with chemicals.

Table 3.6 *Oxide stripe laser processing method procedure.*

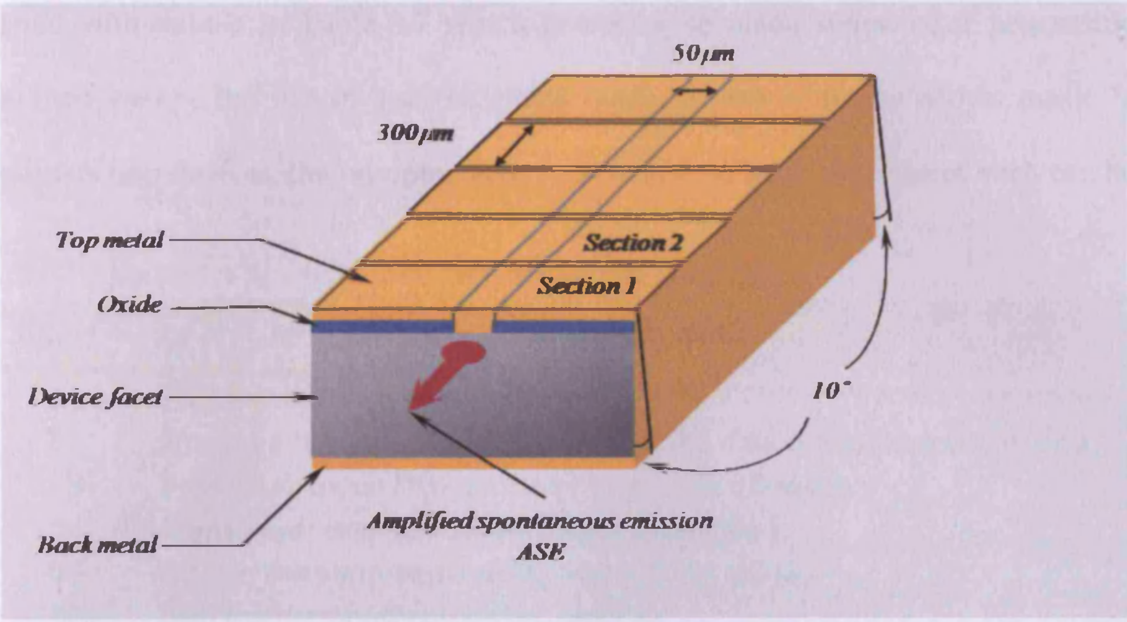

Figure 3.10 *Schematic diagram of multisection device.*

current is confined in this method. The cleaving process is used to determine the length of the laser device, which is fixed to be about $2000\mu m$. The device length is the cavity length and the reflectivity is due to the semiconductor-air interface and electromagnetic modes emit from both facets. The window sections in the top contact enable us to observe pure spontaneous emission and to avoid stimulated emission. The etching process, which forms these windows, is only etched through the top contact layer.

Multisection device

The multisection device processing method is used to fabricate structures into multisection devices required for experimental measurements such as absorption and gain spectra to characterise these structures. In Figure 3.10 a typical multisection device is shown, the processing procedures used to reach that are listed with details in Table 3.7 which is similar to oxide stripe laser processing method except the use of 4μm channels mask instead of the windows mask. In multisection devices, the pumping area is divided into several sections, each can be

Step No.	Step Description
01	Scribe and cleave the structure.
02	Clean the structure with chemicals using cotton bud then De-oxide it.
03	Deposit an oxide SiO_2 on the structure then bake it.
04	Apply photoresist to the structure then bake it.
05	Expose the photoresist using 50μm stripe mask.
06	Develop the photoresist then bake it.
07	Etch the oxide SiO_2 using wet etching.
08	Remove the photoresist then clean it with chemicals.
09	Evaporate the metals Au:Zn.
10	Apply photoresist then bake it.
11	Expose the photoresist using 50μm stripes mask (between the stripes).
12	Develop the photoresist then bake it.
13	Etch the Zn:Au in 50μm stripe using wet etching.
14	Etch the oxide SiO_2 using wet etching.
15	Remove the photoresist then clean it with chemicals.
16	Apply photoresist to the structure then bake it.
17	Expose the photoresist using 4μm channels mask between sections.
18	Develop the photoresist then bake it.
19	Etch the Zn:Au using wet etching.
20	Etch the oxide SiO_2 using wet etching.
21	Remove the photoresist then clean it with chemicals.
22	Anneal Zn:Au then etch GaAs between sections.
23	Mount the structure for lapping then lap it to 100μm then polish it.
24	Demount the structure then clean it with chemicals.
25	Evaporate the metals AuGe:Ni:Au then anneal it.
26	Mount the structure on moly foil sheet.
27	Scribe shortly to form the multisection stripes then cleave it.
28	Scribe edge of strip at 5 section intervals and cleave them.
29	Demount the multisection devices then clean them with chemicals.

Table 3.7 *Multisection device processing method procedure.*

pumped individually. The length of each section is $300\mu m$ and, along the section, a $50\mu m$ wide contact stripe of Au-Zn is in between the oxide stripes.

In order to determine the gain and absorption of the structure, the measurement of the single-pass Amplified Spontaneous Emission (ASE) is required. The ASE is the light which is amplified by a single pass of light through a specific length. Multiple passes are avoided by using 10° angle facets with respect to the normal of the mode propagation to remove the feedback process.

3.4 Device Mounting and Testing

The laser and multisection devices are mounted on a standard TO5 transistor header for handling and usage in the experiments. The laser device is mounted with two different orientations, first with device edge facing the experiment, Figure 3.11(a) and 3.11(b), and second with device top facing the experiment after remounting the copper block on the header, Figure 3.11(c). However, the multisection device is mounted only with device edge facing the experiment. Each header can have two laser devices or one multisection device whereas the positive

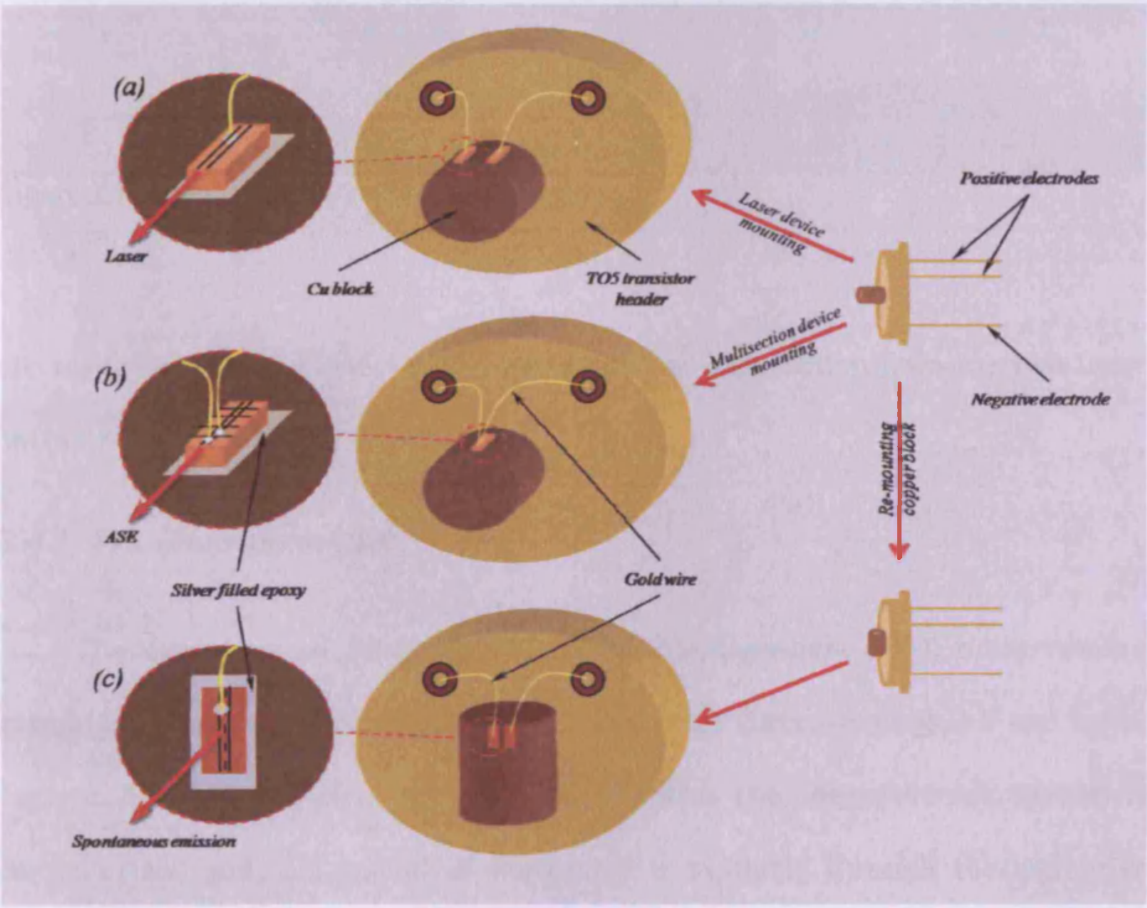

Figure 3.11 *Diagram of a standard TO5 transistor header shows how devices can be mounted as (a) laser edge facing, (b) multisection edge facing and (c) laser top facing.*

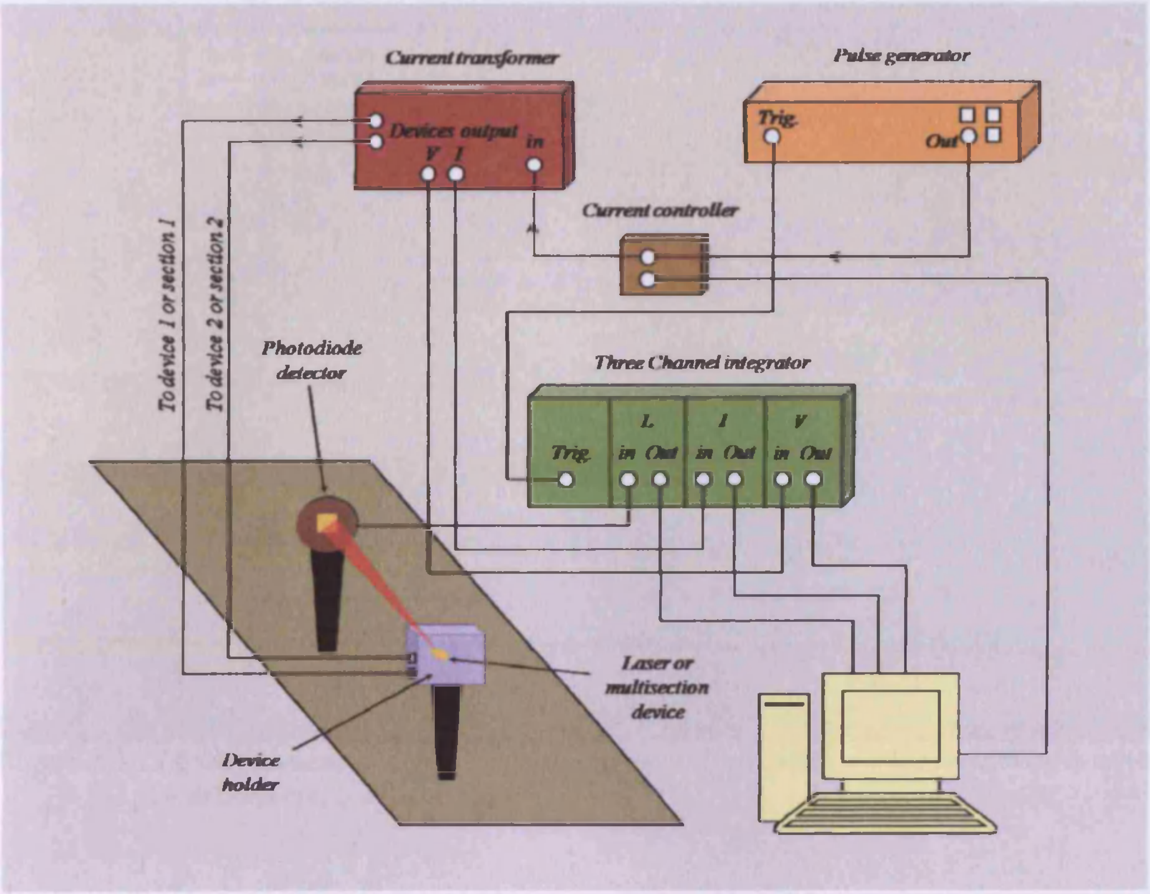

Figure 3.12 *Block diagram of IVL measurement system.*

electrode can either connect each laser device or each section from the two front sections in the multisection device.

3.4.1 IVL Measurements

The experimental setup for the current-voltage-light I-V-L measurement system is shown in Figure 3.12 and used to measure current-voltage I-V and light-current L-I characteristics at room temperature. The measurement system is computerised and the control of the inputs is available through the computer program. The pulse generator is set to $1000ns$ duration and $1KHz$ rate to reduce self

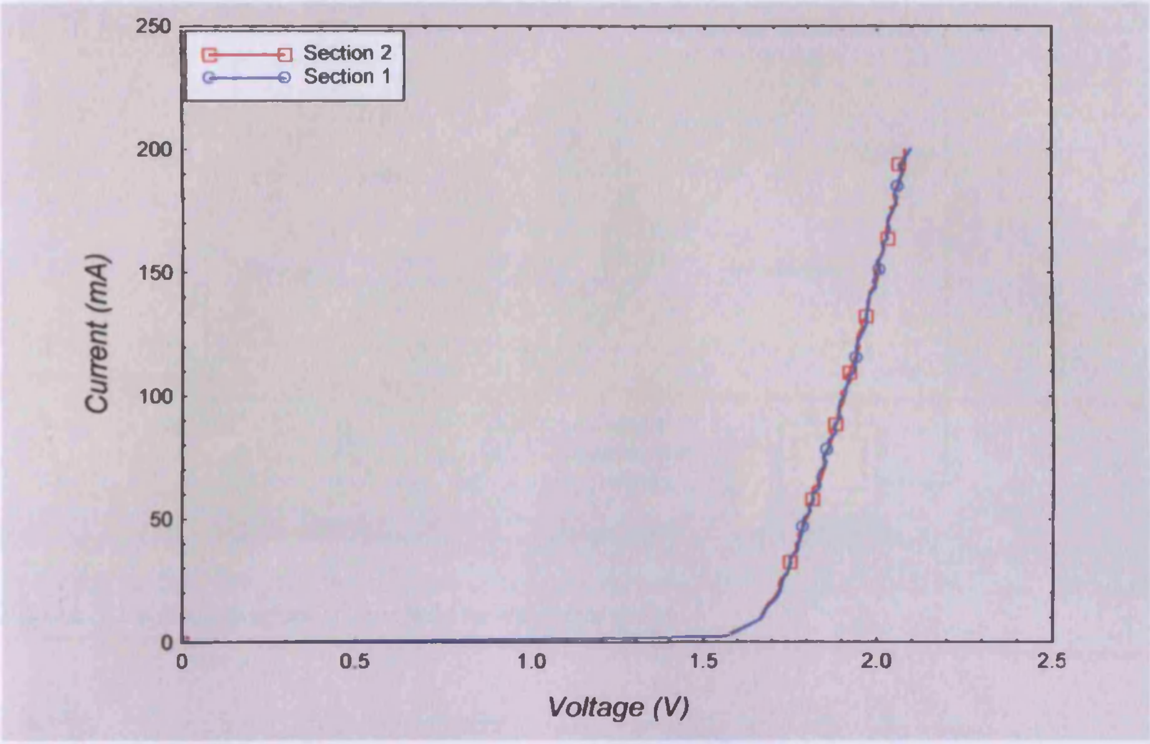

Figure 3.13 *I-V characteristic of a typical multisection device. The symbols marked on each curve are a guide to the eye.*

heating effects. The three channel integrator averages the gate signals of current, voltage and light when they are triggered to the output gates. The gate positions are chosen to be at the stable part on the signals. The sample is held in a device holder and the light is detected by using a photodiode detector.

The I-V and L-I characteristics are important for checking the laser and multisection devices performance. In the laser device, the I-V characteristic checks the device contact, which should start with almost zero current and turn on at about 1.6V as shown in Figure 3.13, while the L-I characteristics shows how good the device is by looking at its threshold. More details about finding the threshold from L-I characteristics are discussed in the next section. In the multisection

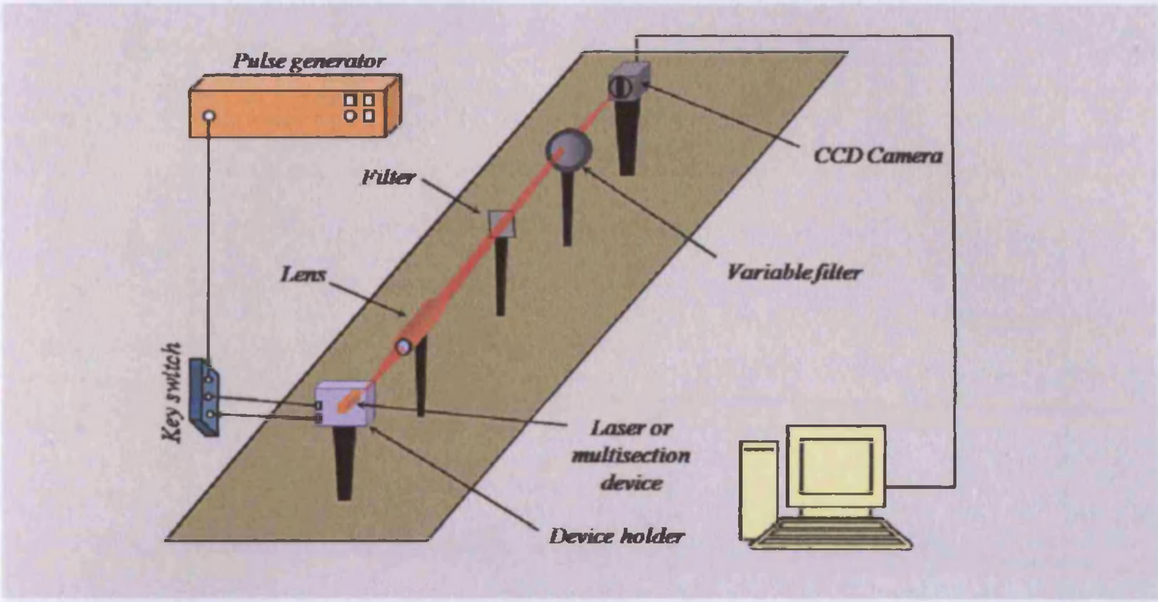

Figure 3.14 *Block diagram of near field measurement system.*

device, the first two sections are used and relations for obtaining the gain and absorption spectra [5] are based on this case. These relations are discussed in detail later in this chapter. The I-V characteristic of section 1 and 2 should be identical in order to satisfy these relations to use for further checking otherwise the multisection device will not considered suitable. Figure 3.13 shows an example of I-V characteristics section 1 and 2 for a typical multisection device suitable for further measurements. This can be made by taking a fixed current and calculating the difference percentage, exceeding no more than 3% will mean that the multisection device is suitable for further measurements.

3.4.2 Near Field Measurements

The near field is defined as the distribution of light intensity at the facet of the laser or multisection devices. The advantages of using the near field measurements

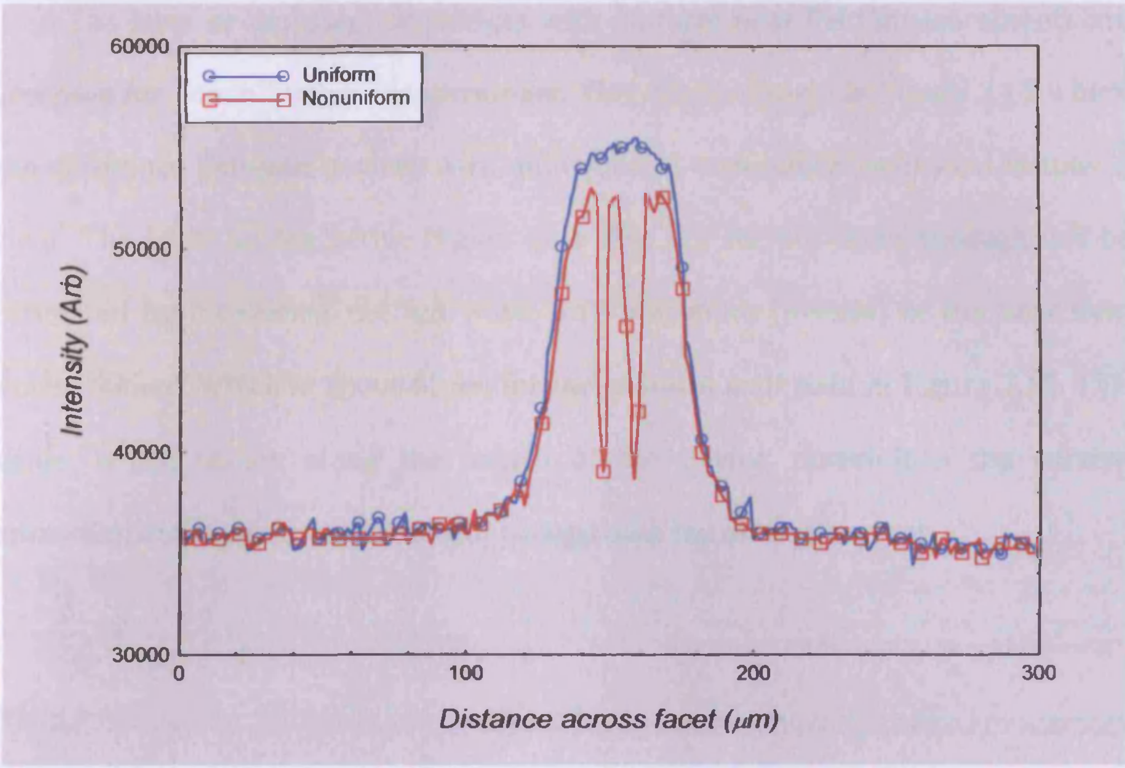

Figure 3.15 *Near field measurements for typical laser devices with uniform (circles) and nonuniform (squares) near field shapes. The symbols marked on each curve are a guide to the eye.*

are to check if there is any damage in the active region across the device facet and to find accurate value for the area that the current flows through. The experimental setup used to measure this active width is shown in Figure 3.14 and it can be measured by holding the device in the device holder and driving it with a pulsed current using pulse generator set at 1000*ns* duration and 1*KHz* rate. The light emitted from the device is coupled in to a CCD camera by using a ×5 magnification lens. A set of filters are used to avoid the saturation limit of the emitting light in the CCD camera. The CCD camera takes a photo for the near field, then the photo is analysed using the profiling properties in Origin program, which plot the intensity of the light density on the digital image against the distance across the device facet.

The laser or multisection devices with uniform near field measurements are accepted for use in further measurement. This can be shown in Figure 3.15 where the difference between devices with uniform and nonuniform near field shapes is clear. The width of the active region area that the current flows through can be estimated by measuring the full width half maximum (FWHM) of the near field measurement, which is about $53\mu m$ for the uniform near field in Figure 3.15. This value, which occurs along the length of the device, determines the current spreading in the device and does not change with the driving current.

3.5 IVL-T Measurements

The current-voltage-light-temperature (IVL-T) measurement includes the measurement of the current-voltage I-V and light-current L-I characteristics at a range of temperatures between $150K - 400K$. Before taking any IVL-T measurement data from the system, temperature and current calibration are required.

3.5.1 Temperature and Current Calibration

The calibration of both current and temperature can be done by comparing their outputs, taken by the system, with their outputs taken by another calibrated equipments. In temperature calibration the comparison is between two diode sensor temperatures, one of them is already installed in the system and the other is placed in the device position. However, current calibration compares two currents; one is given by the system and the other by a calibrated current probe.

Temperature calibration

This calibration requires a diode sensor calibrated by applying constant current and measuring the voltages at different known temperatures. These are Nitrogen boiling point $77K$, Carbon dioxide sublimation point $195K$, water triple and boiling points $273K$ and $373K$ respectively. This is done by a member of the optoelectronic research group. From these four points one can obtain a general relationship between the voltage and temperature of the diode sensor. This diode sensor is driven by a constant current and placed at position where the laser device is sitting to allow taking a range of readings as a function of temperature. The obtained relationship for the diode sensor is then used to derive an equation which describes the relation between the real temperature T_r, as measured by the sensor, and the output from the computer T_c for the diode sensor located in the chamber below the position of the laser device.

Current calibration

The current calibration is comparing two currents, one is taken by the system I_c, which needs to be calibrated, and the other is taken by an oscilloscope I_r using a calibrated current probe. A typical laser device is placed into the system to allow taking a range of readings for both currents in order to derive an equation that describes the relation, which is linear, between the real current I_r and the current read by the computer I_c.

3.5.2 L-I Characteristics

The experimental set up for L-I measurements is shown in Figure 3.12 with the laser device is held in a device holder facing the photo detector. The pulse generator applied a 1000*ns* long pulse with a repetition frequency of 1*kHz* to the laser devices. The 3 channel boxcar integrator measures the current and voltage signals using a pulse transformer for the current and also measure the voltage across the resistor in the photo detector. It is based on a sample-and-hold technique that averages the incoming signal over the gate pulse length, d.c. voltages representing the current, voltage and light signals are fed back to the software. The measured light intensity of the laser device as a function of injection current is

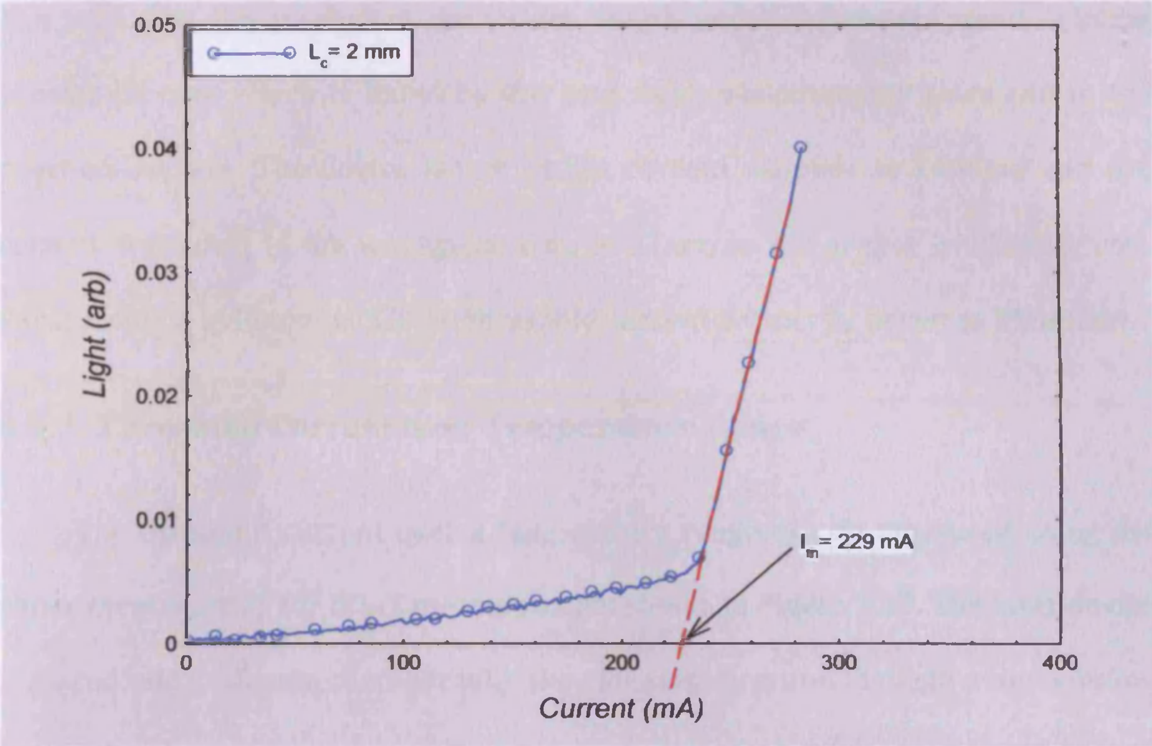

Figure 3.16 *Threshold current of a topical laser device at room temperature.*

shown in Figure 3.16 at room temperature for a typical 2mm long laser device. The small amplitude at low currents is due to spontaneous emission and threshold is reached when the optical gain matches the optical losses. The device starts lasing at this point and the light output increases abruptly as shown in Figure 3.16. By extrapolating the light-current curve at a constant slope backwards the threshold current was then determined where it crosses the current axis. This point refers to the threshold current. In this case the threshold current I_{th} from Figure 3.16 is 229mA. The threshold current density J_{th} is a more representative parameter which defined as the threshold current per unit area and represented by Equation 3.3.

$$J_{th} = \frac{I_{th}}{A} \tag{3.3}$$

The area A is the product of the device length and the current spreading in the waveguide core which is found by the near field measurements discussed in the previous section. The device length in the current example is $2000\mu m$ and the current spreading in the waveguide core is $53\mu m$, so the area A is $10.6\times10^{-4}cm^2$. Substituting A in Equation 3.3 the threshold current density J_{th} becomes $216A/cm^2$.

3.5.3 Threshold Current over Temperature Range

The threshold current over a temperature range can be measured using the experimental set up for IVL-T measurements shown in Figure 3.17. The laser device is placed into a vacuum chamber with the emission direction through a top window in the chamber. A photo detector placed above the window measured the photons out of the emitting laser diode. The temperature is varied in the range from $150K$ – $400K$ by using a copper finger steeped into a small container filled with liquid nitrogen LN_2 and the heater controller connected to the heat sink of the sample. The pulse generator applied a $1000ns$ long pulse with a repetition frequency of $1kHz$ to the laser device. The software installed has the ability to run and control the IVL measurements over a range of temperature. It is necessary to measure the threshold current as a function of temperature in order to obtain information on device parameters and understand physical processes. For this reason, the temperature control equipment is built, which is shown schematically in Figure 3.17. It consists of a sample stage placed in a chamber, which has a window on its top, and a copper finger, which passed through this chamber into a small container fill with liquid nitrogen LN_2. The laser device is set on a copper block hold

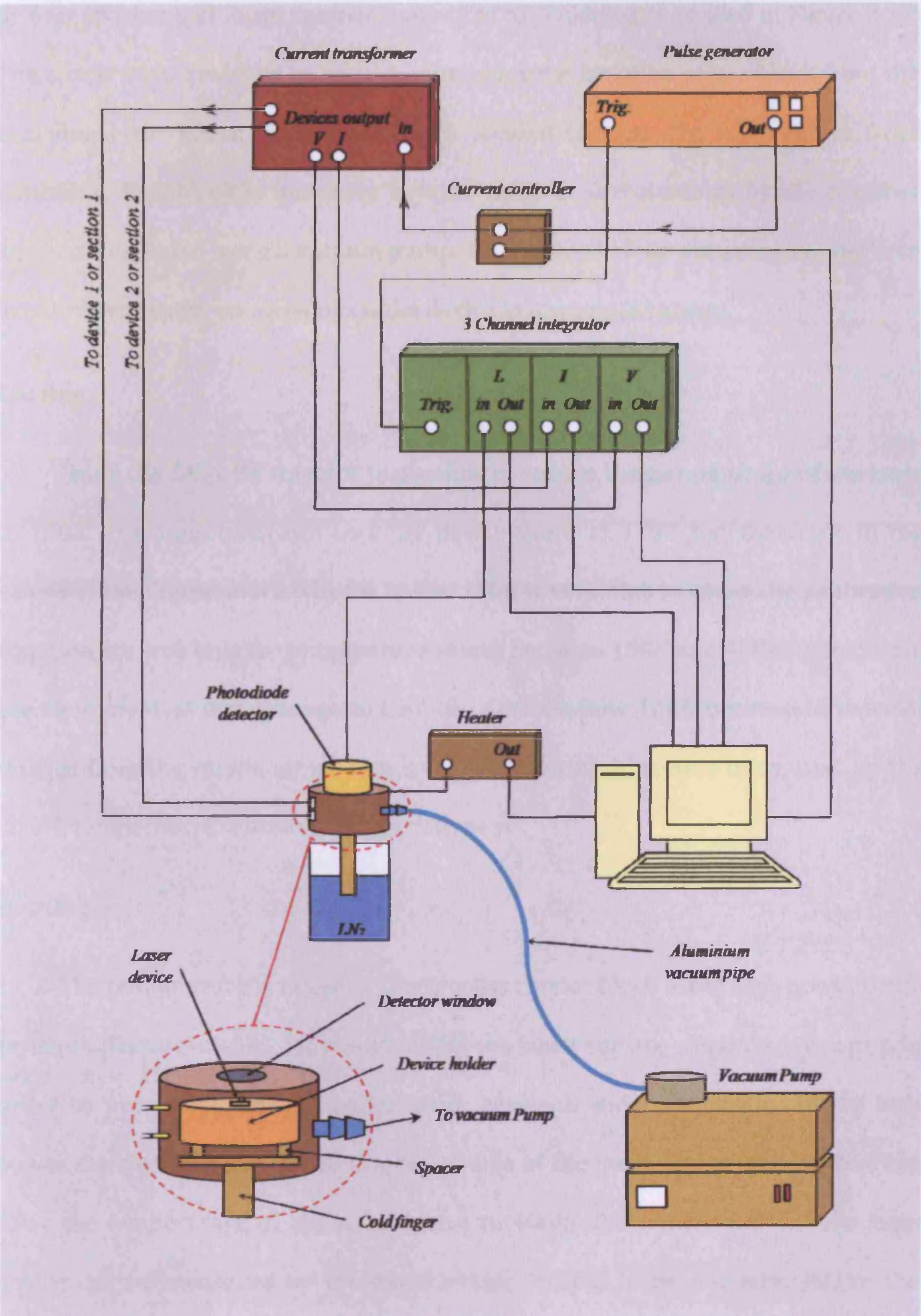

Figure 3.17 *Block diagram for current-voltage-light-temperature experiment.*

by four spacers and these spacers connect to the cold finger as seen in Figure 3.17. The spacers are designed to provide some thermal isolation of the block from the cold finger to reduce the heater power needed to raise the temperature from minimum. This block is thermally isolated from its surroundings by the chamber which is evacuated using a vacuum pump. The purpose of the vacuum chamber is to avoid water vapour condensing on the device at low temperatures.

Cooling

Using the LN_2 cold finger it is possible to reduce the temperature of the laser to $150K$. The equipment can cool the device down to $120K$ but the error in the values of the temperature when it below $150K$ is very high because the calibration equation are true only for temperature values between $150K$ and $400K$. In addition, the equipment cannot manage to cool the device below $120K$ because of thermal leakage from the surroundings such as the various wires needed to connect up the lasers, temperature sensor and heater elements.

Heating

The temperature is raised by heating the copper block using high power rated resistors. These resistors are placed within the block and are connected in series. In order to provide a uniform temperature gradient under the device, these high power resistors are positioned one either side of the laser device. The heaters can raise the temperature of the laser device to $400K$. The temperature of the laser device can be measured by the diode sensor located in the chamber below the position of the laser device, driven by a constant current.

3.6 Spectral Analyses

The spectral analysis is a method of analysing the properties of matter by looking at the bands of their optical spectrum. It is a technique that some equipment use where the light intensity is been plotted against the wavelength.

Here is one of these techniques, which is used to analyse the spectra emitted from the studied structures and from which the lasing wavelength for this structure can be determined. A typical spectral analysis experimental setup which was used to measure the lasing wavelength is shown in Figure 3.18. The pulse generator applied a 1000ns long pulse with a frequency of 1kHz to the laser devices. The two movable stands are used to couple the laser devices with the optical fibre so that the light enters the optical fibre. The optical fibre transmits the light to the

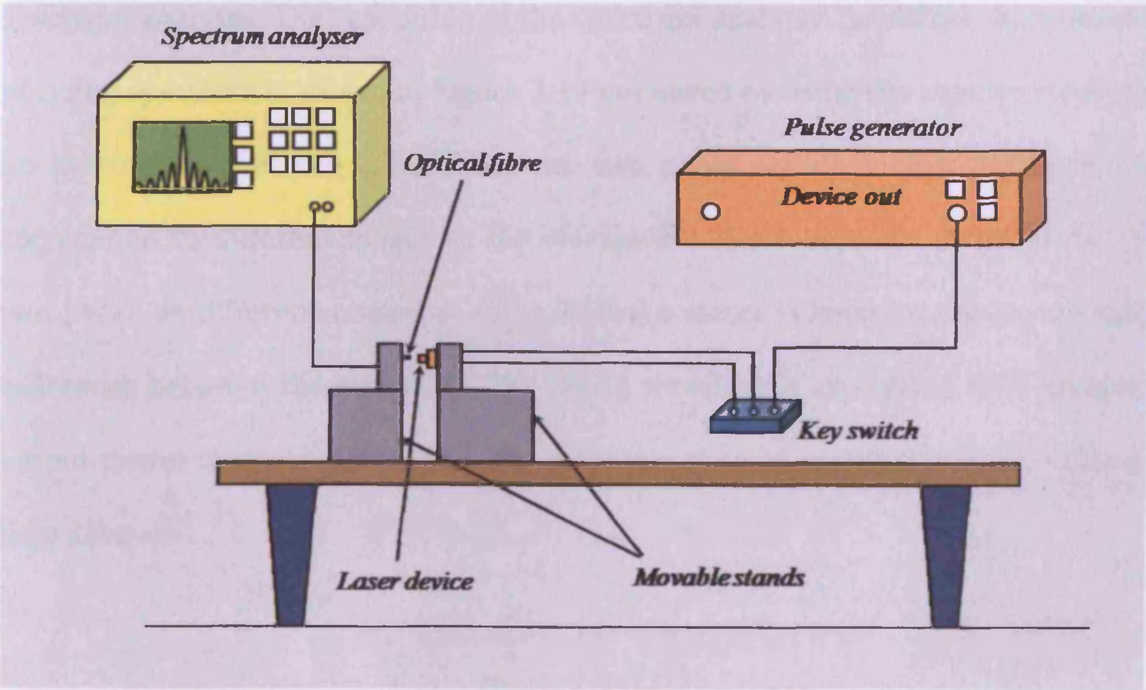

Figure 3.18 *Diagram for the spectral analysis experiment.*

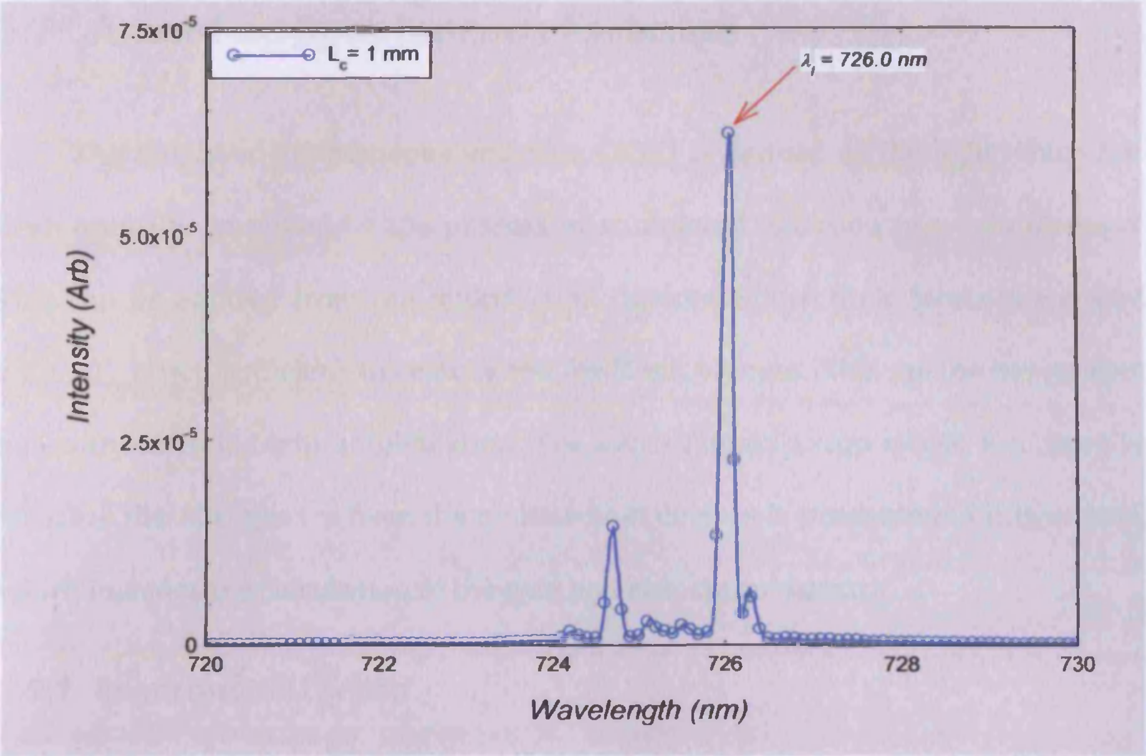

Figure 3.19 *Example of lasing spectrum for laser device pumped with $1.1I_{th}$ at room temperature. The symbol marked on the curve is a guide to the eye.*

spectrum analyser. The resolution of the spectrum analyser is $0.05nm$. An example of lasing spectrum is shown in Figure 3.19 measured by using the experimental set up illustrated in Figure 3.18. There are two peaks shown in this graph which correspond to different modes in the waveguide. The reason for considering the two peaks as different modes and not different states is because the wavelength difference between them is small. The lasing wavelength associated with greatest output power that pumped with 1.1 I_{th} is $726nm$ at room temperature for $1000\mu m$ long device.

3.7 Amplified Spontaneous Emission

The amplified spontaneous emission (ASE) is defined as the light which has been optically amplified by the process of stimulated emission in a gain medium. This can be emitted from the multisection devices where their facets are angled with 10°, which sufficient to remove the feedback process. This means having gain but with no round-trip amplification. The experimental setup which was used to measure the ASE spectra from the multisection devices is presented in this section, which includes the calculation of the gain and absorption spectra.

3.7.1 Experimental Setup

The experimental set up used to measure the ASE spectra of the multisection devices are shown in Figure 3.20. The multisection devices are placed into a vacuum cryostat with the emission direction through a side window in the cryostat. The output light of the multisection devices was directed in to a ×5 magnification lens placed near to the cryostat window to collect only the amplified light to a certain point, then in to a polariser and in to a spectrograph, which separates the incoming light wave into a wavelength spectrum. This spectrum from the spectrograph is detected with a CCD camera which is attached with a cooler used to maintain temperature stability to work efficiently. The temperature can be varied by using a temperature controller and liquid nitrogen LN_2 which flows into the cryostat using a liquid nitrogen transfer tube. The pulse generator applied a 1000*ns* long pulse with a repetition frequency of 1*kHz* to the multisection devices. The second pulse generator is used to operate the CCD camera which applied a 400*ns*

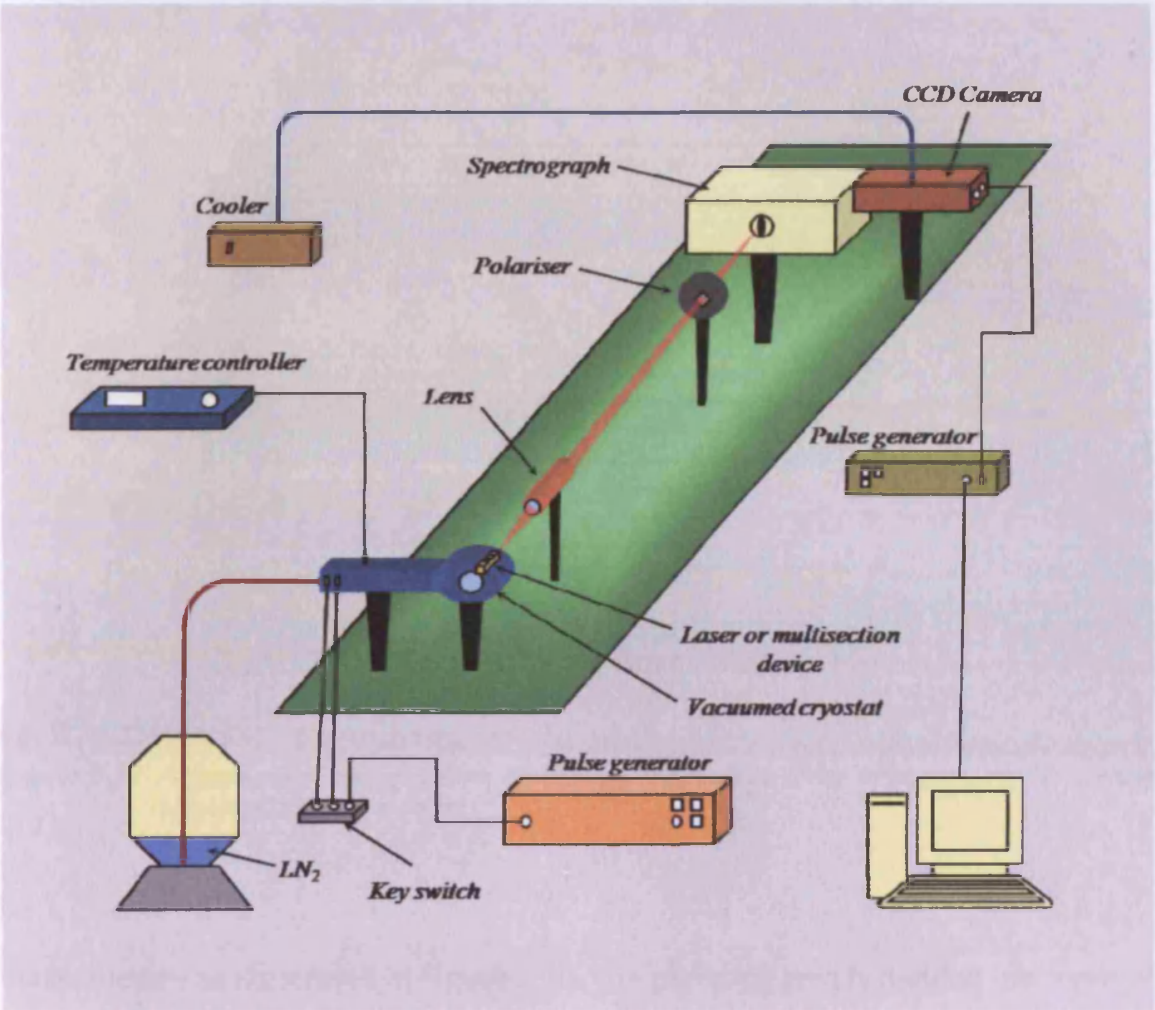

Figure 3.20 *Experiment set up used to measure the amplified spontaneous emissions spectra and spontaneous emission spectra.*

long pulse and adjusted to couple it signal with the signal from the other pulse generator. These signals are fed back to the software program in order to be presented by the computer screen.

3.7.2 Gain and Absorption Measurements

In order to determine the gain and absorption characteristics for a given structure one can use the multisection device processing method fabricated from

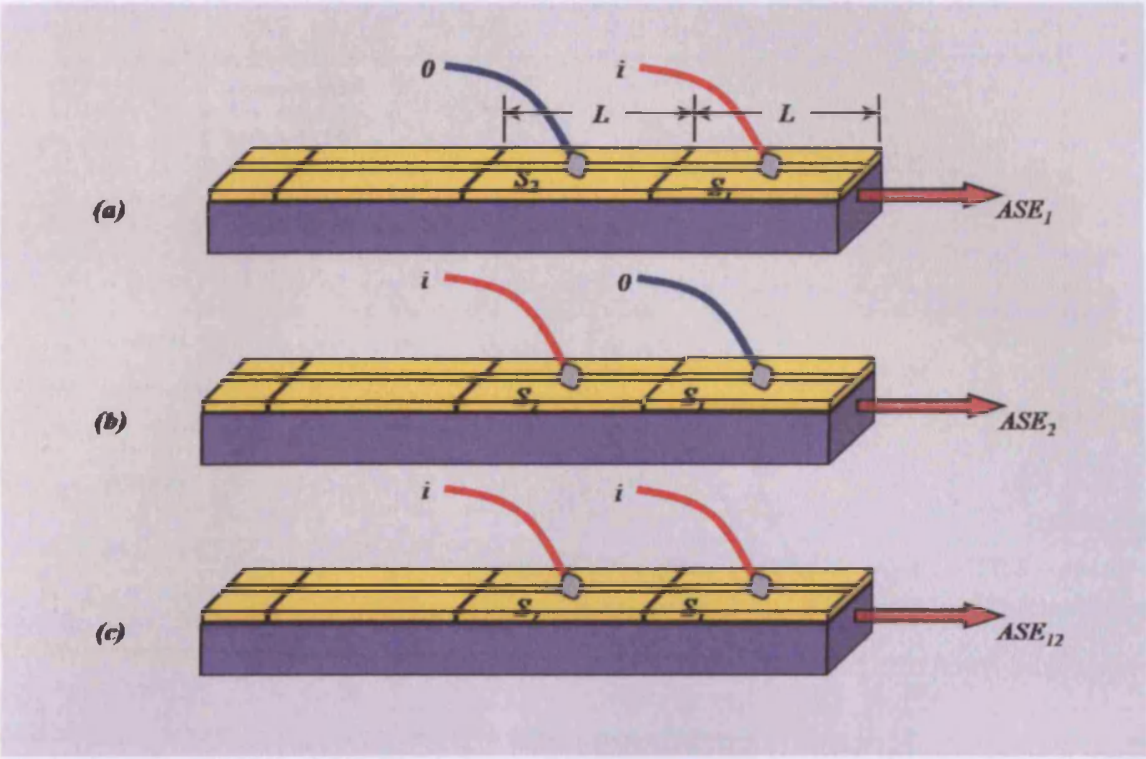

Figure 3.21 *ASE spectrums emerging from the end of a multisection device when pumping (a) section1 (b) section2 (c) both sections.*

that structure as illustrated in Figure 3.10. The pumping area is divided into several sections, each section can be pumped individually and the ASE spectrum is measured from the end of the multisection device. The intensity of the ASE spectrum at the end of a pumped section of length L can be seen [5] in Equation 3.4

$$I_{ASE} = \frac{I_{spon}(e^{(G-\alpha_i)L} - 1)}{G - \alpha_i} \tag{3.4}$$

where I_{spon} is proportional to the spontaneous recombination rate $I_{spon} = CR_{spon}$, C is the coupling coefficient which represents the photon collection geometry of the measurement apparatus, stripe width, spectrometer resolution, and the overall calibration factor of the measurement system.

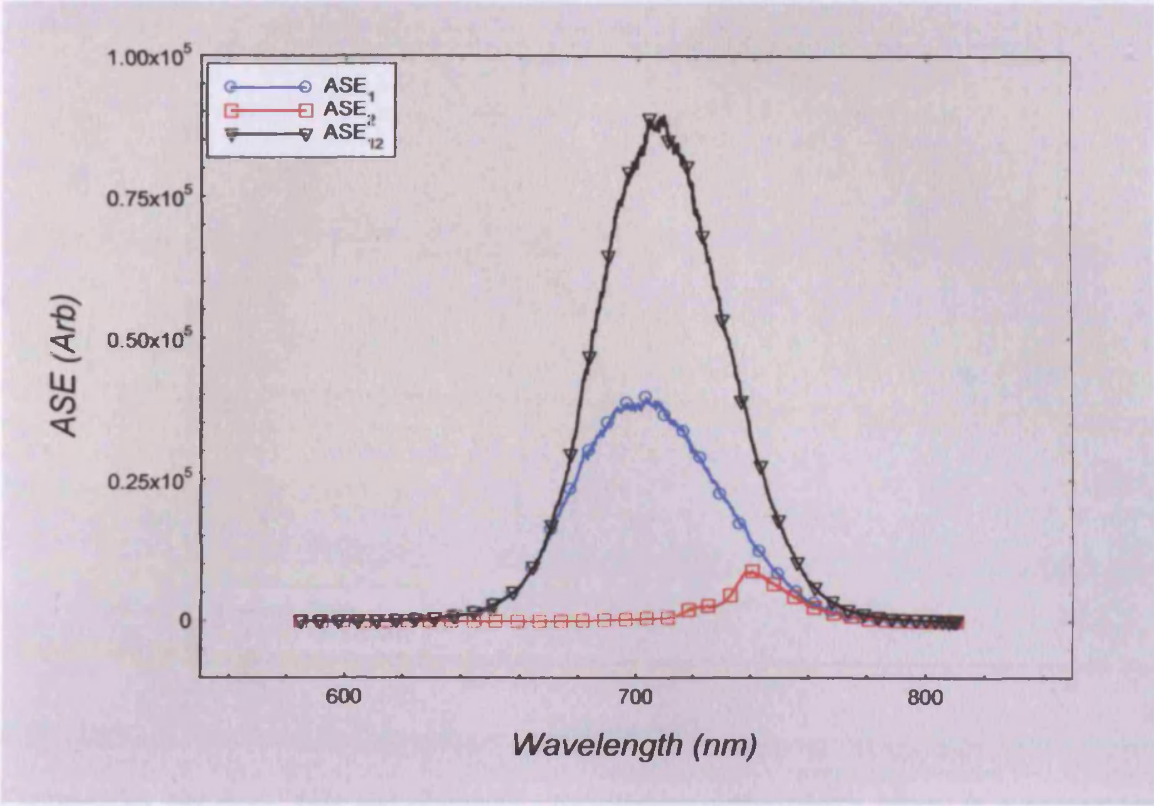

Figure 3.22 *Intensity of ASE spectra verses wavelength in a typical multisection device pumped with 200mA at room temperature. The symbols marked on each curve are a guide to the eye.*

The modal gain and absorption characteristics can be determined by comparing the ASE spectra which emerge from the end of the multisection device when pumping section 1 or section 2 or both as shown in Figure 3.21. As one can see from this figure, ASE_1 emerge when section 1 was pumped, ASE_2 emerge when section 2 was pumped and ASE_{12} emerge when sections 1 and 2 were pumped. The intensities of these ASE measurements can be derived starting with Equation 3.4 to be as follows

$$I_{ASE_1} = \frac{I_{spon}(e^{(G-\alpha_i)L} - 1)}{G - \alpha_i} \tag{3.5}$$

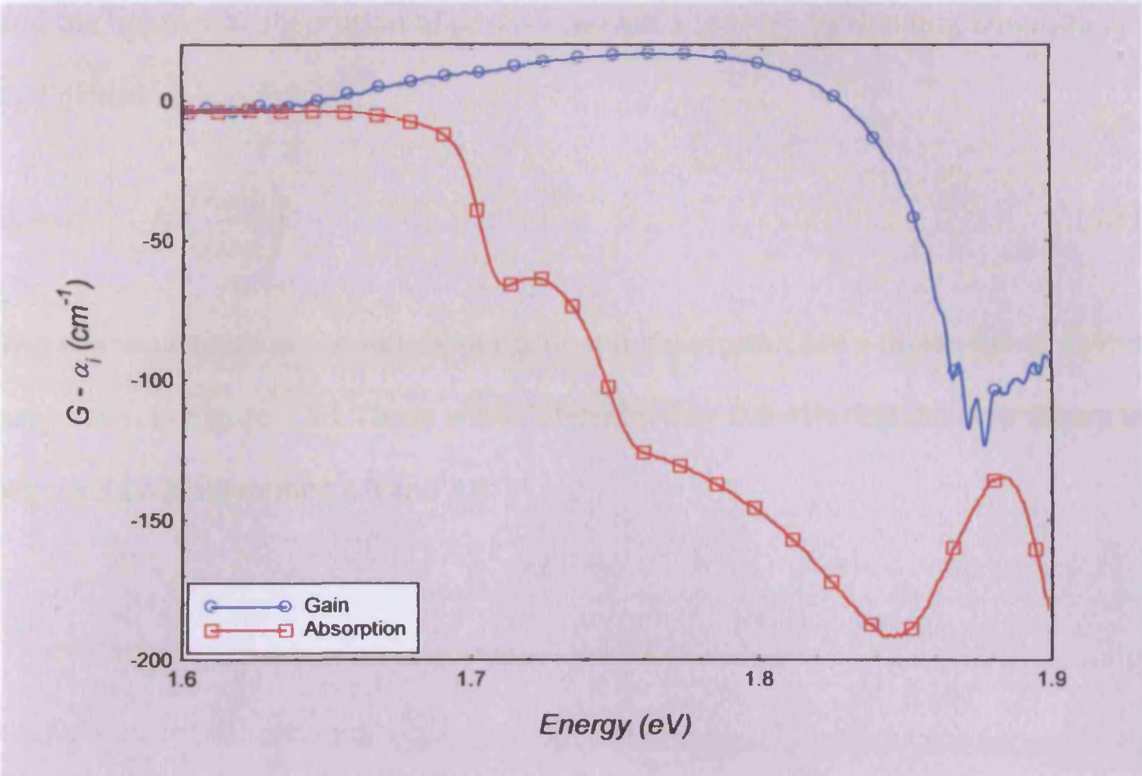

Figure 3.23 *Net model gain and absorption characteristics verses photon energy in a multisection device pumped with 200mA at room temperature. The symbols marked on each curve are a guide to the eye.*

$$I_{ASE_2} = \frac{I_{spon}(e^{(G-\alpha_i)L} - 1)}{G - \alpha_i} \cdot e^{(A-\alpha_i)L} \tag{3.6}$$

$$I_{ASE_{12}} = \frac{I_{spon}(e^{(G-\alpha_i)2L} - 1)}{G - \alpha_i} \tag{3.7}$$

All these ASE intensities are shown in Figure 3.22.

The net modal gain is given by dividing Equation 3.7 by Equation 3.5 as follows

$$G - \alpha_i = \frac{1}{L} ln\left(\frac{I_{ASE_{12}}}{I_{ASE_1}} - 1\right) \tag{3.8}$$

and the net modal absorption of passive section 1 is given by dividing Equation 3.6 by Equation 3.5 as follows

$$A - \alpha_i = \frac{1}{L} ln\left(\frac{I_{ASE_2}}{I_{ASE_1}}\right) \tag{3.9}$$

The characteristics of the net model gain and absorption for a multisection device are shown in Figure 3.23. These were determined by substituting the data shown in Figure 3.22 in Equations 3.8 and 3.9.

3.8 Spontaneous Emission

The spontaneous emission, as explained in Chapter 2, is defined as the process by which the carriers in the excited state relaxed spontaneously into the ground state and emit a photon. The measurements of the spontaneous emission are obtained from the top window of the laser devices. It can be used to analyse the studied structures, particularly when it plotted against the wavelength. It could give us information about the carriers and how they are distributed in the structure during pumping. Before taking measurement for spontaneous emission the system spectral response must be calibrated.

3.8.1 System Response Calibration

In order to measure the actual spontaneous emission emitted from the top windows of the laser device, a system response correction is required. This can be done by using a standard lamp. The intensity as a function of wavelength is given by lamp manufacturer along with other circumstances that should be taken in account. The correction is calculated by dividing the manufacturer data by the measured data taken for that lamp.

3.8.2 Spontaneous Emission Spectra

The spontaneous emission spectra are very important for analysing a given structure in terms of radiative and nonradiative currents. The intensity of the spontaneous emission is in arbitrary units which can be normalised to a certain level in order to compare these measurements for various structures. Usually it is

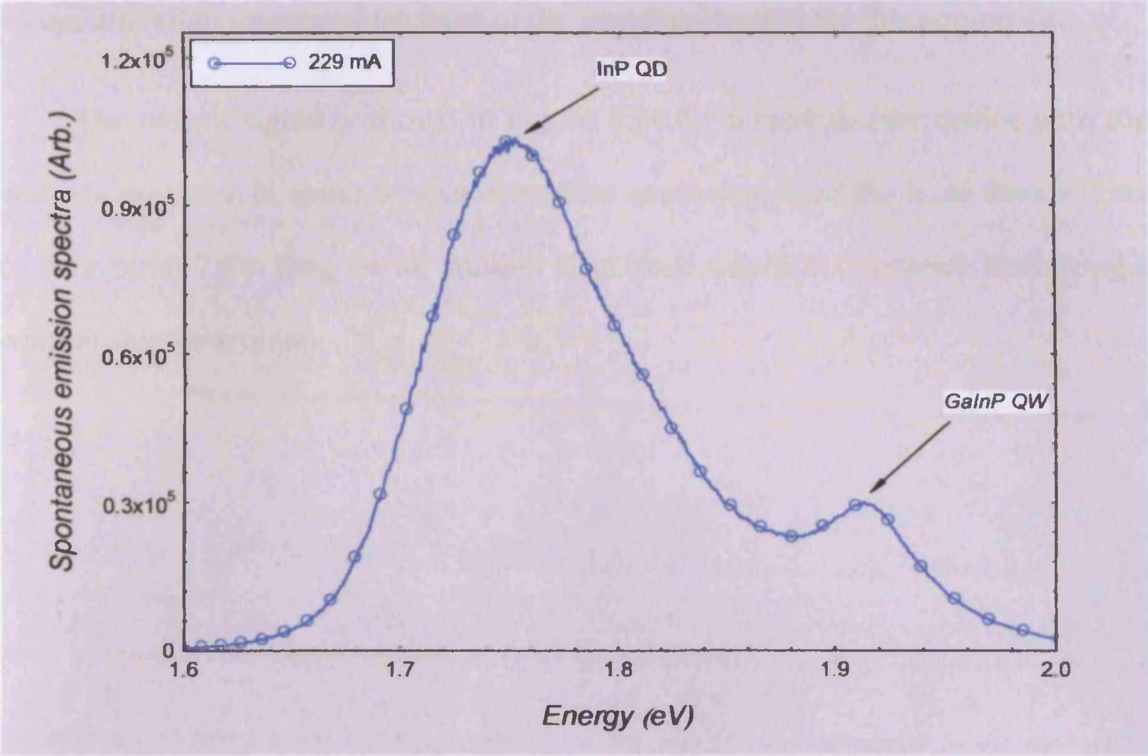

Figure 3.24 *Spontaneous emission verses photon energy in a 2mm long laser device with window emission at room temperature. The symbol marked on the curve is a guide to the eye.*

normalised to the lowest energy peak.

The experimental set up used to measure the spontaneous emission spectra of laser devices is shown in Figure 3.20. The laser devices are placed into a vacuum cryostat with the top window emission directed through a side window in the cryostat. The output light of the laser top window was directed in to a ×10 magnification lens placed near to the cryostat window to collect the photons to a certain point, then into a spectrograph. The outgoing light from the spectrograph was detected with a CCD camera. The temperature can be varied by following the same procedures written in the previous section for this equipment. The pulse generators are applied to both the laser device and the CCD camera with the same values and adjustments which used in the previous section for this equipment.

The output signal is shown in Figure 3.24 for a typical laser device with top window emission at room temperature. The cavity length of the laser device is set to be around 2mm long for all studied structures which is necessary for having a comparable structures.

3.9 Summary

In this chapter the device structures which have been used for measurements in this thesis were presented. The chapter begun by introducing the materials used to construct these structures. The chapter described the device preparation which transforming these structures in to working laser or multisection devices. The chapter illustrated how these devices can be mounted in order to make them suitable for testing which is the last step required for checking how good these devices are.

The experimental procedures and equipments used in this thesis were also presented. These were used to measure and evaluate the data presented in the following chapters. These include experiments for measuring the threshold current and spontaneous emission by using the laser device, the optical gain and absorption by using the multisection device. The experiments ware undertaken in pulsed mode in order to avoid the raise of heating effects during measurements.

References

[1] Y. P. Varshni, "*Temperature dependence of the energy gap in semiconductors*", Physica Amsterdam 34, 149 (1967).

[2] I. Vurgaftman, J. R. Meyer and L. R. Ram-Mohan, "*Band parameters for III–V compound semiconductors and their alloys*", J. Appl. Phys. 89, 11 (2001).

[3] L. A. Coldren and S. W. Corzine, "*Diode laser and photonic Integrated circuits*", *Wiley and Sons*, New York, (1995).

[4] EPSRC National Centre for III-V Technologies web site - MOVPE (As,P)- right hand side downloads [*http://www.shef.ac.uk/eee/nc35t/MOVPEepi.pdf*].

[5] P. Blood, G.M Lewis, P.M. Smowton, H.D. Summers, J.D. Thomson, J. Lutti, "*Characterization of Semiconductor Laser Gain Media by the Segmented Contact Method*", IEEE J. Sel. Top. Quant. Elect., 9, pp.1275-1282 (2003).

CHAPTER 4

Effect of Barrier Width and Growth Temperature

4.1 Introduction

This chapter presents the data taken from several experiments using seven structures, which vary in both the barrier width and growth temperature, to study the effect of barrier width and growth temperature on optoelectronic properties of InP/AlGaInP quantum dot laser diodes. Interpretation of this data is also given.

This chapter begins by introducing the device structures used. The threshold current density around room temperature is evaluated including narrow and wide barrier widths. The chapter describes the optical absorption and gain spectra using the amplified spontaneous emission emitted from multisection devices. This explains the behaviour of the threshold current density in structures grown at low temperatures and verifies the threshold current density values by comparing the gain-current relations obtained from both the laser and multisection devices. Afterwards, the chapter describes the spontaneous emission spectra taken for all structures at the same pumping, which is obtained from the gain spectra, to explain carrier loss in structures grown at high temperatures. The chapter describes the lasing wavelength and ends with summarising the effect of both barrier width and growth temperature on InP/AlGaInP quantum dot laser diodes using the data presented in the chapter by different experiments.

4.2 Device Structures

The device structures used in this chapter to study the effect of barrier width and growth temperature are described in this section. The device structures detail are illustrated in Figure 3.7 Chapter 3 and listed in Table 3.5 Chapter 3. The bandgap energy diagram versus growth distance for these structures is shown in Figure 3.8 Chapter 3. There are seven structures used and they are similar but vary in two parameters. These parameters are the width of the barriers and the temperature at which the wave guide core is grown. In this chapter, the comparison of two main barrier widths of 8*nm* and 16*nm* $(Al_{0.3}Ga_{0.7})_{0.51}In_{0.49}P$, which separate 5 dot layers, is studied. Each of these dot layers was formed from 2 monolayers of InP grown on $(Al_{0.3}Ga_{0.7})_{0.51}In_{0.49}P$ and covered by 8nm $Ga_{0.51}In_{0.49}P$ quantum well layers. The comparison also will include results for these structures at different growth temperatures of 690°*C*, 710°*C*, 730°*C* and 750°*C* for each barrier width.

The device structures were processed into multisection devices to measure the amplified spontaneous emission and also oxide isolated stripe lasers with top windows to measure the threshold current density as well as spontaneous emission as was described in Chapter 3.

4.3 Threshold Current Density

The threshold current density for structures with narrow 8*nm* and wide 16*nm* barriers is studied in this section. The section starts by describing changes in the light-current characteristics, and therefore threshold current, around room temperature.

4.3.1 Threshold Current

The light-current characteristics have been investigated using the current voltage light temperature I-V-L-T measurement experiment, which is described in Chapter 3. In the light-current characteristic curve the starting point of lasing is the

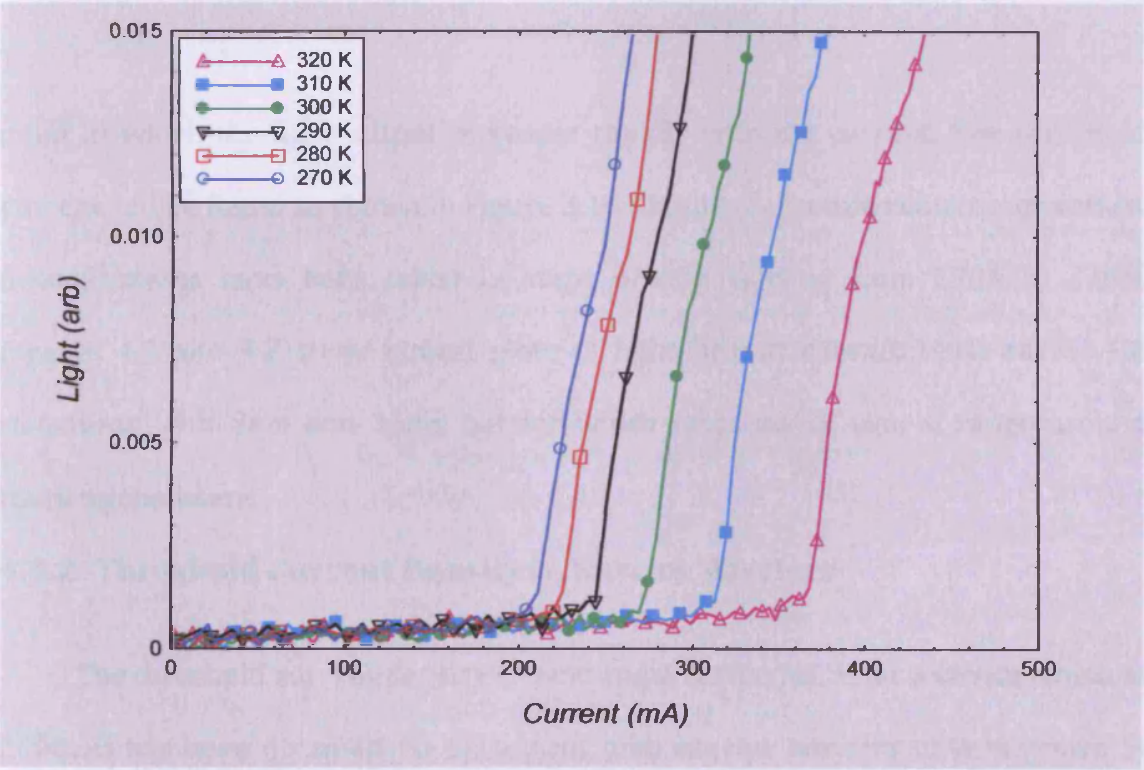

Figure 4.1 *Light-current characteristic curves for structure with 8nm barrier width grown at 730°C. The symbols marked on each curve are a guide to the eye.*

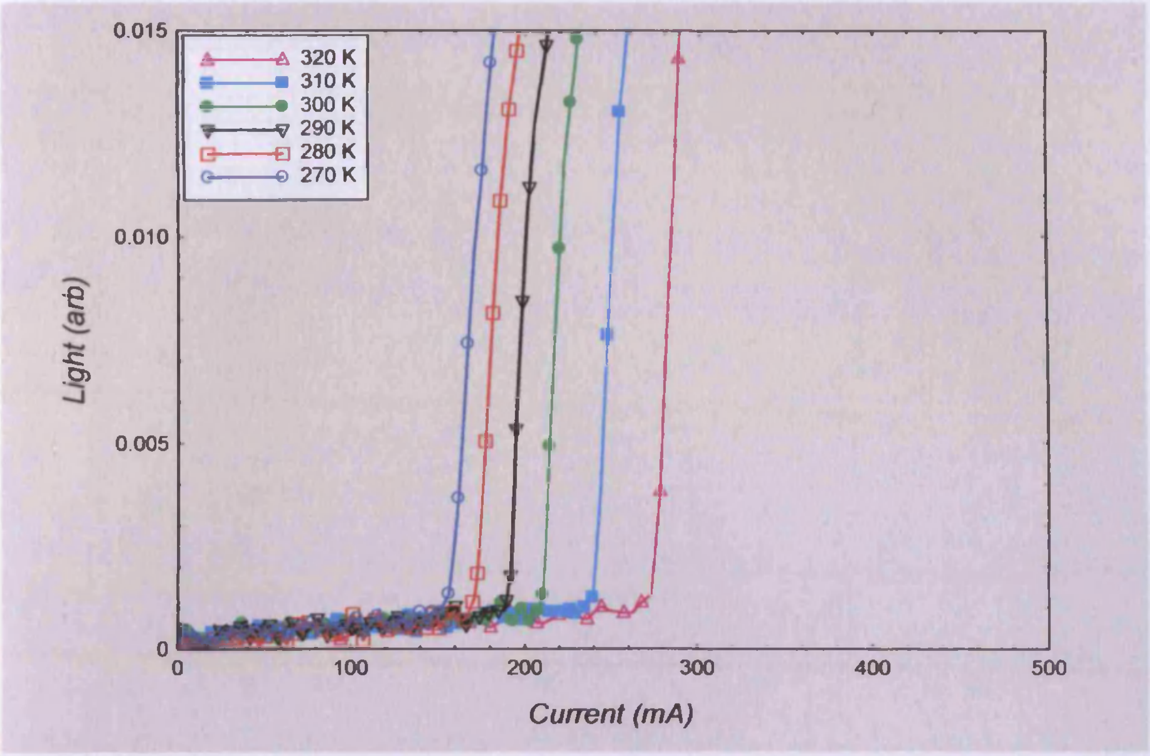

Figure 4.2 *Light-current characteristic curves for structure with 16nm barrier width grown at 710°C. The symbols marked on each curve are a guide to the eye.*

point at which the light output increases rapidly with the current. The threshold current can be found as shown in Figure 3.16 Chapter 3. Around room temperature, measurements have been taken in steps of $10K$ starting from $270K$ to $320K$. Figures 4.1 and 4.2 show typical plots of light-current characteristic curves for structures with $8nm$ and $16nm$ barrier width respectively over a range around room temperature.

4.3.2 Threshold Current Density in Narrow Barriers

The threshold current density around room temperature for a device length of $2000\mu m$ has been obtained for structures with narrow barriers of $8nm$ grown at temperatures of $690°C$, $710°C$, $730°C$ and $750°C$ from the light-current characteristic

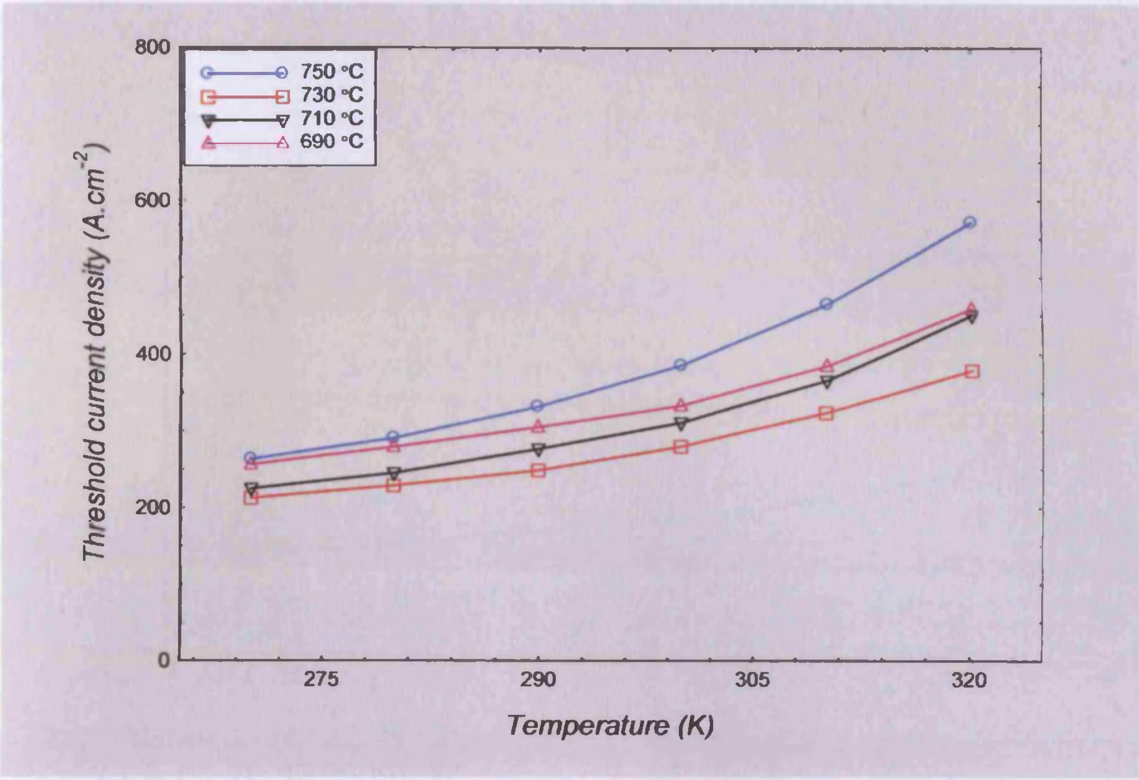

Figure 4.3 *Threshold current density around room temperature for structures with 8nm barrier width grown at different temperatures.*

curves, Figure 4.1. Therefore the threshold current densities for the light-current characteristic curves which were illustrated in Figure 4.1 and 4.2 can be evaluated. Figure 4.3 shows a nonlinear increase to the threshold current density as the temperature increases around room temperature for all structures. The threshold current densities in Figure 4.3 show a minimum value for structure grown at 730°*C*. The value increases in structures grown at temperatures above and below 730°*C*. These behaviours shown in Figure 4.3 will be discussed later in this chapter.

4.3.3 Threshold Current Density in Wide Barriers

The plot of the threshold current density around room temperature for

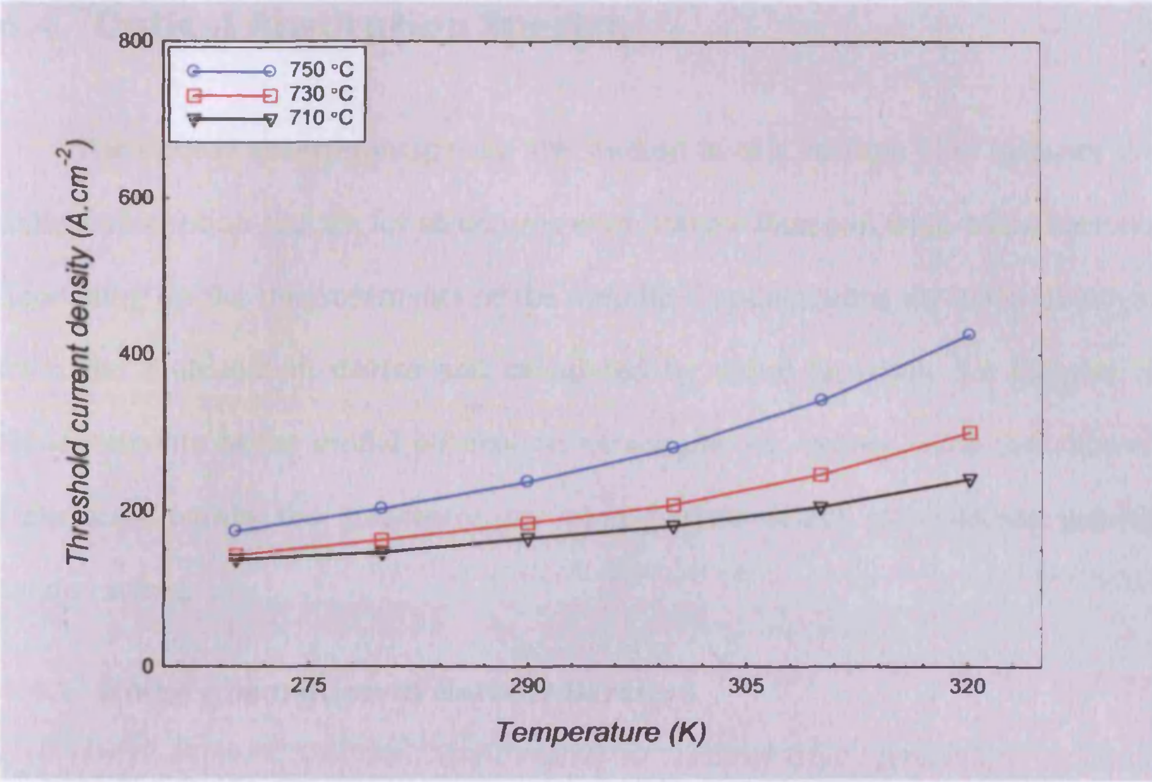

Figure 4.4 *Threshold current density around room temperature for structures with 16nm barrier width grown at different temperatures.*

structures with wide barriers grown at different temperatures and with cavity length of $2000\mu m$ is shown in Figure 4.4. This figure also shows a nonlinear increase to the threshold current density as the temperature increases around room temperature for all structures. The threshold current densities in Figure 4.4 at fixed measurement temperature show a nonlinear increase with the growth temperature, the lowest value is for structure grown at $710^{\circ}C$. These behaviours shown in Figure 4.4 will be discussed later in this chapter.

4.4 Optical Absorption Spectra

The optical absorption spectra are studied in this section. This includes the optical absorption spectra for structures with narrow $8nm$ and wide $16nm$ barriers depending on the measurements of the amplified spontaneous emission obtained from the multisection device and calculated by using Equation 3.9 Chapter 3. Measurements of the modal absorption verses photon energy show the allowed transitions within the structures for each barrier width at different growth temperatures.

4.4.1 Modal Absorption in Narrow Barriers

The absorption spectra for structures with barrier width of $8nm$ grown at temperatures of $690°C$, $710°C$, $730°C$ and $750°C$ are plotted in Figure 4.5. Previous studies shows that InP quantum dots grown on GaInP can be formed with three dot size distributions, small, large and very large dots. The small and large dots are coherently strained while the very large dots are associated with defects in the material [1], [2]. As a result of this, the inhomogenously broadened transitions in Figure 4.5 identify with the ground and excited state of a large dot size subset and a small dot size subset, of a bimodal dot size distribution, are labeled. As the growth temperature is increased, the features associated with the inhomogenously broadened transitions shift to higher energy and decrease in magnitude. This is due to the decrease in the size and density of the large dot size subset. The change in the size of the dots causes a change in the energy of the dot states which is observed as a shift in the photon energy of absorption spectra whereas the change in the

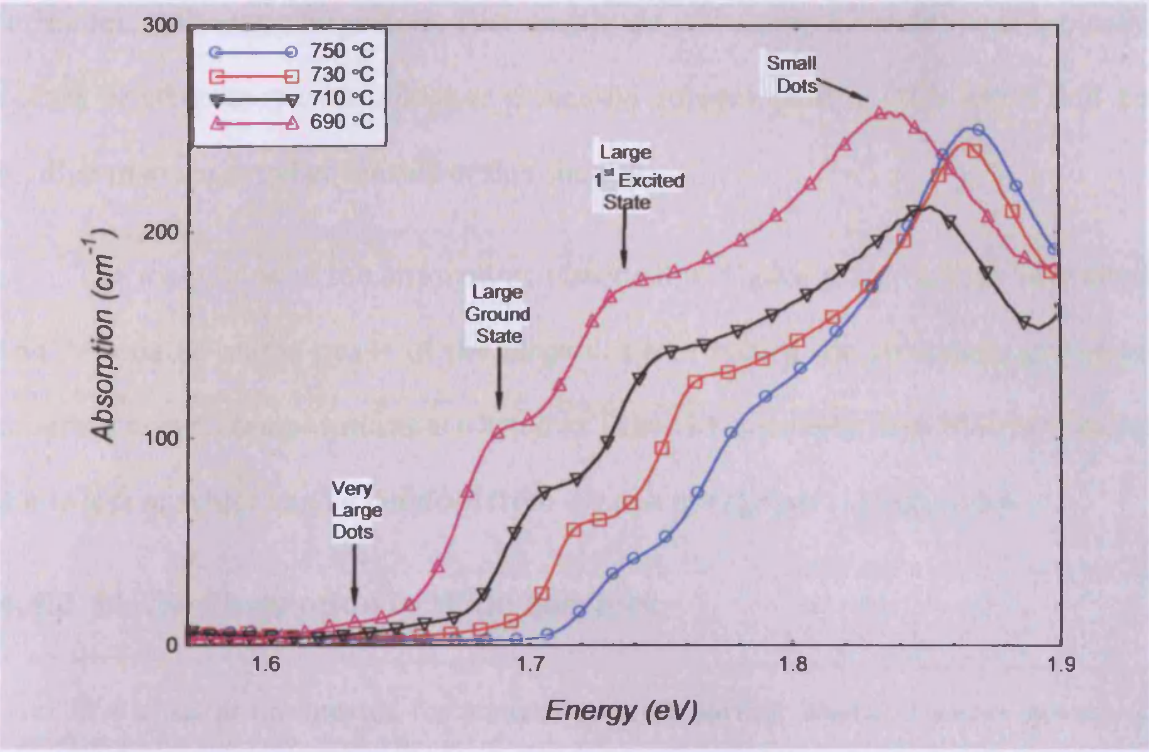

Figure 4.5 *Modal absorption versus photon energy for structures with 8nm barrier. The symbols marked on each curve are a guide to the eye.*

density of the dots cause a change in the state availability which lead to the change in modal absorption magnitude of the absorption spectra.

There is also a small absorption signal at lower energies in Figure 4.5 which increases in structures with decreasing growth temperature and identified with the

Growth temperature	Absorption at energy of large dot ground state peak (cm^{-1})	Absorption at energy of large dot 1st excited state peak (cm^{-1})	α_i (cm^{-1})
690°C	104.1	171.6	3.3
710°C	72.5	139.9	2.9
730°C	59.0	130.9	3.8
750°C	36.9	109.7	3.6

Table 4.1 *Large dot ground and excited states peak values for structures with 8nm barrier width.*

formation of the very large dots. The magnitude of the very large dot peak typically occurs in structures with a higher threshold current density. This effect will be studied in more detail at the end of this chapter.

The magnitude of the absorption, observed in Figure 4.5, at energy of ground and 1st excited states peaks of the large dot size subset for structures grown at different growth temperatures are listed in Table 4.1 including their internal optical mode loss α_i, which can be deduced from the low energy part of Figure 4.5.

4.4.2 Modal Absorption in Wide Barriers

The absorption spectra for structures with barrier width of 16*nm* grown at temperatures of 710°*C*, 730°*C* and 750°*C* are plotted in Figure 4.6. The absorption spectra for these structures show similar trends to that for structures with 8*nm* barrier width. The magnitude of absorption for structures with 16*nm* barrier width at the low energy states is both narrower and larger than that in structures with 8*nm* barrier width. Moreover, the magnitude of absorption for structures with 16*nm* barrier width at the very low energy states, which is believed correspond to very large dots, have small and decreased magnitudes as compared to structures

Growth temperature	Absorption at energy of large dot ground state peak (cm^{-1})	Absorption at energy of large dot 1st excited state peak (cm^{-1})	α_i (cm^{-1})
710°C	78.7	131.5	3.0
730°C	66.3	125.3	3.5
750°C	39.9	109.0	4.0

Table 4.2 *Large dot ground and excited states peak values for structures with 16nm barrier width.*

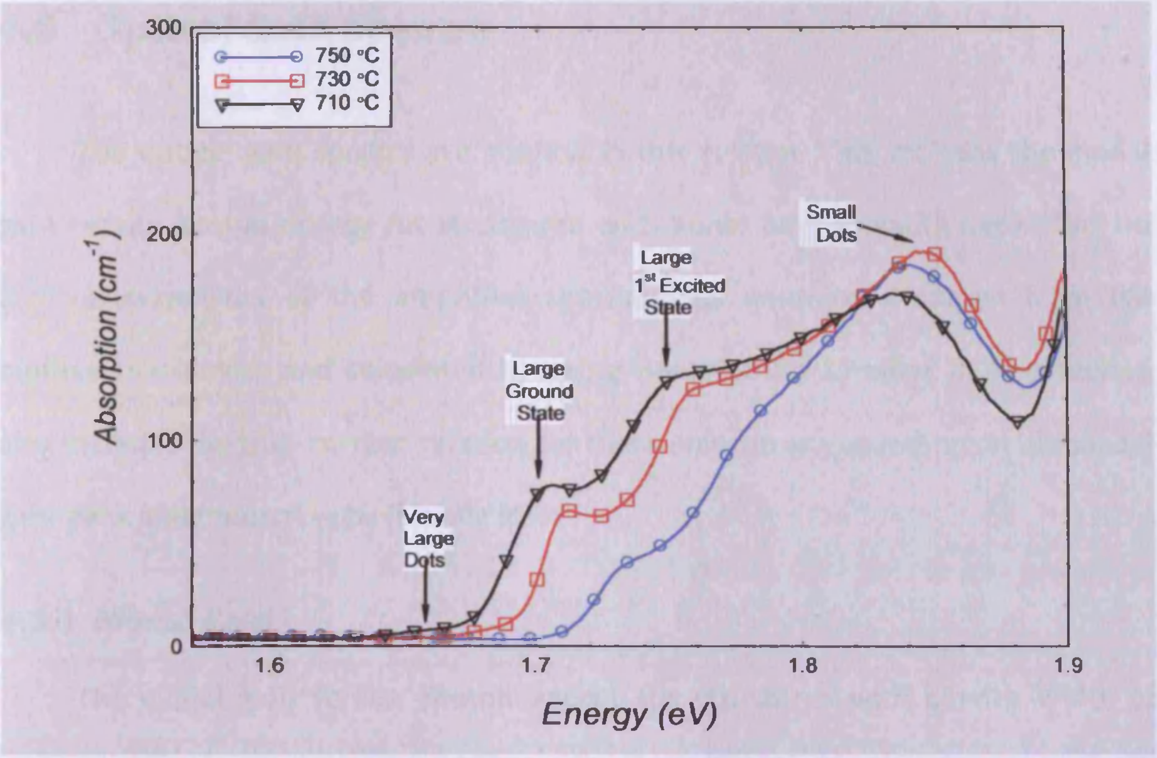

Figure 4.6 *Modal absorption versus photon energy for structures with 16nm barrier. The symbols marked on each curve are a guide to the eye.*

with 8*nm* barrier width. This can be seen when comparing both Figures 4.5 and 4.6. This implies that the effect on threshold current density from the very large dots in structures with 16*nm* barrier width may be less than that in 8*nm* barrier width structures.

The magnitude of the absorption, observed in Figure 4.6, at energy of ground and 1st excited states peaks of the large dot size subset for structures grown at different growth temperatures are listed in Table 4.2. This table includes the internal optical mode loss α_i for these structures. From Tables 4.1 and 4.2, the magnitude of the absorption at different energies is not the same for 1st excited states to ground states due to the overlapping spectra with other dot size states.

4.5 Optical Gain Spectra

The optical gain spectra are studied in this section. This includes the modal gain versus photon energy for structures with 16*nm* barrier width depending on the measurements of the amplified spontaneous emission obtained from the multisection device and calculated by using Equation 3.8 Chapter 3. This section also includes the gain-current relation for these structures depending on the modal gain peak and internal optical mode loss.

4.5.1 Modal Gain

The modal gain versus photon energy for structures with barrier width of 16*nm* grown at temperatures of 710°*C*, 730°*C* and 750°*C* are plotted in Figures 4.7, 4.8 and 4.9 respectively. These are taken at different injected currents at room temperature and calculated from the amplified spontaneous emission obtained from the multisection devices of these structures as described in Chapter 3. The inhomogenously broadened gain transitions shown in Figures 4.7, 4.8 and 4.9 can be identified with the ground and excited states of a large dot size subset. They are very broad spectra and the emission from the ground and excited states of the large dot size subset are hard to distinguish.

The internal optical mode loss α_i can be deduced from the low energy part of the gain spectra which agree with the low energy part of absorption spectra described in the previous section. It shows values of 3.0, 3.5 and 4.1cm^{-1}, as seen in Table 4.3, for structures with 16*nm* barrier width grown at 710°*C*, 730°*C* and 750°*C* respectively. The uncertainty in these values is about ±1cm^{-1}. The gain spectra can

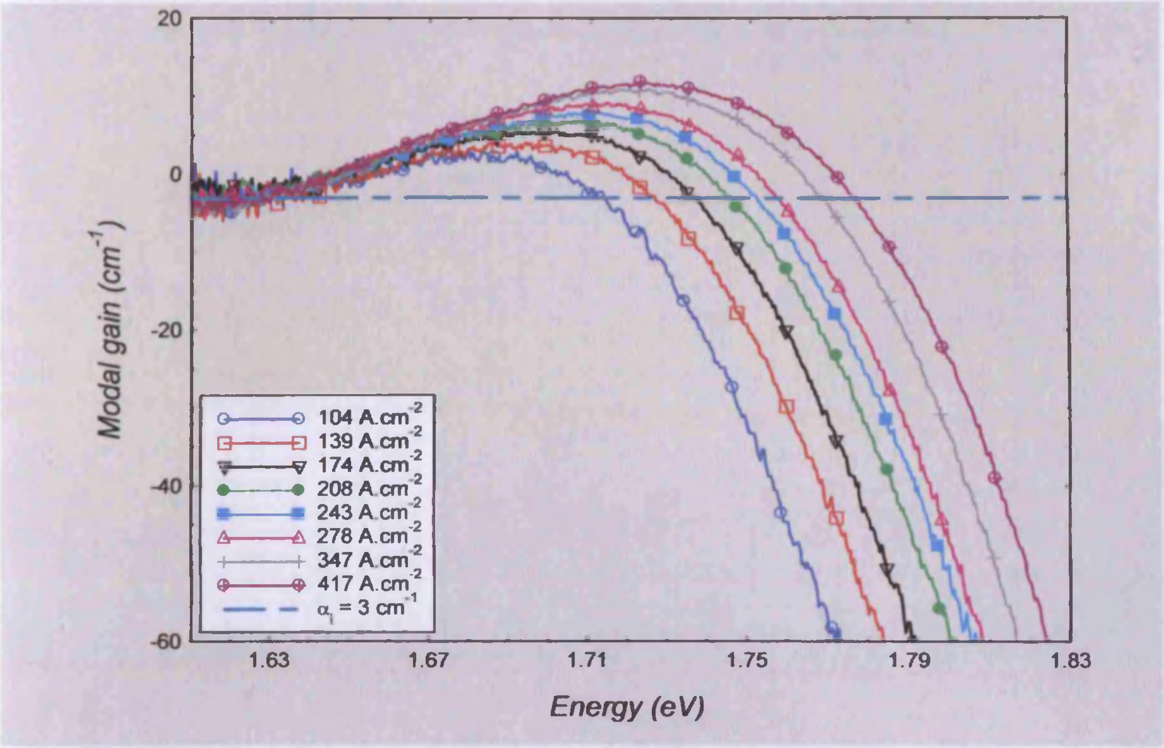

Figure 4.7 *Modal gain versus photon energy for structure with 16nm barrier width grown at 710°C. The symbols marked on each curve are a guide to the eye.*

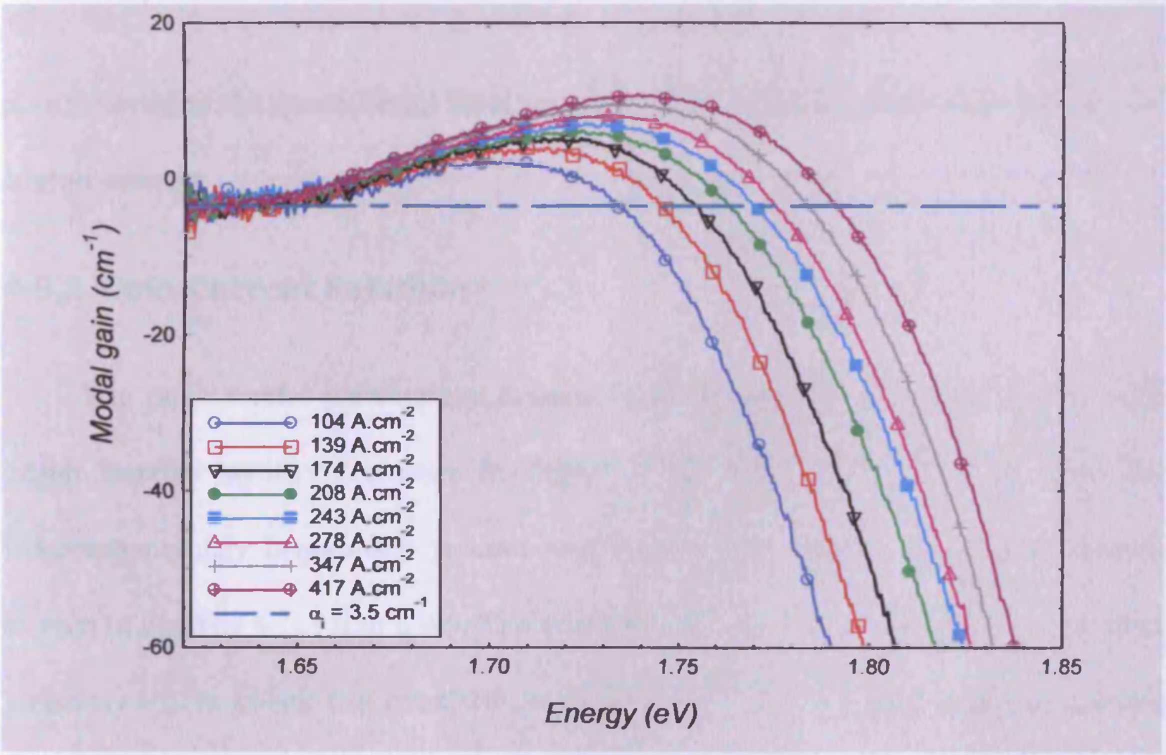

Figure 4.8 *Modal gain versus photon energy for structure with 16nm barrier width grown at 730°C. The symbols marked on each curve are a guide to the eye.*

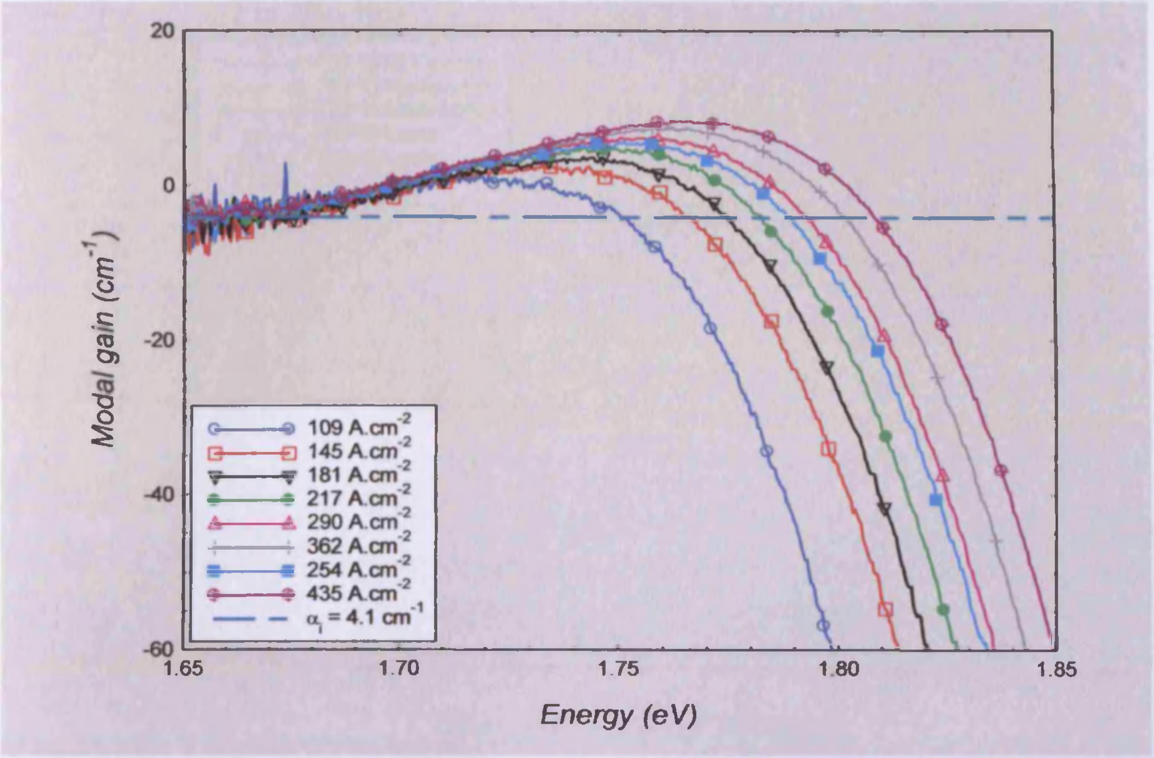

Figure 4.9 *Modal gain versus photon energy for structure with 16nm barrier width grown at 750°C. The symbols marked on each curve are a guide to the eye.*

also determine the quasi-Fermi level separation ΔE_f when the gain value equals α_i at higher energy.

4.5.2 Gain-Current Relations

The peak modal gain versus drive current characteristic for structures with 16*nm* barrier width is shown in Figure 4.10. These are obtained from the inhomogeneously broadened ground and excited state peaks of the gain spectra shown in Figures 4.7, 4.8 and 4.9. The studying of the gain-current relation of these structures is to check the consistency of their threshold current densities, which were obtained from the laser devices, with these obtained from the multisection

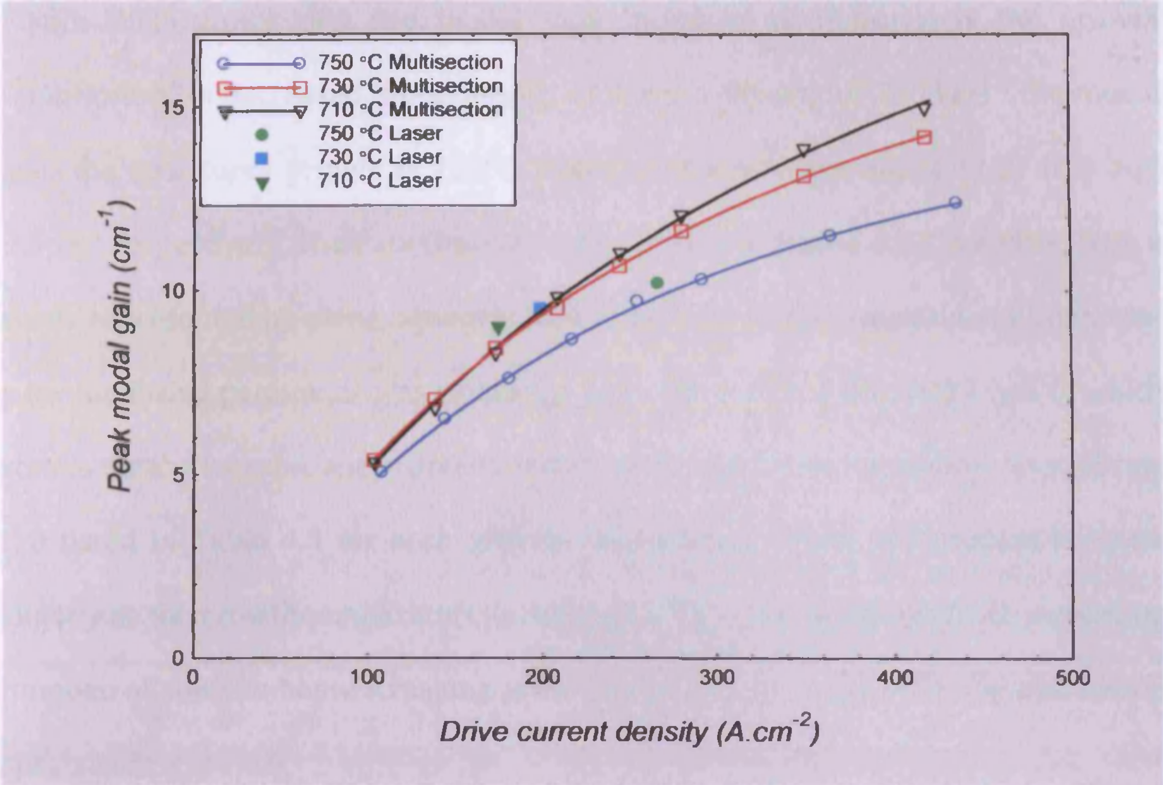

Figure 4.10 *Gain-current relations for structures with 16nm barrier width. The (solid points) are the gain-current of the lasers at room temperature. The lines are fits of Equation 2.22 of the multisection data.*

devices, which seems to be true within error as in Figure 4.10, where the error is $\pm 1 cm^{-1}$. The points in the figure are from the laser devices with different growth temperatures calculated by using Equation 2.12 Chapter 2, which depend on cavity length, internal optical mode loss α_i and reflectivity of the facets R. In addition,

Growth temperature	J_t $(A.cm^{-2})$	G_s (cm^{-1})
710°C	15.4 ± 0.5	20.4 ± 0.5
730°C	13.2 ± 0.5	17.8 ± 0.5
750°C	11.8 ± 0.5	14.7 ± 0.5

Table 4.3 *Transparency current density and modal gain saturation list for structures with 16nm barrier width.*

Figure 4.10 shows that the modal gain increases nonlinearly as the growth temperature is decreased, for example, at current density of $250 A.cm^{-2}$ the modal gain for structures grown at $710°C$, $730°C$ and $750°C$ are about 11.2, 10.9 and $9.5 cm^{-1}$ respectively. The data characteristics shown in Figure 4.10, are fitted with a curve represented by using Equation 2.22 Chapter 2. In this equation, the constants γ for the fitting parameter was estimated to be about 0.052 whereas J_t and G_s which stands for the transparency current density and modal gain saturation respectively are listed in Table 4.3 for each growth temperature. These parameters increase slightly as the growth temperature is reduced. This is consistent with the increasing number of states when decreasing growth temperature as seen in the absorption spectra of Figure 4.6.

4.6 Spontaneous Emission Spectra

The spontaneous emission spectra are studied in this section. This includes the spontaneous emission spectra for structures with narrow 8*nm* and wide 16*nm* barriers depending on the measurements of the spontaneous emission obtained from the top window of the laser devices. Measurements of the spontaneous emission show where are the carriers exist within the structures for each barrier width grown at different temperatures.

4.6.1 Selection of Currents

In order to compare spontaneous emission spectra of different structures, the injected current densities, at which these spontaneous emission spectra were

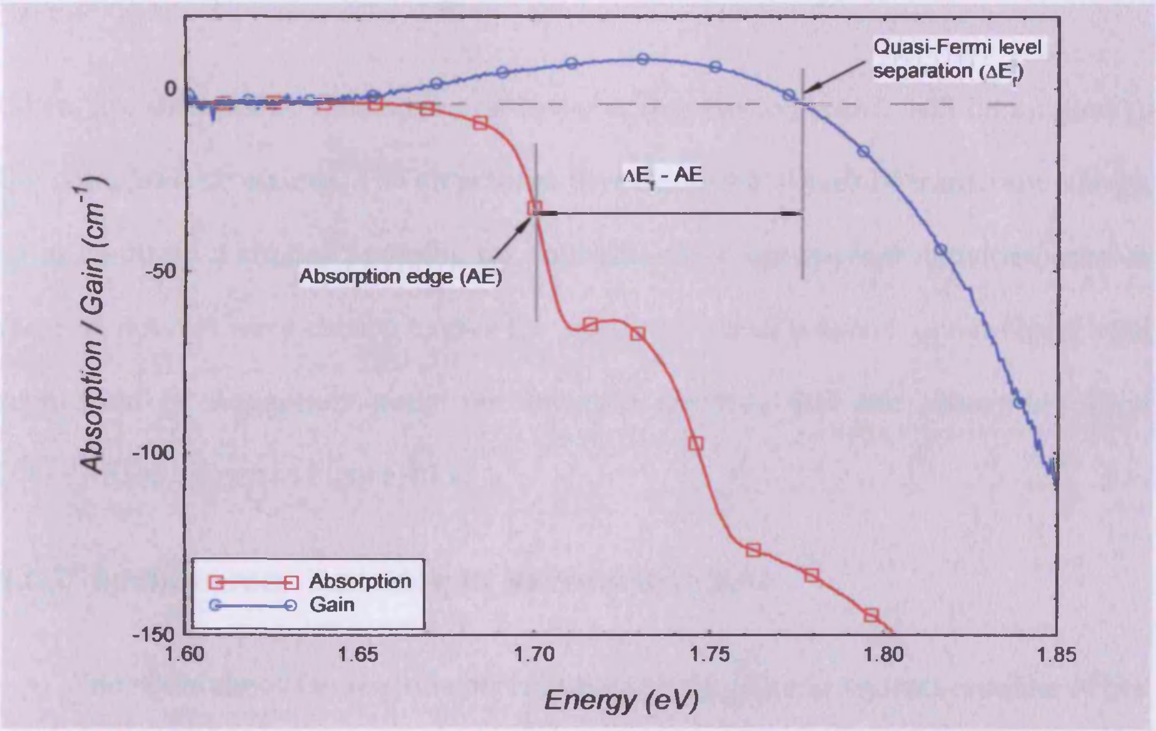

Figure 4.11 *Difference between quasi-Fermi level separation and absorption edge. The symbols marked on each curve are a guide to the eye.*

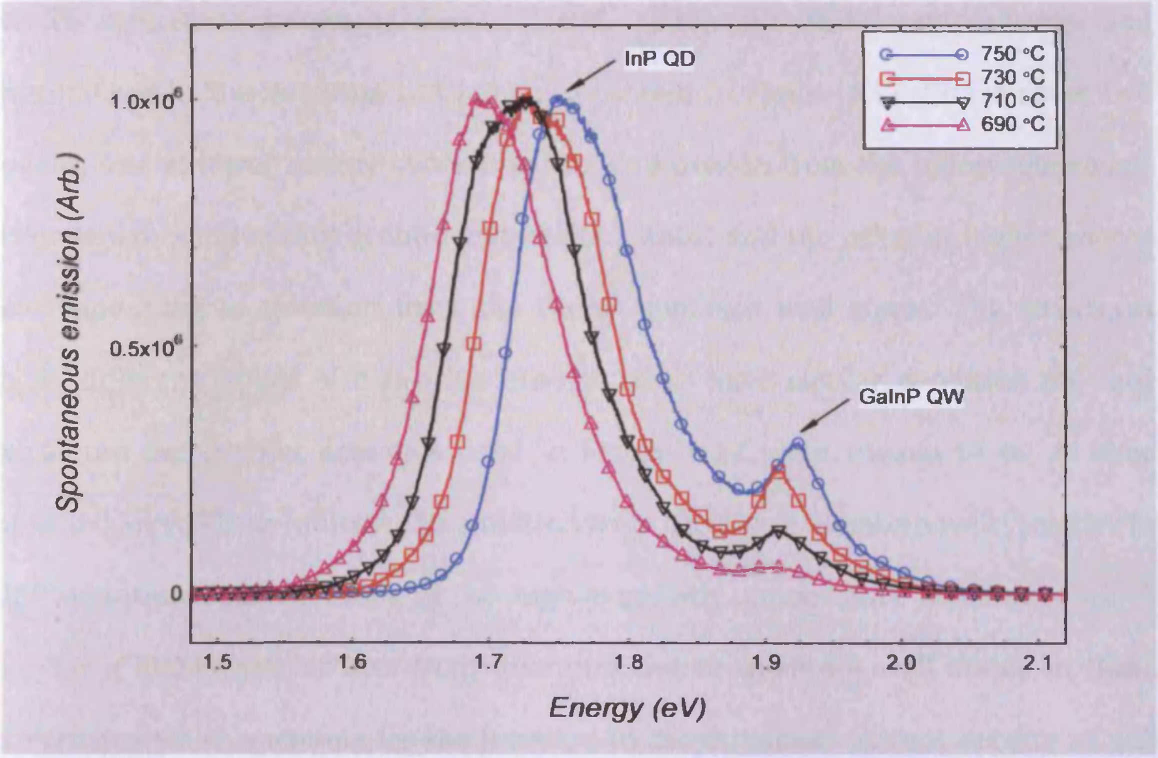

Figure 4.12 *Spontaneous emission spectra for structures with 8nm barrier width taken at the same difference between quasi- Fermi level separation and absorption edge. The symbols marked on each curve are a guide to the eye.*

taken, are selected at values leading to certain condition which will be applied to the compared structures. The structures have different values of transition energy, so to maintain a similar pumping for each structure the current densities used in these structures were chosen to give the same difference between quasi-Fermi level separation (transparency point on the gain spectra) and the absorption edge ($\Delta E_f - AE$) as shown in Figure 4.11.

4.6.2 Spontaneous Emission in Narrow Barriers

The spontaneous emission spectra taken through a top-contact window of the laser devices with injected current densities at room temperature for $8nm$ barrier width structures grown at 690°C, 710°C, 730°C and 750°C temperatures and normalised at the quantum dot peak are plotted in Figure 4.12. These show two peaks, one at lower energy corresponding to emission from the inhomogeneously broadened quantum dot ground and excited states and the other at higher energy corresponding to emission from the GaInP quantum well states. The structures have different values of transition energy, so to have similar condition for each structure the current densities used in Figure 4.12 were chosen to be at same injected level. These indicate the emission from the GaInP quantum wells relative to InP quantum dots increases in the higher growth temperature structures which means a higher carrier loss from quantum dot to quantum well states in these structures which accounts for the increase in the threshold current density as will be explained in detail later in this chapter.

4.6.3 Spontaneous Emission in Wide Barriers

The spontaneous emission spectra taken through a top-contact window of the

Barrier width	Growth Temperature	A_{QW}/A_{tot}
8nm	690°C	0.0308
8nm	710°C	0.0677
8nm	730°C	0.1223
8nm	750°C	0.1500
16nm	710°C	0.1297
16nm	730°C	0.1925
16nm	750°C	0.2768

Table 4.4 *The ratio of the area of the spectrum corresponding to quantum well emission to total area under spontaneous emission spectra.*

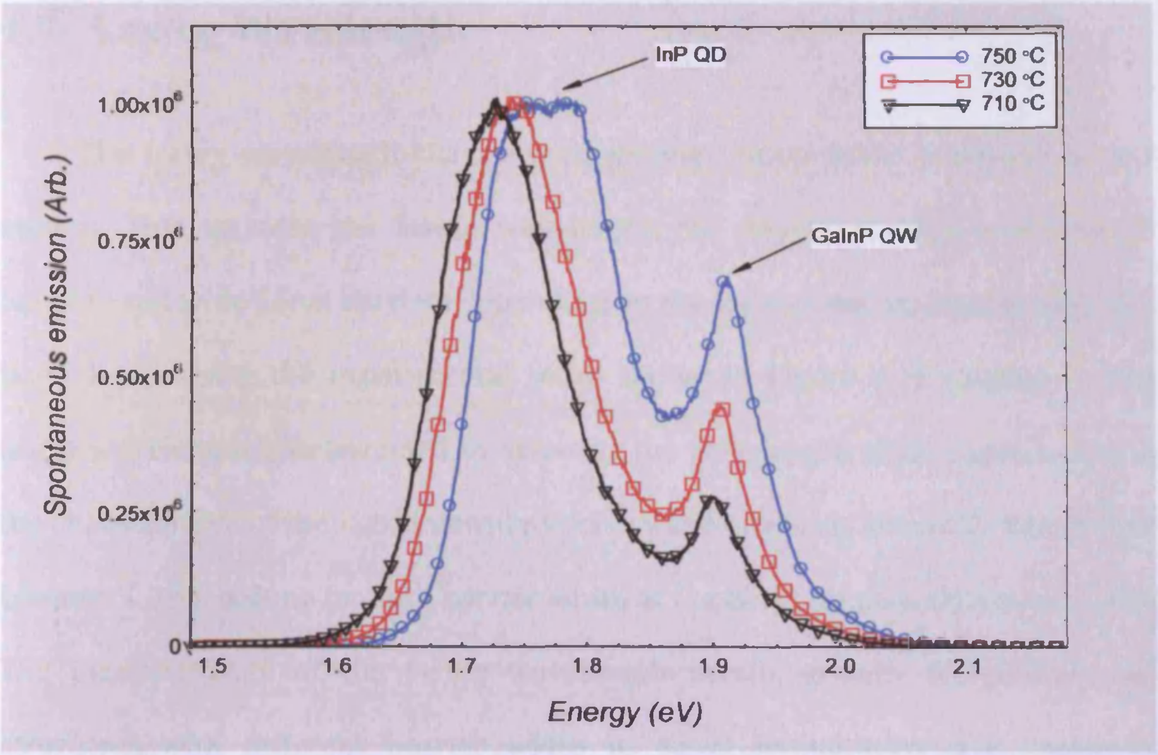

Figure 4.13 *Spontaneous emission spectra for structures with 16nm barrier width taken at the same difference between quasi- Fermi level separation and absorption edge. The symbols marked on each curve are a guide to the eye.*

laser devices with injected current densities just below threshold for 16*nm* barrier width structures grown at 710°C, 730°C and 750°C temperatures and normalised at the quantum dot peaks are plotted in Figure 4.13. These show similar trends to that in 8*nm* barrier width structures where the emission from the GaInP quantum wells relative to InP quantum dots increases in the higher growth temperature structures. The values for the ratio of the area of the spectrum at energies corresponding to the GaInP quantum well emission to the total area A_{QW}/A_{tot} for all studied structures are listed in Table 4.4. This ratio can be calculated by drawing a vertical line from the minimum value between the two peaks then evaluate the area under the quantum well peak starting from that vertical line.

4.7 Lasing Wavelength

The lasing wavelength change with growth temperature is studied in this section. This includes the lasing wavelength for structures with narrow 8*nm* barriers and wide 16*nm* barriers depending on the measurements emitted from the laser device using the experimental setup shown in Figure 3.18 Chapter 3. The lasing wavelength is determined by selecting the wavelength of the highest peak in the characteristic of the light intensity versus wavelength, as shown in Figure 3.19 Chapter 3. This is done for each barrier width at the different growth temperatures. The measurements of the lasing wavelength versus growth temperature for structures with different barrier width at room temperature are shown in

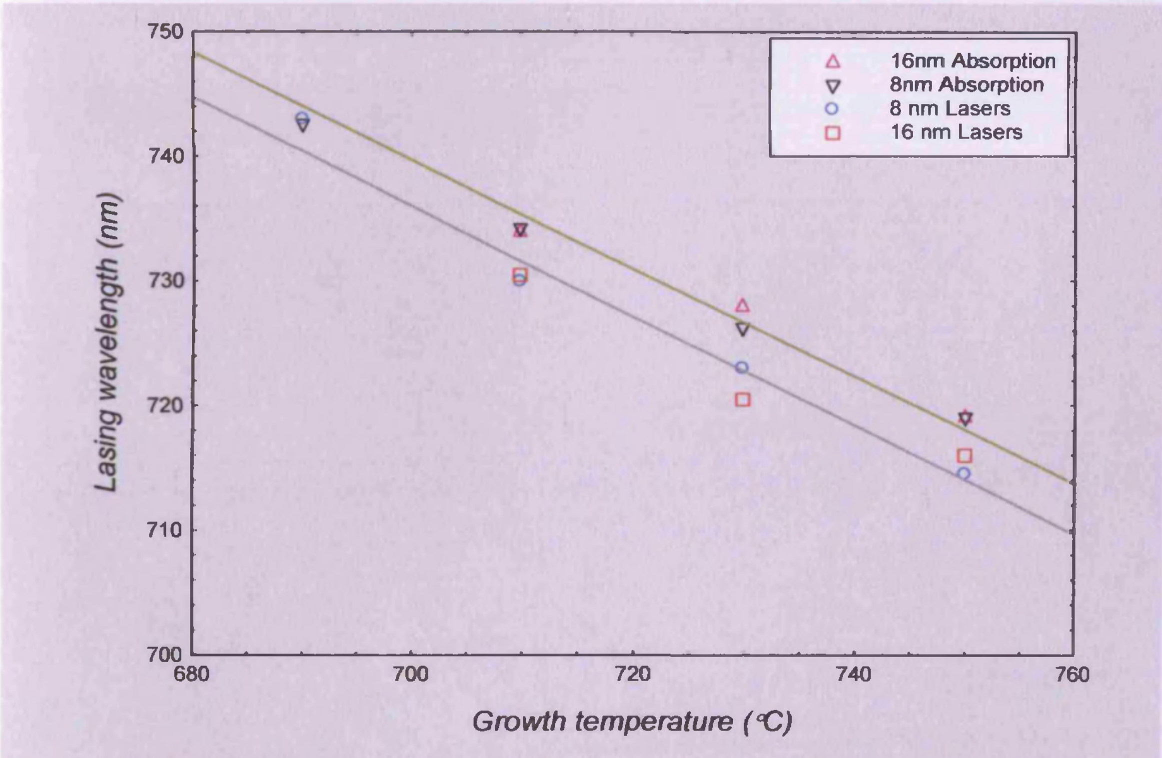

Figure 4.14 *Absorption edges and lasing wavelengths versus growth temperatures for structures with cavity length of 2mm long and different barrier width at room temperature.*

Figure 4.14. These are consistent with the measurements of the absorption edges obtained from the optical absorption spectra shown in Figures 4.5 and 4.6 of the same structures. These indicate a linear decrease to the lasing wavelength values as the growth temperature increases. The effect of the growth temperature on the dots size and height leads to different energy level positions which account for the change in lasing wavelength. This agrees with the energy shift in the absorption, gain and spontaneous emission spectra. The lasing wavelength range of $715nm$ - $745nm$ is obtained by changing the growth temperature between $690^{\circ}C$ - $750^{\circ}C$ and it is independent of the change in barrier width as seen in Figure 4.14. This covers a wavelength range from the required wavelength range mentioned in the motivations in Chapter 1.

4.8 Barrier Width and Growth Temperature

The effect of barrier width and growth temperature on optoelectronic properties is studied in this section. These properties include threshold current density, optical absorption and spontaneous emission for structures with narrow 8*nm* and wide 16*nm* barriers each grown at different temperatures depending on the measurements obtained from both laser and multisection devices which have been shown in the previous sections.

4.8.1 Barrier Width Effect

The threshold current density for different barrier widths grown at different

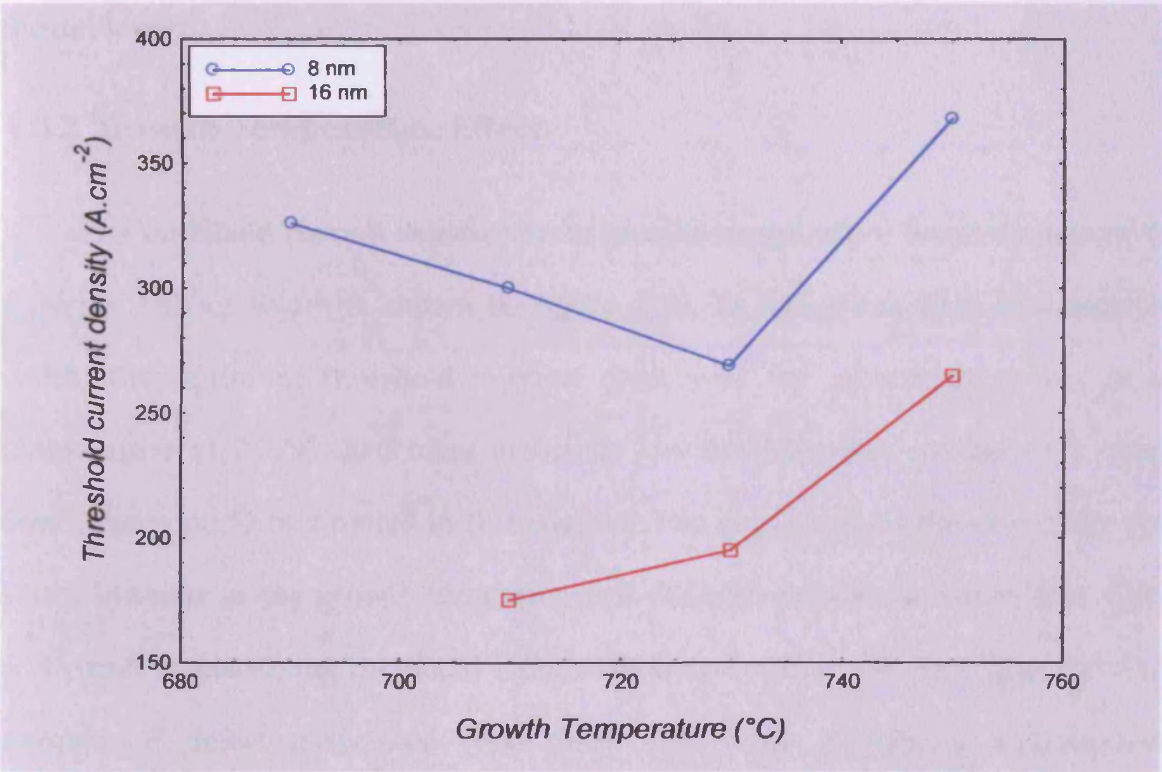

Figure 4.15 *Threshold current density versus growth temperature for structures with different barrier widths at room temperature.*

temperatures is shown in Figure 4.15. The threshold current density points are taken from Figure 4.3 for structures with 8*nm* barrier width at room temperature and from Figure 4.4 for structure with 16*nm* barrier width at room temperature. The threshold current density for structures with 16*nm* barrier width is lower than that with 8*nm* barrier width as shown in Figure 4.15. Previous results shows that the increase of the spacer layers between the dots layer reduce the threshold current density for InAs quantum dots [3]. In structures with 16*nm* barrier width there is more barrier material, which smooths out the surface of the barrier. This will reduce the effect on the next dot layers which mean one layer of dots has less effect on the growth of subsequent layers of dots and this will reduce the inhomogeneous broadening of the quantum dots as shown in Figure 4.16. Same explanation was used in InAs quantum dot when they have high spacers between the dot layers.

4.8.2 Growth Temperature Effect

The threshold current density versus growth temperature for structures with different barrier width is shown in Figure 4.15. In structures with 8*nm* barrier width, the optimum threshold current density is for structures grown at a temperature of 730°*C*. Structures grown at low temperatures contain very large dots as previously mentioned in this chapter. The magnitude of the very large dot states increase as the growth temperature is reduced as seen in Figure 4.16. This will result in increasing threshold current density because the very large dot has number of defect associated with them and these provide a nonradiative recombination to the structure as suggested previously [4] in InP/GaInP quantum

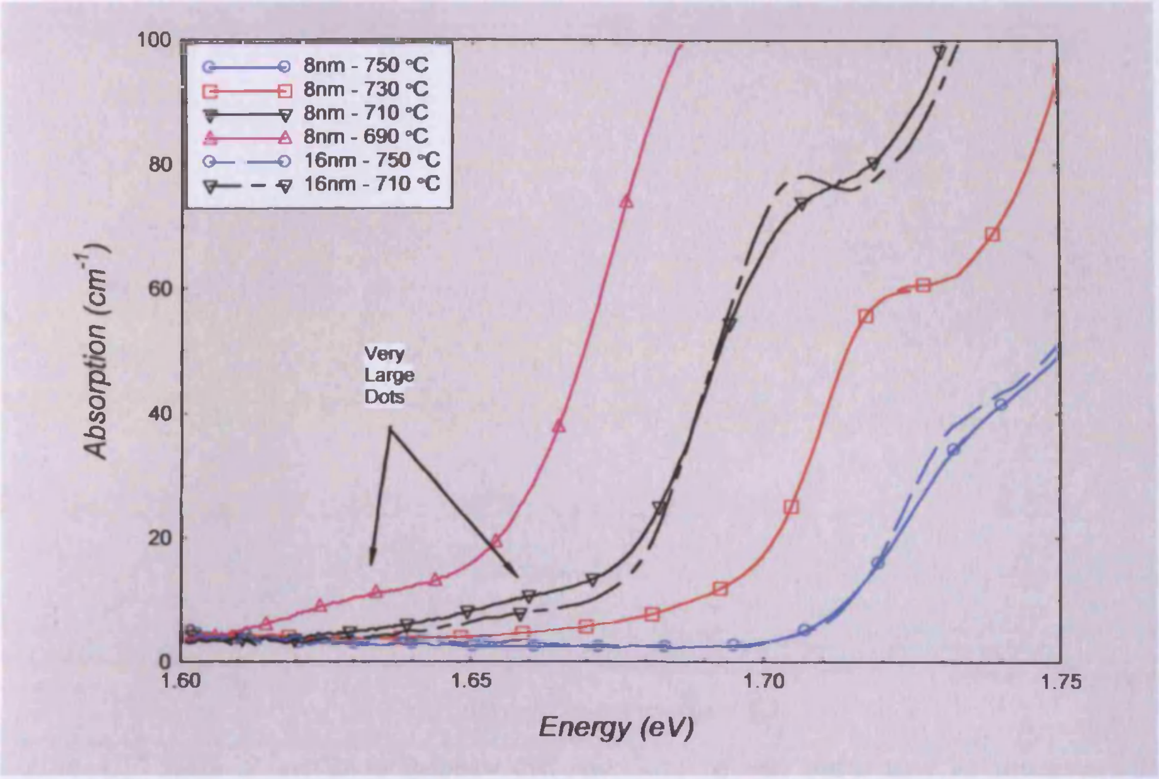

Figure 4.16 *Modal absorption versus photon energy shows the very large dots for structures with different barrier width. The symbols marked on each curve are a guide to the eye.*

dot. However, in structures with 16*nm* barrier width, there is more barrier material which smooths out the surface of the barrier as mentioned previously, and therefore the effect of the very large dot is smaller because their number has been reduced as barrier surface is plane in all dot layers. As a result of this, the very large dots cause the increase in the threshold current density more in structures with 8*nm* barriers than structures with 16*nm* barriers, especially in structures grown at low temperatures as shown in Figure 4.16. The structures which are grown at temperature of 710°*C* in Figure 4.16 show an obvious difference in the very large dot between these structures which result in high difference in their threshold current densities magnitude as compare to structures grown at high temperatures such as 750°*C*.

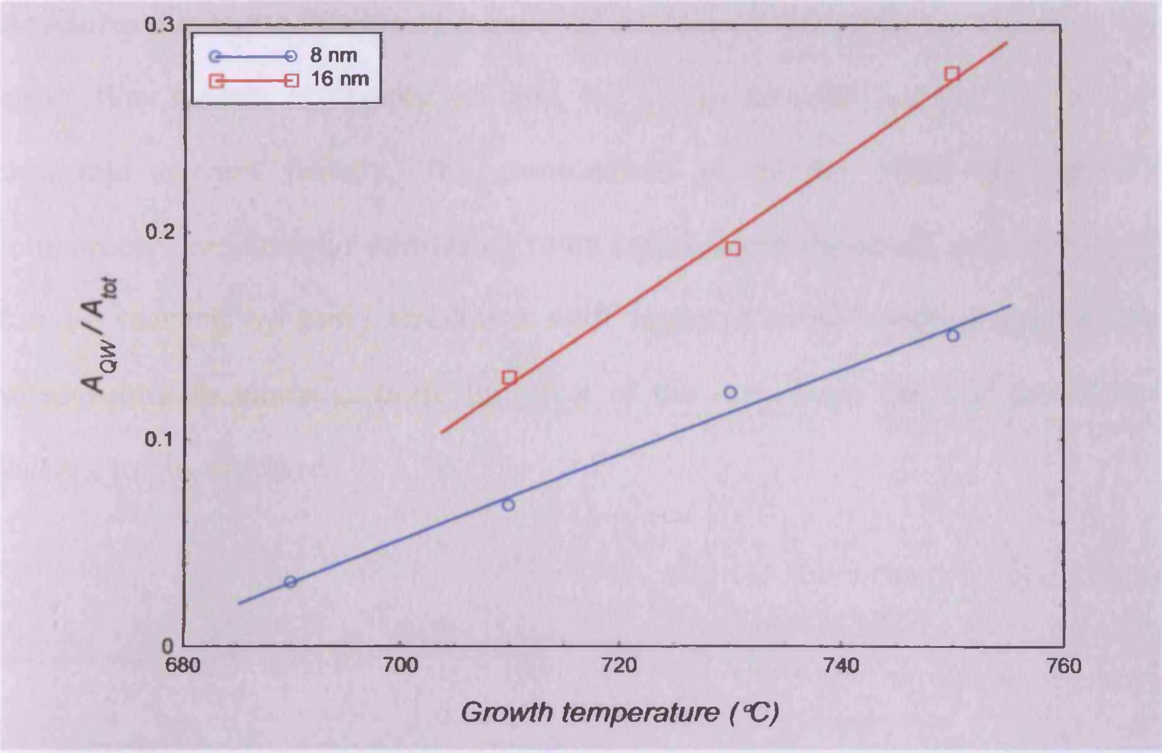

Figure 4.17 *Ratio of area under quantum well peak versus growth temperature for structures with different barrier width at room temperature.*

The ratio of area of the spectrum at energies corresponding to the GaInP quantum well states to the total area A_{QW}/A_{tot} versus growth temperature for structures with different barrier width grown at different growth temperatures is plotted in Figure 4.17. These are taken for spontaneous emission spectra shown in Figures 4.12 and 4.13 with injected current densities just below threshold at the same difference between quasi-Fermi level separation and the absorption edge for structures with 8*nm* and 16*nm* barrier width respectively. These curves shown in Figure 4.17 indicate the emission from the GaInP quantum wells relative to InP quantum dots increases in the higher growth temperature structures which means a higher carrier leakage from quantum dot to quantum well states in these structures due to the decreasing number of states available for lasing as seen in the absorption spectra of Figures 4.5 and 4.6, which accounts for the increase in threshold current density. The combination of barrier width and growth temperature required for optimising room temperature threshold current density can be reached by using structures with higher barrier width grown at low temperature to minimise both the affect of the very large dot and the carrier leakage in the structure.

4.9 Summary

In this chapter the data taken from several experiments were presented and interpreted using seven structures, which vary in both the barrier width and growth temperature, to study the effect of barrier width and growth temperature on optoelectronic properties of InP/AlGaInP quantum dot laser diodes.

The chapter began by introducing the device structures used in this chapter. The threshold current density around room temperature were evaluated including these in narrow and wide barrier widths using laser devices. The chapter described the optical absorption and gain spectra using the amplified spontaneous emission emitted from multisection devices. This explains the behaviour of the threshold current density in structures grown at low temperatures and verifies the threshold current density values by comparing the gain-current relations obtained from both the laser and multisection devices. Afterwards, the spontaneous emission spectra taken for all structures at the same pumping, which obtained from the gain spectra, were studied and this presents the carrier loss in the system which explains the increase of threshold current density for structures grown at high temperatures. The chapter evaluated the lasing wavelength for the studied structures. Finally, the chapter ended with studying the effect of both barrier width and growth temperature on InP/AlGaInP quantum dot laser diodes using the data presented in the chapter by different experiments.

References

[1] W. Seifert, N. Carlsson, J. Johansson, M-E. Pistol, L. Samuelson, *"In situ growth of nano-structures by metal-organic vapour phase epitaxy"*, Journal of Crystal Growth, 170, pp. 39-46 (1997).

[2] J. Porsche, A. Ruf, M. Geiger, F. Scholz, *"Size Control of self assembled InP/GaInP quantum islands"*, Journal of Crystal Growth, 195, pp. 591- 595 (1998).

[3] C. L. Walker, I. C. Sandall, P. M. Smowton, I. R. Sellers, D. J. Mowbray, H. Y. Liu, M. Hopkinson, *"The Role of High Growth Temperature GaAs Spacer Layers in 1.3μm In(Ga)As Quantum Dot Lasers "*, IEEE Photonics Technology Letters, 17, 10, p.2011 (2005).

[4] P. M. Smowton, J. Lutti, G. M. Lewis, A. B. Krysa, J. S. Roberts, P. A. Houston, *"InP-GaInP quantum-dot lasers emitting between 690-750nm"*, IEEE Journal of Selected Topics in Quantum Electronics, 11, 5 pp.1035- 1040 (2005).

CHAPTER 5

Carrier Distribution at Low Temperatures

5.1 Introduction

In this chapter the carrier distribution at low temperatures taken from several experiments is interpreted using four structures, which vary in the growth temperature, to study the carrier distribution in InP/AlGaInP quantum dot laser diodes.

The chapter begins by introducing the device structures used. The threshold current density at low temperature is evaluated using laser devices. The chapter studies the optical absorption and gain spectra for a certain gain value at low temperatures using the amplified spontaneous emission emitted from multisection devices. This presents the energy shift with temperature and also presents the quasi-Fermi level separation in the low temperature range. Afterwards, the chapter studies the spontaneous emission spectra at low temperatures taken for two of the structures and this presents both the carrier distribution in quantum dot states and the carrier loss in the system. Both explain the increase of threshold current density at either low or high temperatures. The chapter then evaluates the lasing wavelength at low temperatures for the studied structures. Finally, the chapter ends with a study of the carrier distribution in different growth temperature structures of InP/AlGaInP quantum dot laser diodes at low temperatures using the data presented in the chapter by different experiments.

5.2 Device Structures

The device structures used in this chapter to study the effect of growth temperature on carrier distribution are described in this section. The device structures detail are illustrated in Figure 3.7 Chapter 3 and listed in Table 3.5 Chapter 3. The bandgap energy diagram versus growth distance for these structures is shown in Figure 3.8 Chapter 3. There are four structures used and they are similar but vary in the temperature at which the waveguide core is grown. In this chapter, the comparison of different structures at low temperatures were grown with dot and other waveguide core layers at different temperatures of 690°*C*, 710°*C*, 730°*C* and 750°*C* is studied. Each of these dot layers was formed from 2 monolayers of InP grown on $(Al_{0.3}Ga_{0.7})_{0.51}In_{0.49}P$ and covered by 8*nm* $Ga_{0.51}In_{0.49}P$ quantum well layers.

The device structures were processed into multisection devices to measure the amplified spontaneous emission and also oxide isolated stripe lasers with top windows to measure the threshold current density as well as spontaneous emission as was described in Chapter 3.

5.3 Threshold Current Density

In this section the threshold current density at low temperatures is studied. The section starts by describing the light-current characteristics in the low temperature range from which the threshold currents are determined. These are used to calculate the threshold current densities at low temperatures for structures grown at different temperatures.

5.3.1 Threshold Current at Low Temperatures

The light-current characteristics have been investigated using the current voltage light temperature I-V-L-T measurement experiment, which is described in

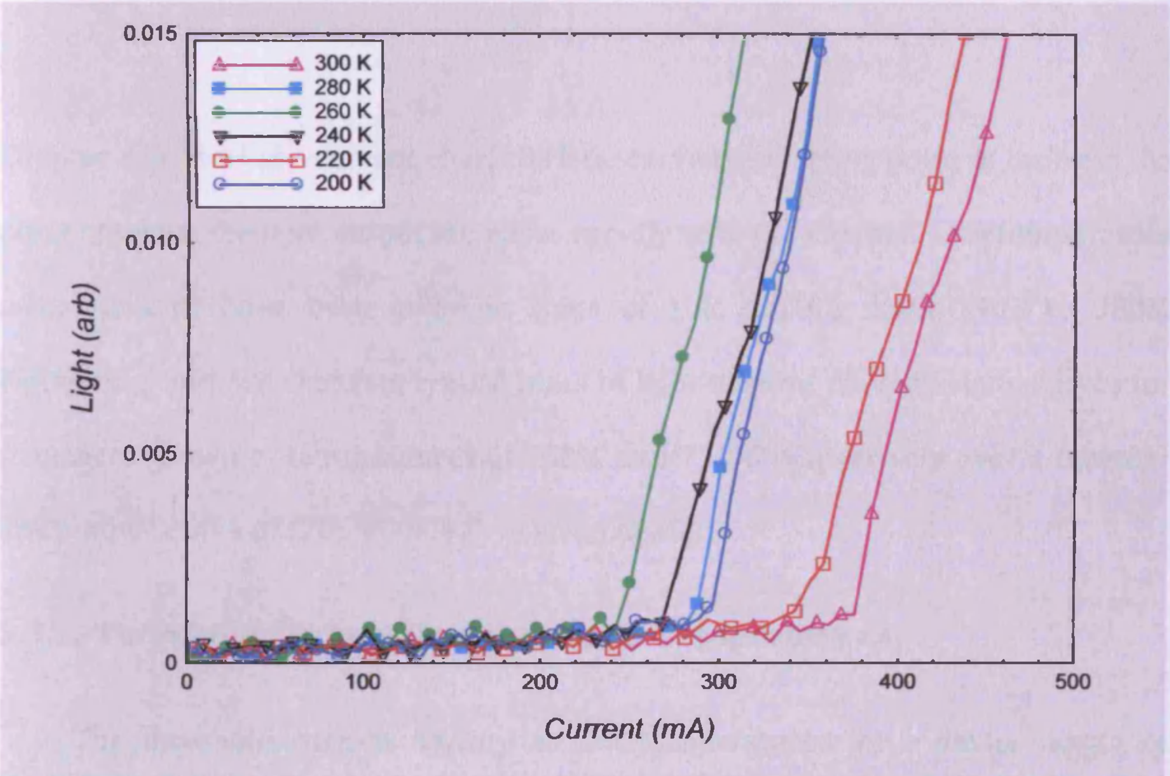

Figure 5.1 *Light-current characteristic curves for structure grown at 750°C. The symbols marked on each curve are a guide to the eye.*

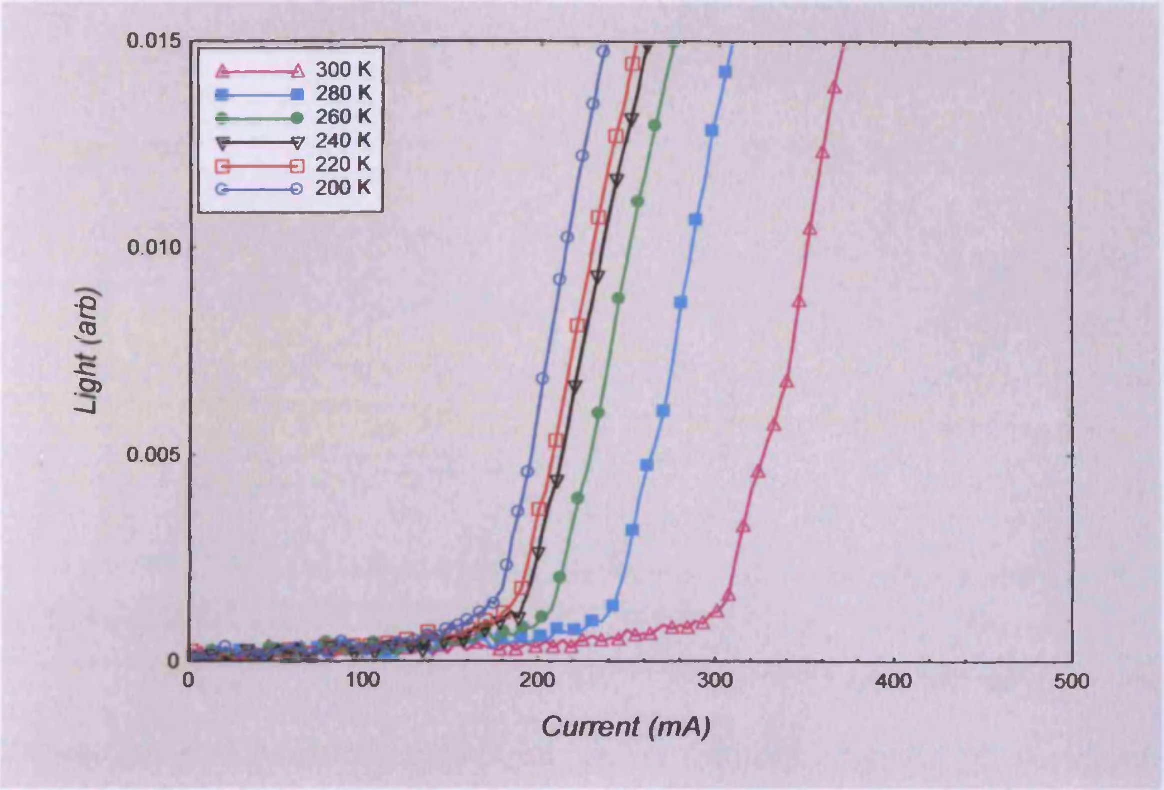

Figure 5.2 *Light-current characteristic curves for structure grown at 710°C. The symbols marked on each curve are a guide to the eye.*

Chapter 3. In the light-current characteristic curve the starting point of lasing is the point at which the light output increases rapidly with the current. Low temperature measurements have been taken in steps of $10K$ starting from $190K$ to $300K$. Figures 5.1 and 5.2 illustrate typical plots of light-current characteristic curves for structures grown at temperatures of $750^{\circ}C$ and $710^{\circ}C$ respectively over a range of low temperatures of $(200K - 300K)$ in steps of $20K$.

5.3.2 Threshold Current Density at Low Temperatures

The threshold current density at low temperatures for a device length of $2000\mu m$ has been obtained for structures grown at temperatures of $690^{\circ}C$, $710^{\circ}C$,

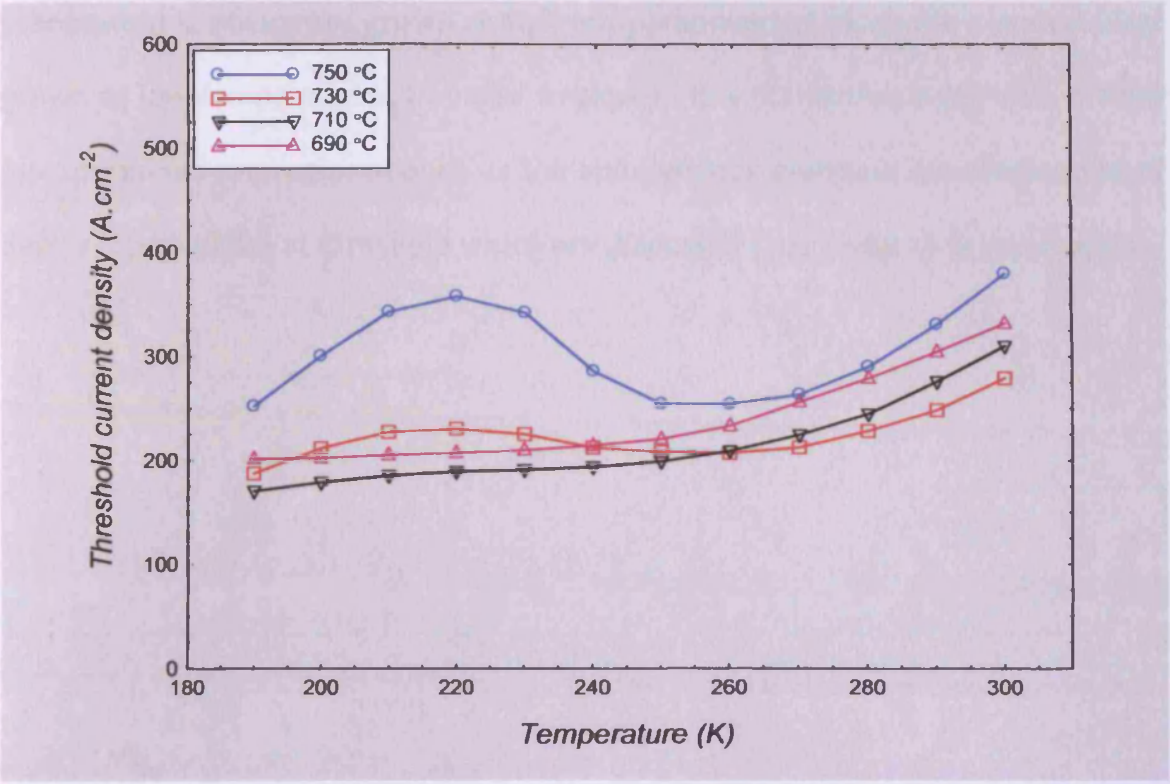

Figure 5.3 *Threshold current density at low temperatures for structures grown at different growth temperatures.*

730°C and 750°C from the light-current characteristic curves. The plot of the threshold current density at low temperatures for structures grown at different temperatures and with cavity length of 2000μm is shown in Figure 5.3. This figure shows the threshold current density increases superlinearly at higher temperatures above 260K which is often observed in quantum dot systems. At low temperatures, the threshold current density exhibits a distinctive dependence on the operating temperature, where from 190K, it initially increases with temperature until it reaches a local maximum at 220K, then it decreases with increasing temperature until a minimum is reached at 260K. This has previously been observed for p-doped InAs/GaAs quantum dot lasers [1]. This type of behaviour became more pronounced in structures grown at high temperatures but disappears in structures grown at low temperatures. In order to explain this distinctive behaviour, further measurements are required such as the spontaneous emission spectra from laser device top windows at threshold which are discussed later in detail in this chapter.

5.4 Optical Gain and Absorption Spectra

The optical gain and absorption spectra at low temperatures are studied in this section. This includes the optical gain and absorption spectra for structures grown at a high temperature of $750°C$ and low temperature of $710°C$ obtained from the multisection device measurements using Equation 3.9 Chapter 3. Measurements of the gain spectrum at low temperatures with the same value of peak gain are compared.

5.4.1 Selection of Gain Values

In order to compare spontaneous emission spectra of the same structure at different temperatures, the injected current densities, at which these spontaneous emissions were taken, are selected at threshold using laser devices with cavity length about $2mm$ long. The equivalent value at which the gain spectrum is taken using the multisection device is $6cm^{-1}$ at any temperature because this is the value of the optical losses of a 2mm long laser.

5.4.2 Temperature Variation in High Growth Temperature

The gain and absorption spectra at low temperatures for structure grown at temperature of $750°C$ are shown in Figure 5.4. Each of the gain spectra is taken at peak value of $6cm^{-1}$ and gives single values for both the injected levels and the injected currents at a given temperature. The injected level is defined as the difference between quasi-Fermi level separation (transparency point on the gain spectra) and the absorption edge ($\Delta E_f - AE$) as shown in Figure 4.10 Chapter 4

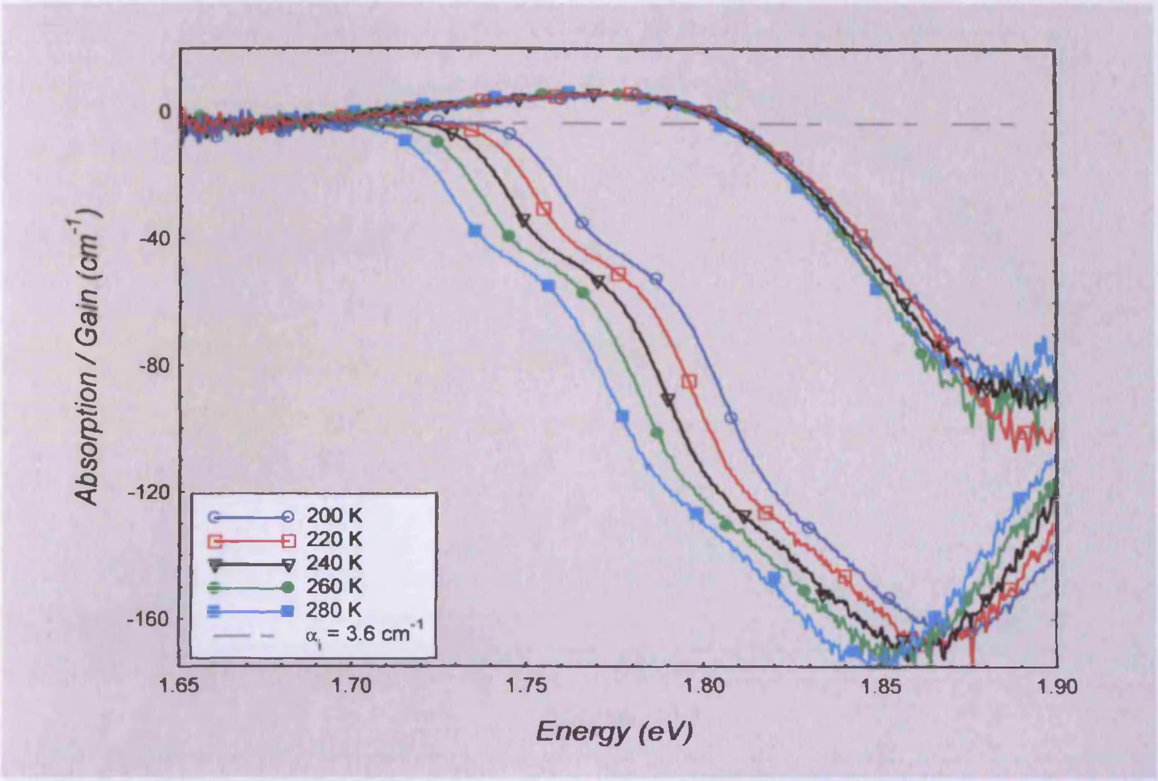

Figure 5.4 *Gain-absorption spectra at different low measurement temperatures with fixed peak gain at $6cm^{-1}$ for structure grown at 750°C. The symbols marked on each curve are a guide to the eye.*

whereas the injected current is the operating current which is applied to the multisection device to reach a gain value equal to $6cm^{-1}$. These two significant quantities along with the shift in the spectra because of temperature change are studied later in detail in this chapter at low temperatures in order to understand the distinctive behaviour of the threshold current density in the $750^{\circ}C$ growth temperature structure.

5.4.3 Temperature Variation in Low Growth Temperature

Similar plots for a structure grown at $710^{\circ}C$ are shown in Figure 5.5. These two significant quantities along with the shift in the spectra are studied later in

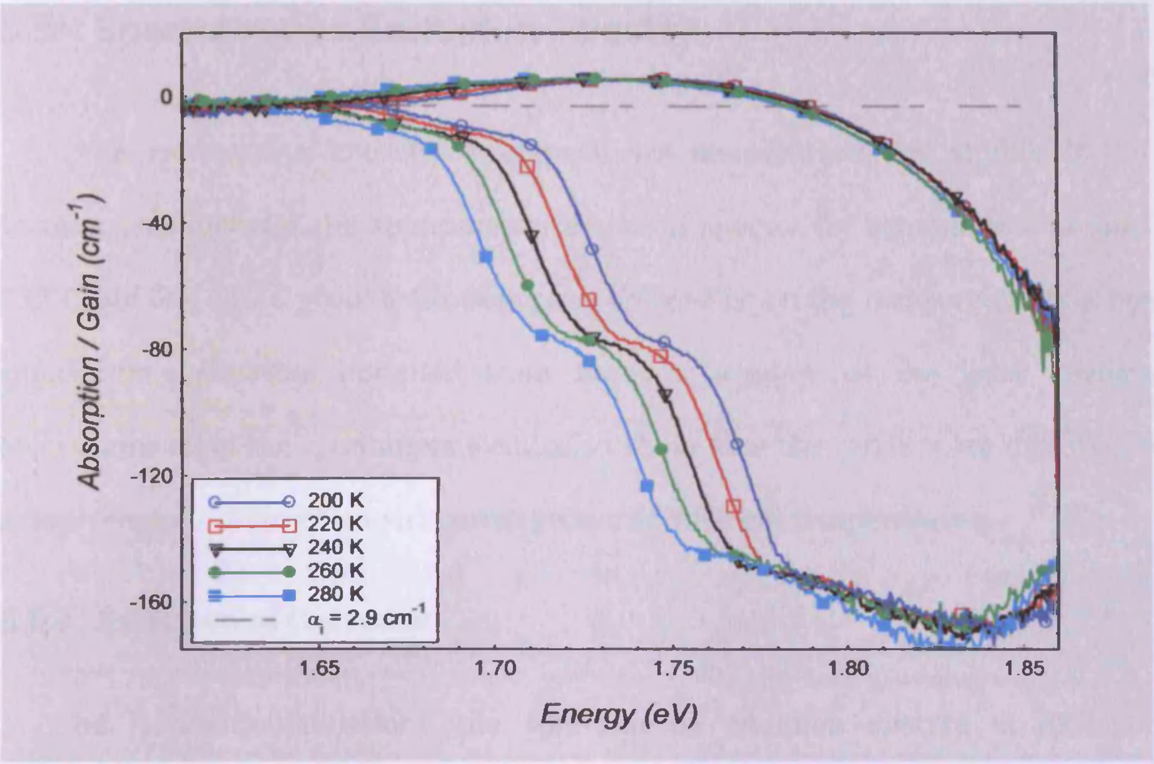

Figure 5.5 *Gain-absorption spectra at different low measurement temperatures with fixed gain at 6cm^{-1} for structure grown at 710°C. The symbols marked on each curve are a guide to the eye.*

detail in this chapter at low temperatures in order to compare between the behaviours of the threshold current density in the 750°C and 710°C growth temperature structures.

5.5 Spontaneous Emission Spectra

The spontaneous emission spectra at low temperatures are studied in this section. This includes the spontaneous emission spectra for structures with high $750^{\circ}C$ and low $710^{\circ}C$ growth temperatures depending on the measurements of the spontaneous emission obtained from the top window of the laser devices. Measurements of the spontaneous emission show how the carriers are distributed at low temperatures within structures grown at different temperatures.

5.5.1 Selection of Currents

As is mentioned before, the spontaneous emission spectra at different temperatures with a given structure are selected at threshold. This will maintain the same condition applied to the structure at any temperature.

5.5.2 Spontaneous Emission in High Growth Temperature

The spontaneous emission spectra taken through a top-contact window of the laser devices with injected current densities at low temperatures for structure grown at $750^{\circ}C$ temperature are plotted in Figure 5.6. These are vertically offset for clarity and normalised to the quantum dot peak. It show two peaks, one at lower energy corresponding to emission from the inhomogeneously broadened InP quantum dots ground and excited states and the other at higher energy corresponding to emission from the GaInP quantum well states. This indicates that as the temperature is increased from $200K$, the InP quantum dot peak initially narrows and the emission from the GaInP quantum well begins to increase. As the

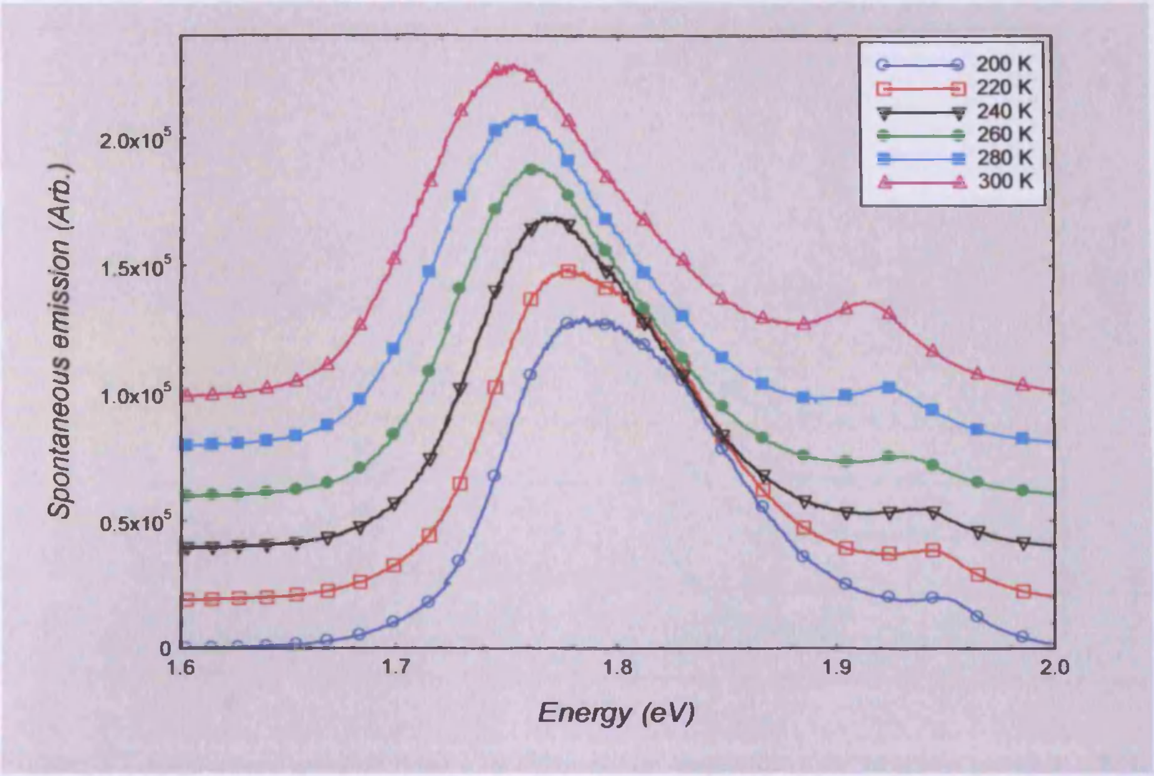

Figure 5.6 *Spontaneous emission spectra at different low temperatures for structure grown at 710°C. The symbols marked on each curve are a guide to the eye.*

temperature is further increased, the InP dot peak width increase again and the magnitude of emission from the GaInP quantum well increases further.

5.5.3 Spontaneous Emission in Low Growth Temperature

Similar plots for a structure grown at $710°C$ are shown in Figure 5.7 and also show two peaks, corresponding to emission from InP quantum dots ground and excited states and from the GaInP quantum well states. This indicates that both the InP quantum dot peak width and the emission from the GaInP quantum well increases with the temperature starting from $200K$.

The broadening in the InP quantum dots peak and the amount of emission

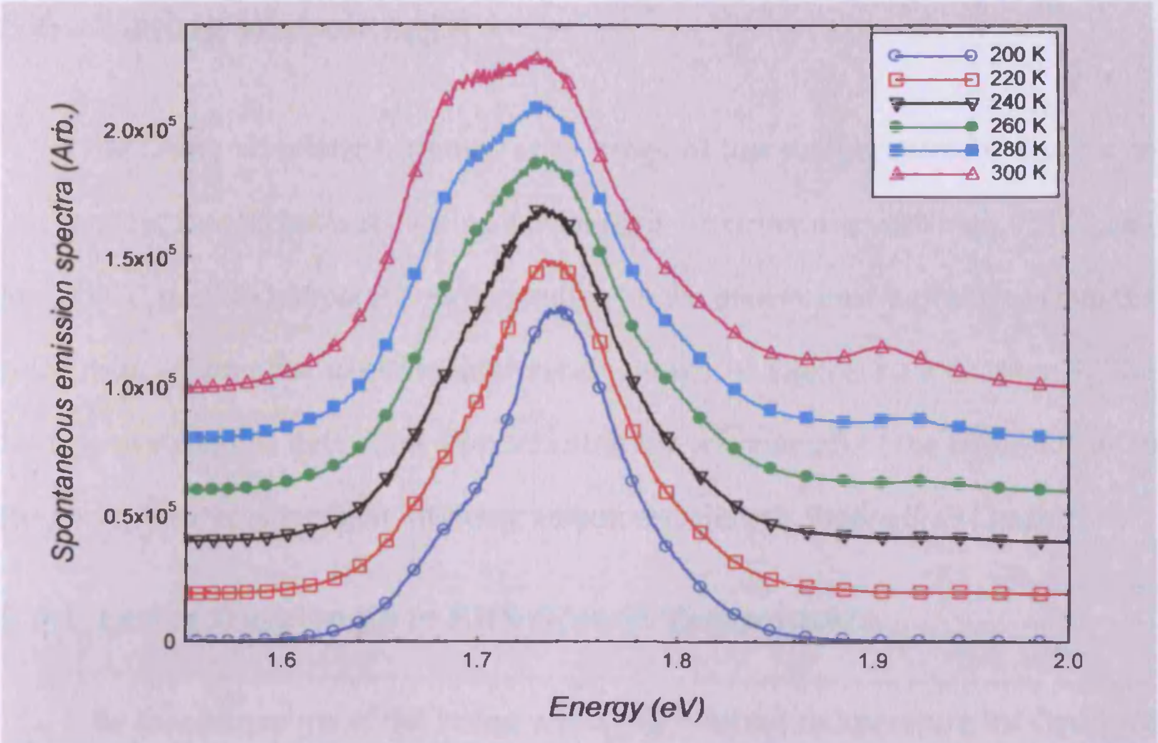

Figure 5.7 *Spontaneous emission spectra at different low temperatures for structure grown at 750°C. The symbols marked on each curve are a guide to the eye.*

from the GaInP quantum well peak are represented by the full width half maximum (FWHM) of the quantum dots peak and the ratio of the area of the spectrum at energies corresponding to the GaInP quantum well states to the total area A_{QW}/A_{tot} respectively. These parameters are proportional to the carrier distribution in the quantum dots states and the carrier loss from quantum dot to the quantum well states. This is discussed in detail later in this chapter.

5.6 Lasing Wavelength

The lasing wavelength change with range of low temperatures is studied in this section. This includes the lasing wavelength for structures with high, 750°*C*, and low, 710°*C*, growth temperatures depending on the measurements emitted from the laser device using the experimental setup shown in Figure 3.18 Chapter 3. The lasing wavelength is determined by selecting the wavelength of the highest peak in the characteristic of the light intensity versus wavelength, Figure 3.19 Chapter 3.

5.6.1 Lasing Wavelength in High Growth Temperature

The measurements of the lasing wavelength versus temperature for structure grown at temperature of 750°*C* are shown in Figure 5.8. These indicate a linear

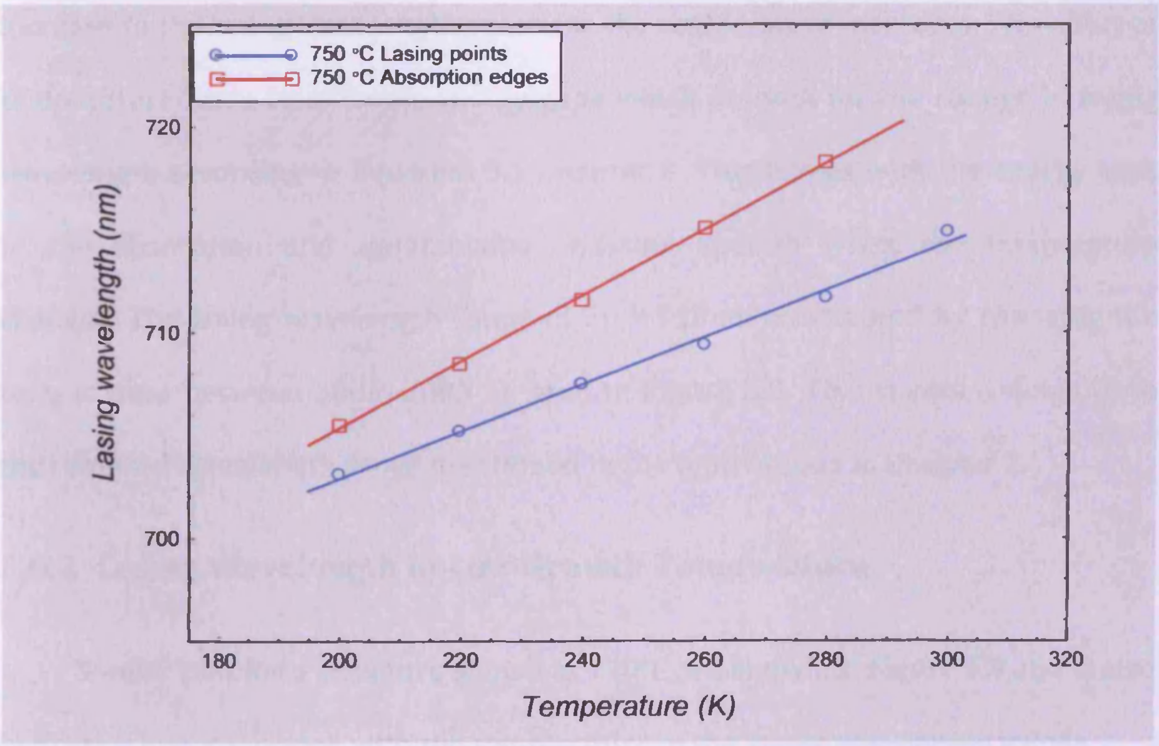

Figure 5.8 *Lasing points and absorption edges versus temperature for structure grown at 750°C.*

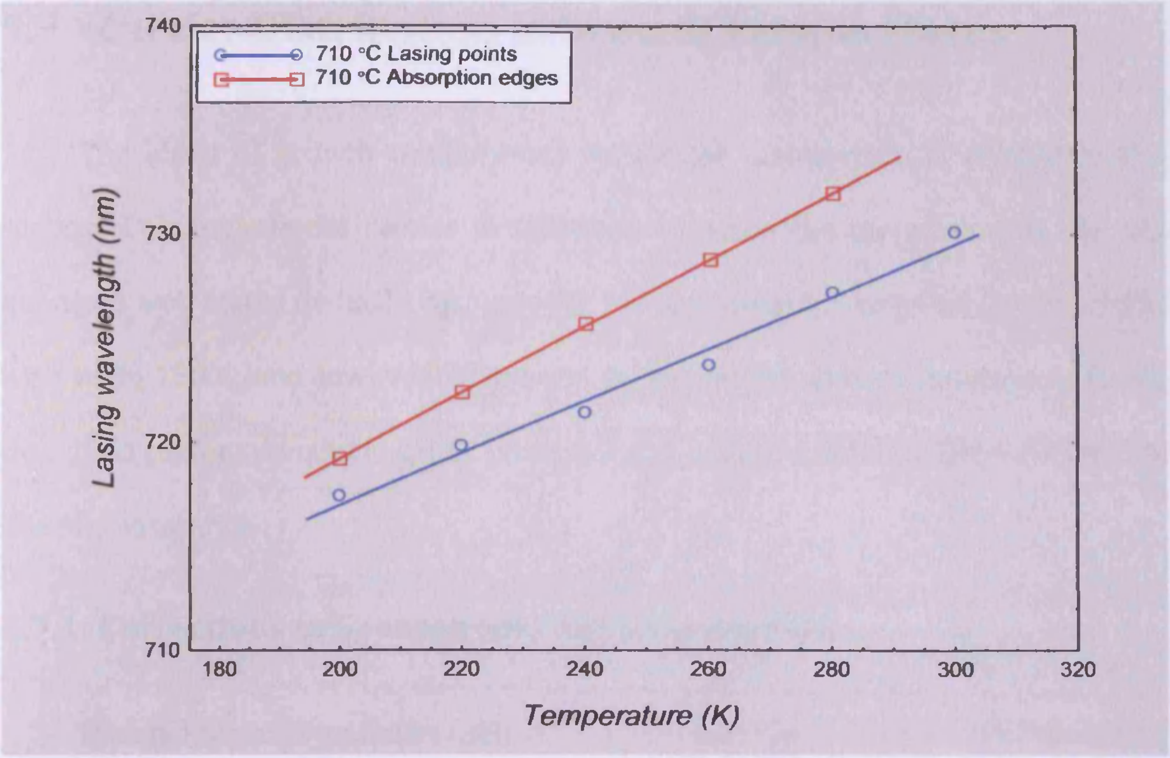

Figure 5.9 *Lasing points and absorption edges versus temperature for structure grown at 710°C.*

increase to the lasing wavelength values as the temperature increases. The effect of temperature leads to different energy gaps which account for the change in lasing wavelength according to Equation 3.1 Chapter 3. This agrees with the energy shift in the absorption and spontaneous emission spectra when the temperature changes. The lasing wavelength range of 703–715nm is obtained by changing the temperature between 200K–300K as seen in Figure 5.8. This covers a range from the required wavelength range mentioned in the motivations in Chapter 1.

5.6.2 Lasing Wavelength in Low Growth Temperature

Similar plot for a structure grown at 710°C are shown in Figure 5.9 and it also indicate a linear increase with the temperature to the lasing wavelength values.

5.7 Carrier Distribution in Growth Temperatures

The effect of growth temperature on carrier distribution is studied in this section. This include the carrier distribution between the quantum dots and the quantum well states deduced by studying the spontaneous emission for structures with high, 750°C, and low, 710°C, growth temperatures and comparison with the threshold current density in order to explain the origin of it distinctive behaviour at low temperatures.

5.7.1 Corrections to Spontaneous Emission Spectra

The spontaneous emission spectra shown in Figures 5.6 and 5.7 are normalised

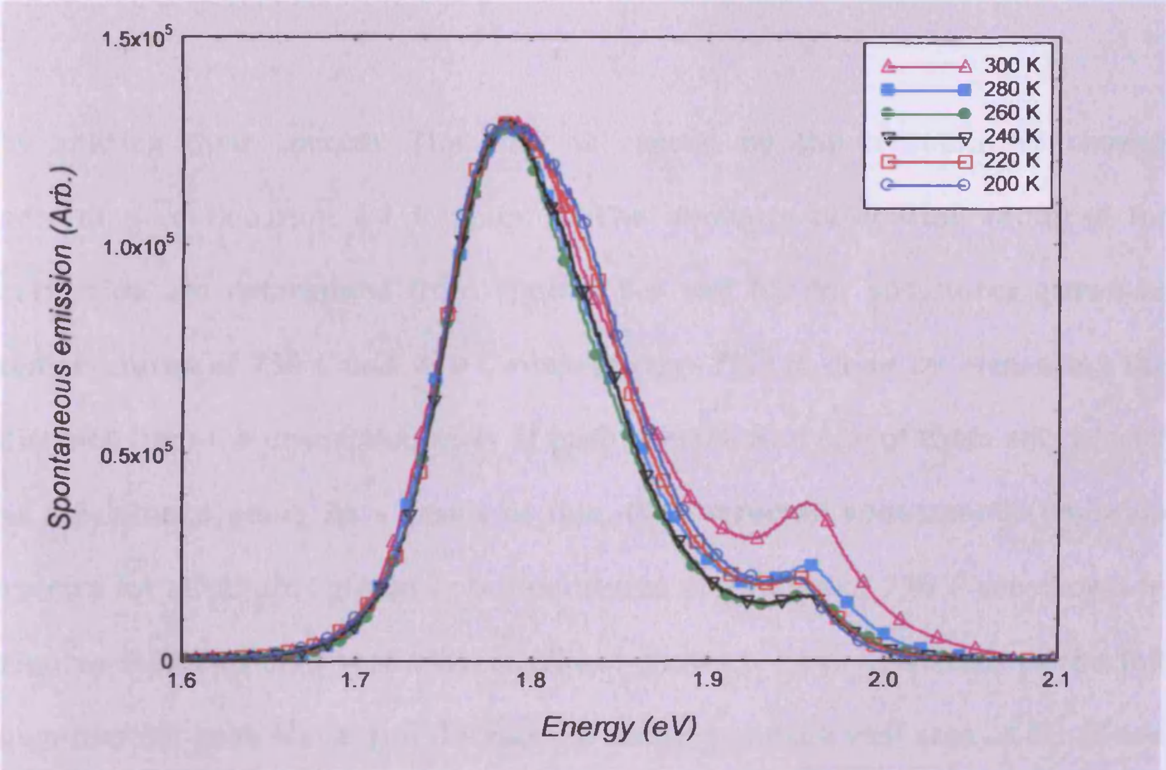

Figure 5.10 *Normalised spontaneous emission spectra for structure grown at 750°C. The symbols marked on each curve are a guide to the eye.*

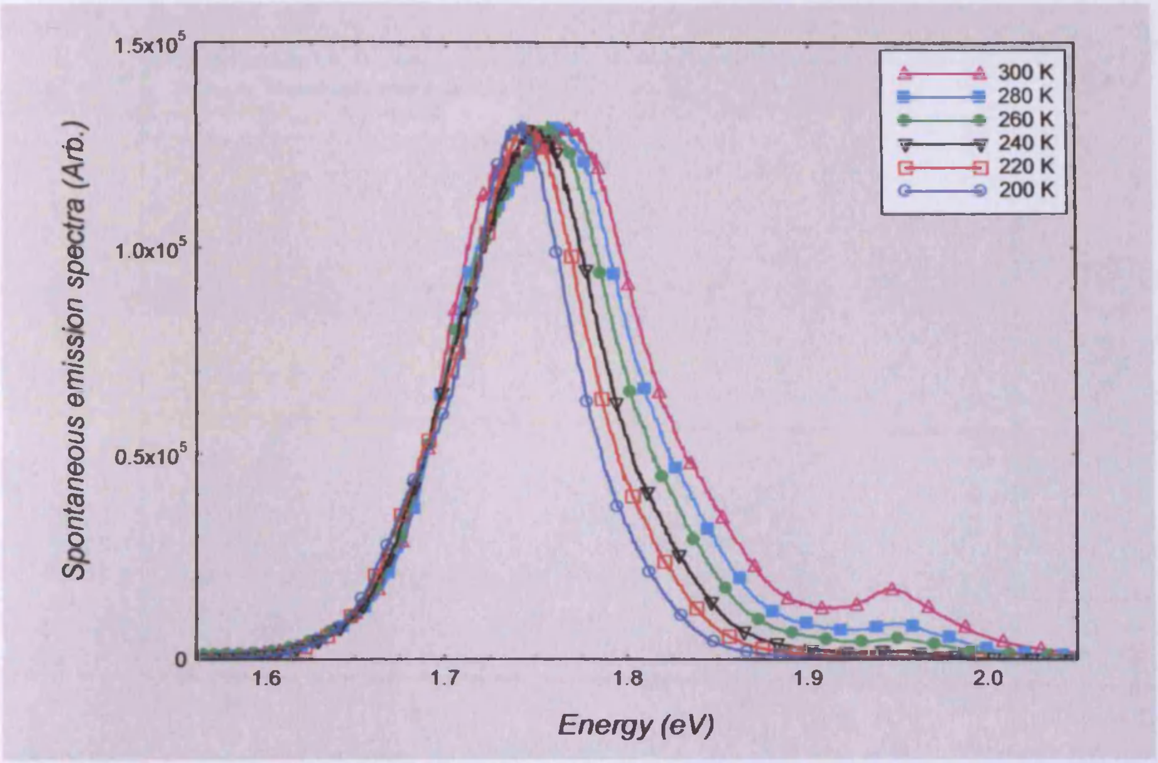

Figure 5.11 *Normalised spontaneous emission spectra for structure grown at 710°C. The symbols marked on each curve are a guide to the eye.*

by shifting their spectra. The shift is caused by the temperature change according to Equation 3.1 Chapter 3. The amounts of shifting required for correction are determined from Figures 5.8 and 5.9 for structures grown at temperatures of 750°C and 710°C respectively. This is done by measuring the distance from the absorption edge of each spectrum to one of them which used as a reference point. As a result of this, the corrected spontaneous emission spectra for structures grown at temperatures of 750°C and 710°C are shown in Figures 5.10 and 5.11 respectively. These shows a clear behaviour of the InP quantum dot peak width and the ratio of GaInP quantum well area as described previously in this chapter. This allowed measuring the change of these two

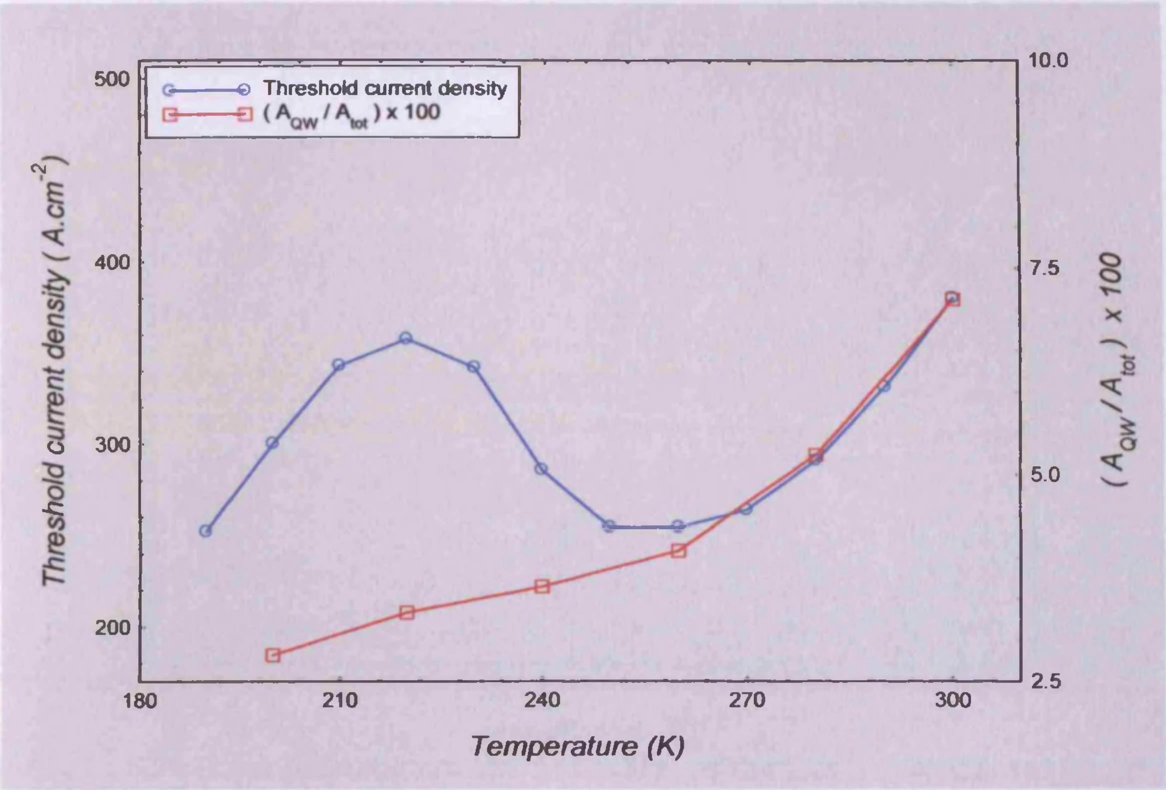

Figure 5.12 *Ratio of quantum well area versus temperature along with their threshold current density for structure grown at 750°C.*

parameters with a range of low temperatures as will be discussed later in this section.

5.7.2 Carrier Leakage from Quantum Dots

The carrier leakage from quantum dot to quantum well states is proportional to the ratio of the area of the spectrum at energies corresponding to the GaInP quantum well states to the total area A_{QW}/A_{tot}. This ratio is plotted as a function of temperature along with the threshold current density for structures grown at temperatures of 750°*C* and 710°*C* in Figures 5.12 and 5.13 respectively. In these figures the ratio of GaInP quantum well increases with increasing temperature

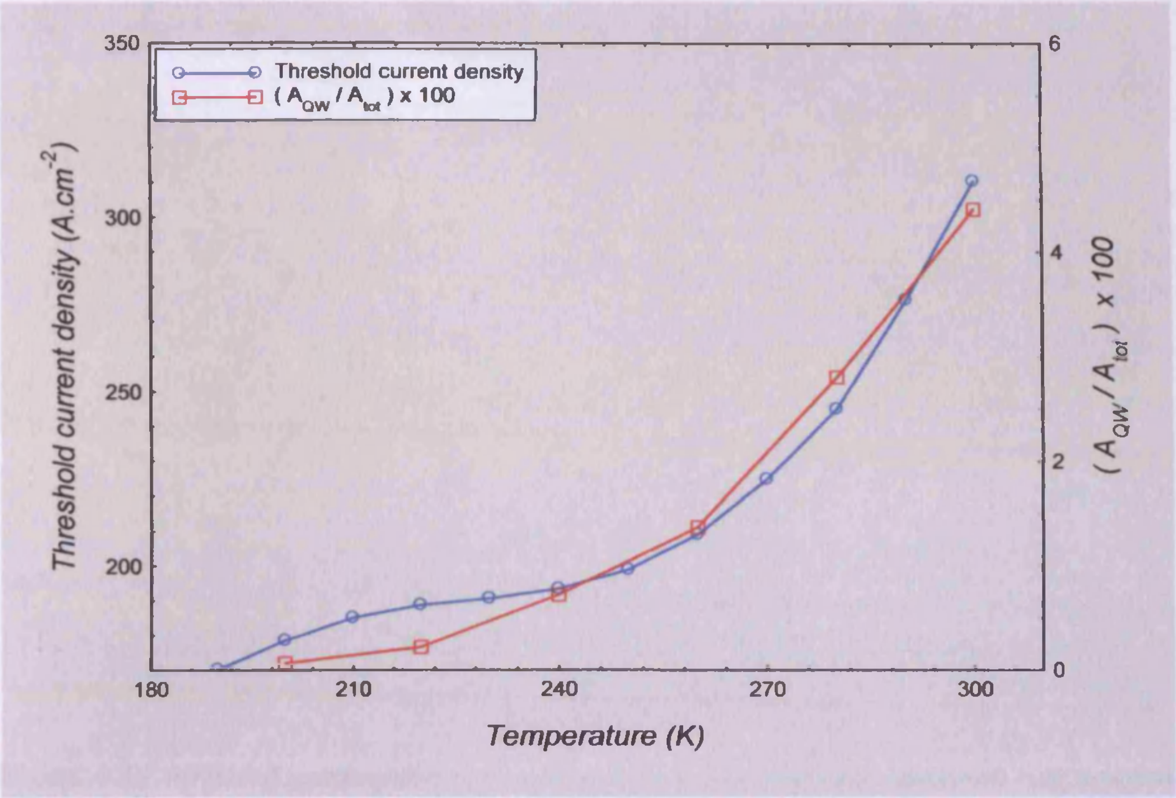

Figure 5.13 *Ratio of quantum well area versus temperature along with their threshold current density for structure grown at 710°C.*

indicating that part of the increase in threshold current density is due to loss of carriers from the dot states, but does not exhibit the reduction seen in the threshold current density of the 750°C growth temperature structure between 220K and 260K. This indicates that the distinctive behaviour of the threshold current density at low temperature is not because of the loss of carriers from the quantum dots to GaInP quantum well as shown in Figure 5.12.

5.7.3 Carrier Distribution in Quantum Dots

The carrier distribution in the studied structures is illustrated in this part. It is proportional to the full width half maximum FWHM of the InP quantum dot

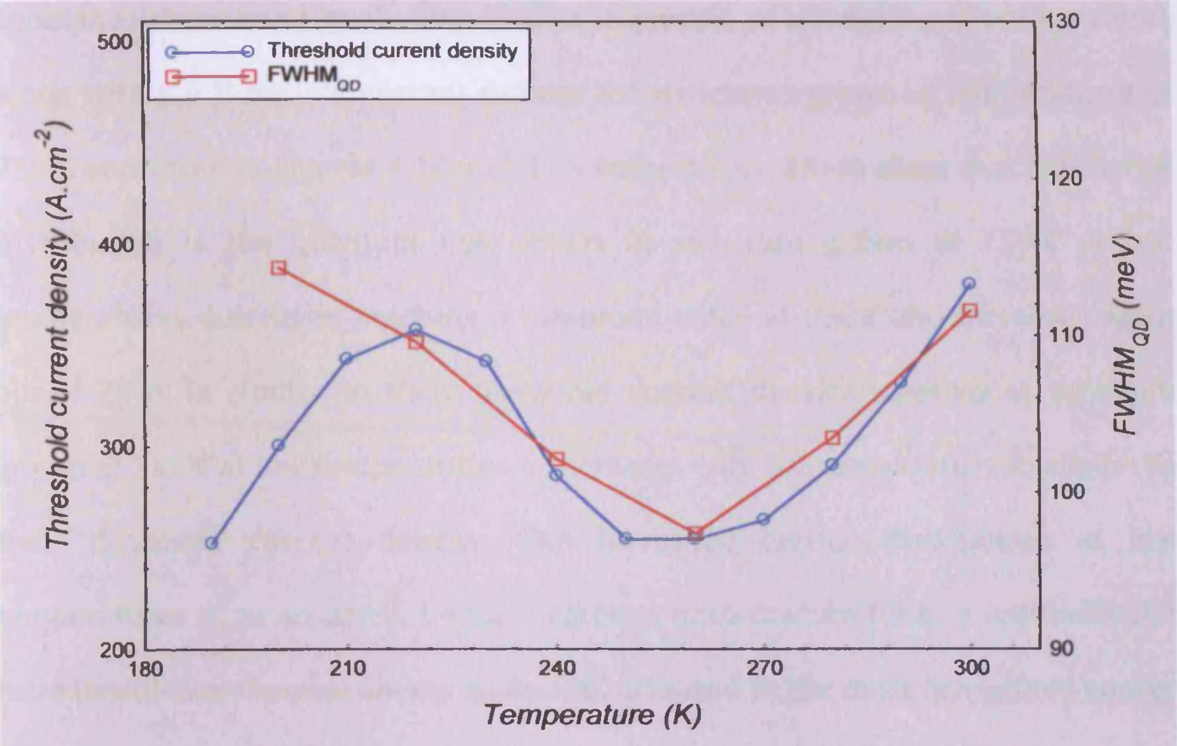

Figure 5.14 *FWHM of quantum dots peak at threshold versus temperature along with their threshold current density for structure grown at 750°C.*

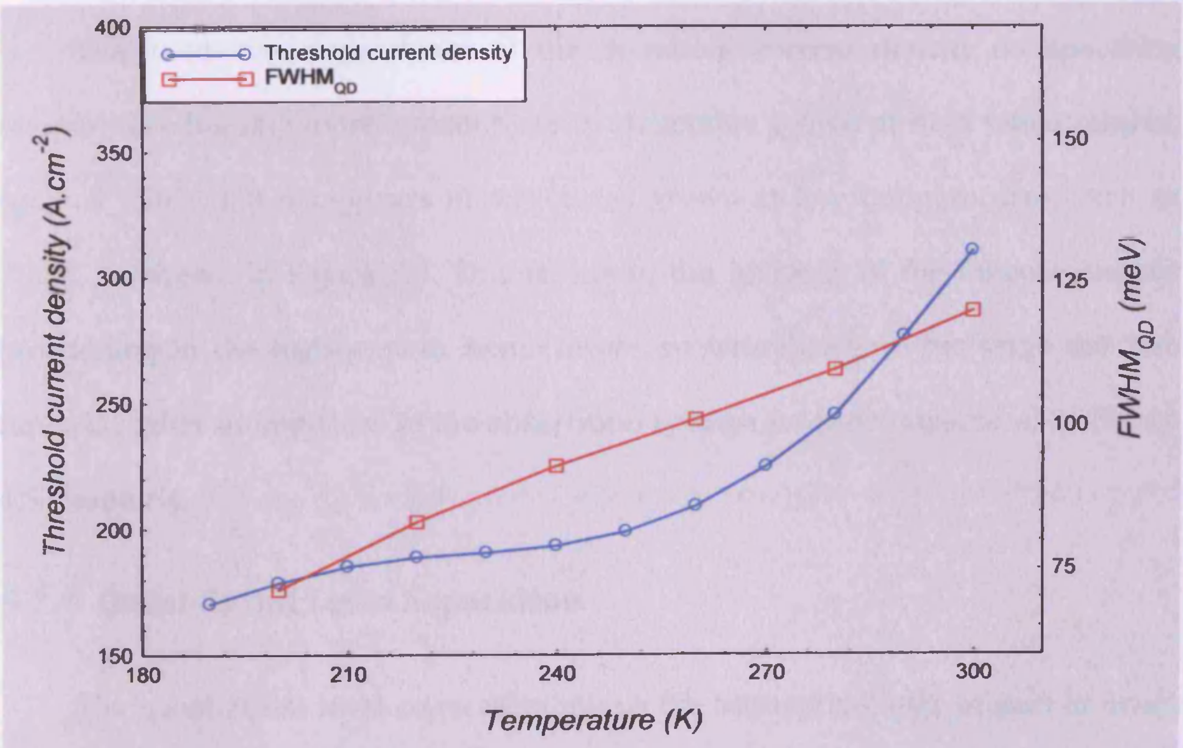

Figure 5.15 *FWHM of quantum dots peak at threshold versus temperature along with their threshold current density for structure grown at 710°C.*

spontaneous emission peak. This FWHM is plotted as a function of temperatures along with the threshold current density for structures grown at temperatures of $750^{\circ}C$ and $710^{\circ}C$ in Figures 4.14 and 4.15 respectively. These show that the carrier distribution in the quantum dots states in structure grown at $750^{\circ}C$ at low temperatures decreases, reaching a minimum value at $260K$ and increases again above $260K$ in similar to their threshold current density whereas in structure grown at $710^{\circ}C$ at low temperatures it increases with the temperature in similar to their threshold current density. The increased carrier distribution at low temperatures is, as assumed, because carriers once captured into a particular dot have insufficient thermal energy to be redistributed to the most favourable energy states (dots) for laser action, meaning more carriers are needed to sustain lasing causing a higher threshold current density.

The distinctive dependence of the threshold current density on operating temperature became more pronounced in structures grown at high temperatures, such as $750^{\circ}C$, but disappears in structures grown at low temperatures, such as $750^{\circ}C$, as shown in Figure 5.3. This is due to the increase of the inhomogeneous broadening in the high growth temperature structures where the large dot size range is higher as appeared in the absorption spectra for these structures in Figure 4.5 Chapter 4.

5.7.4 Quasi-Fermi Level Separation

The quasi-Fermi level separation minus the absorption edge at gain of $6cm^{-1}$ versus temperature for the studied structures are obtained from the gain and

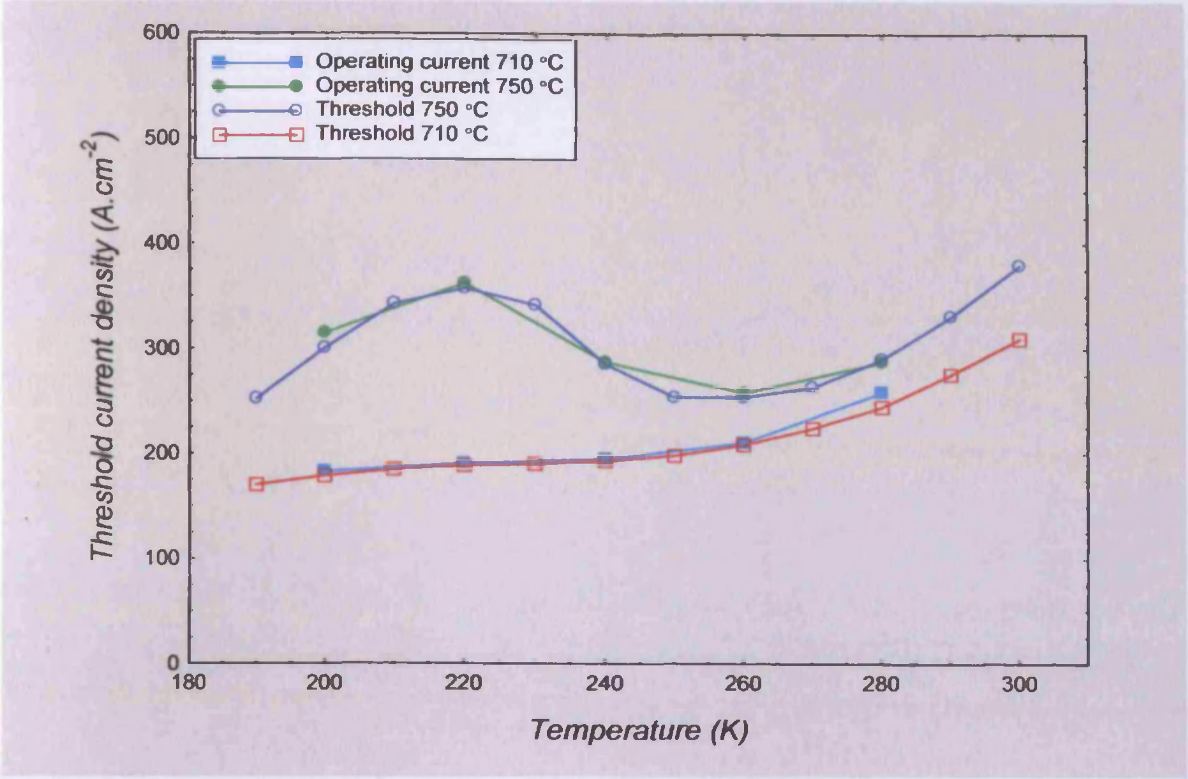

Figure 5.16 *Threshold and operating current densities versus temperatures for different growth temperature structures. The operating current was taken by Samuel Shutts* [2].

absorption spectra for structures grown at 750°C and 710°C shown in Figures 5.6 and 5.7 respectively. The operating currents at which these measurements are taken, measured by Samuel Shutts [2], are plotted in order to compare them with the threshold current densities for these temperatures for both growth temperatures as shown in Figure 5.16. The injected level, which is defined as the quasi-Fermi level separation minus the absorption edge, for structures grown at 750°C and 710°C required achieving a fixed modal gain equivalent to threshold gain of a 2mm long laser, as appear in Figures 5.6 and 5.7, is plotted in Figure 5.17. This indicates that the distinctive behaviour of the threshold current density at low temperature is not caused by a change in the injector level required to obtain a fixed value of gain or by a

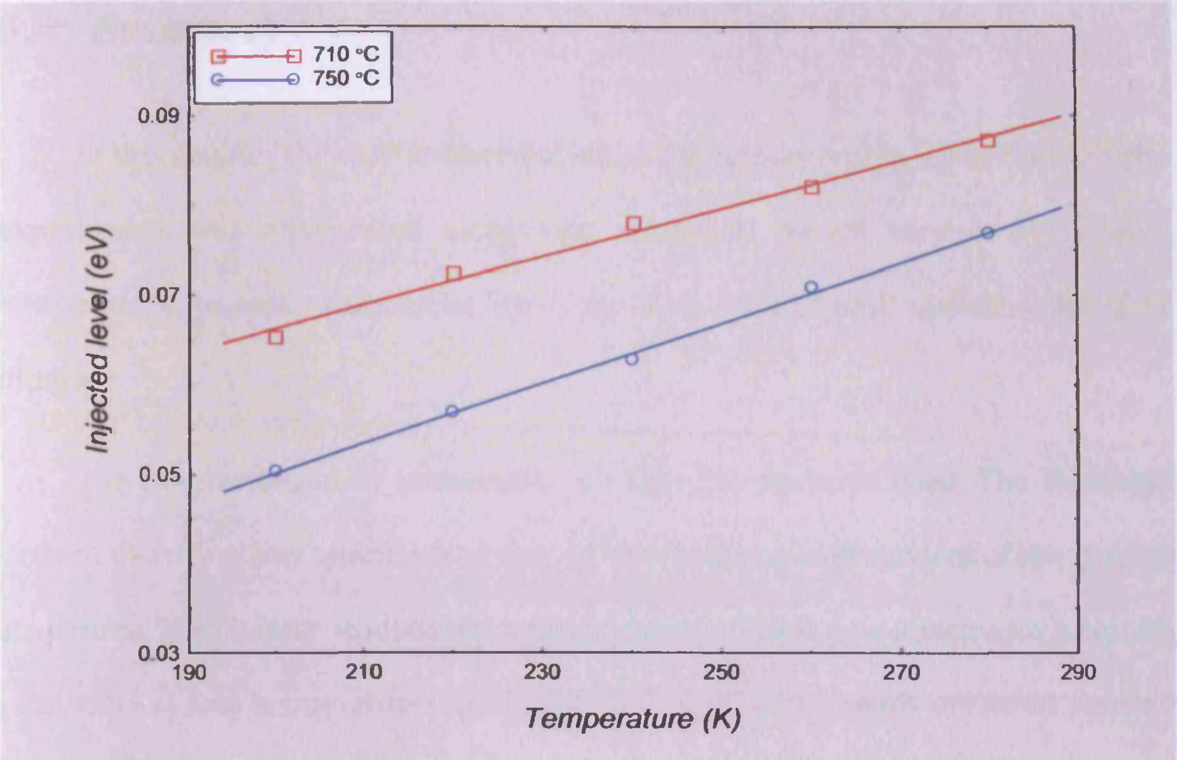

Figure 5.17 *Quasi-Fermi level separation minus absorption edge versus temperature for different growth temperature structures.*

change in the value of peak gain required but is caused by a process that requires an increase in the current density without increasing the injector level.

The data of Figure 5.14 suggests that it is the recombination in the extra states seen in Figure 5.14 that causes this change in current density, or that the same thing that causes this extra recombination and also causes the change in threshold current density.

5.8 Summary

In this chapter the carrier distribution at low temperatures taken from several experiments was interpreted using four structures, which vary in the growth temperature, to study the carrier distribution in InP/AlGaInP quantum dot laser diodes.

The chapter began by introducing the device structures used. The threshold current density at low temperature was evaluated using laser devices of the studied structures. The chapter studied the optical absorption and gain spectra for a certain gain value at low temperatures using the amplified spontaneous emission emitted from multisection devices. This presents the energy shift with temperature and also presents the quasi-Fermi level separation in the low temperature range. Afterwards, the spontaneous emission spectra at low temperatures taken for two of structures at their threshold currents were studied and this presents both the carrier distribution in quantum dots states and the carrier loss in the system. Both explain the increase of threshold current density at either low or high temperatures. The chapter evaluated the lasing wavelength at low temperatures for the studied structures. Finally, the chapter ended with studying the carrier distribution in different growth temperatures of InP/AlGaInP quantum dot laser diodes at low temperatures using the data presented in the chapter by different experiments.

References

[1] I. C. Sandall, P. M. Smowton, J. D. Thomson, T. Badcock, D. J. Mowbray, H. Y. Liu and M. Hopkinson, *"Temperature dependence of threshold current in p-doped quantum dot lasers"*, Applied Physics Letters, 89, p.151118 (2006).

[2] S. Shutts, M. S. Al-Ghamdi, G. T. Edwards, P. M. Smowton and A. B. Krysa, *"The origin of the Temperature dependence of threshold current density in InP/AlGaInP quantum dot laser structures"*, Semiconductor Integrated Optoelectronics, Cardiff, U.K., 6 – 8 April 2009.

CHAPTER 6

Quantity of Deposited Quantum Dot Material

6.1 Introduction

This chapter presents the quantity of deposited quantum dot material taken from several experiments using six structures, which vary in both the growth temperature and quantity of deposited material, to study their effect on optoelectronic properties of InP/AlGaInP quantum dot laser diodes.

The chapter begins by introducing the device structures used. The optical absorption spectra in high and low growth temperatures are studied using the amplified spontaneous emission emitted from multisection devices. The chapter evaluates the threshold current density as a function of temperature using laser devices. This is consistent with the behaviour of the optical absorption spectra in structures grown at low temperatures especially at low energies. The chapter studies the optical gain spectra for structures grown at high temperatures using the amplified spontaneous emission emitted from multisection devices and this verifies the threshold current density values by comparing the gain-current relations obtained from both the laser and multisection devices. Afterwards, the chapter describes the spontaneous emission spectra for structures grown at low temperatures taken with the same current at different temperatures and this presents the non-radiative recombination in the system which explains the increase of threshold current density at these structures. The chapter evaluates the lasing wavelength for the studied structures and finally, ends with estimating the amount of material in quantum dot as a function of the amount of deposited quantum dot material.

6.2 Device Structures

The device structures used in this chapter to study the quantity of deposited quantum dot material are described in this section. The device structures detail and the bandgap energy diagram versus growth distance for these structures are illustrated in Figures 3.7 and 3.8 respectively and listed in Table 3.5 Chapter 3. There are six structures used and they are similar but vary in two parameters. These parameters are the temperature at which the waveguide core is grown and the quantity of deposited quantum dot material. In this chapter, the comparison of growth temperatures at $690°C$ and $730°C$ are studied using structures containing 5 dot layers (each formed from 2 or 2.5 or 3 monolayers of InP) grown on $(Al_{0.3}Ga_{0.7})_{0.51}In_{0.49}P$ covered by $8nm$ $Ga_{0.51}In_{0.49}P$ quantum wells and separated by $8nm$ or $16nm$ wide $(Al_{0.3}Ga_{0.7})_{0.51}In_{0.49}P$ barrier layers for structures grown at $690°C$ and $730°C$ respectively.

The device structures were processed into multisection devices to measure the amplified spontaneous emission and also oxide isolated stripe lasers with top windows to measure the threshold current density as well as spontaneous emission as was described in Chapter 3.

6.3 Optical Absorption Spectra

The optical absorption spectra are studied in this section. This includes the optical absorption spectra for structures with high 730°C and low 690°C growth temperatures depending on the measurements of the amplified spontaneous emission obtained from the multisection device and calculated by using Equation 3.9 Chapter 3. Measurements of the modal absorption verses photon energy show the allowed transitions within the structures for each growth temperature at different quantities of deposited quantum dot material.

6.3.1 Modal Absorption in High Growth Temperatures

The absorption spectra for structures grown at temperature of 730°C with quantity of deposited quantum dot material of 2, 2.5 and 3ML are plotted in Figure 6.1. Previous studies, as mentioned previously in Chapter 4, shows that InP quantum dots grown on GaInP can be formed with a three dot size distributions, small, large and very large dots. The small and large dots are coherently strained while the very large dots are associated with defects in the material [1], [2]. As a result of this, the inhomogenously broadened transitions shown in Figure 6.1 shows a trimodal dot size distribution consist of large, small and very large dot size subsets.

For further analysis, the absorption spectra in Figure 6.1 have to be fitted with Gaussian curves. Fitting these spectra is difficult with the existence of the very large dot absorption which has a lot of states. Therefore the spectra are shifted vertically

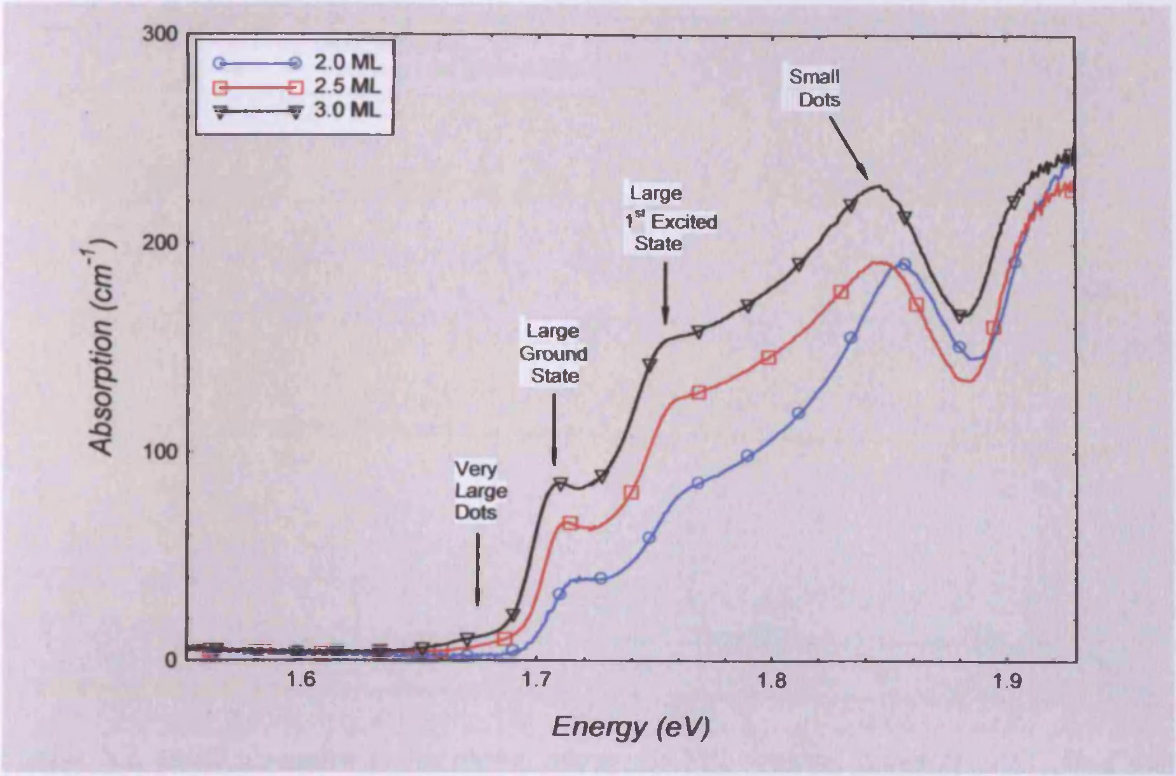

Figure 6.1 *Modal absorption versus photon energy for structures grown at 730°C. The symbols marked on each curve are a guide to the eye.*

to overcome the very large dot states after estimating its ground state by fitting one Gaussian at the lowest energy of the absorption spectra as shown in Figure 6.2. The shifted absorption spectra are fitted again with Gaussian curves. The agreement between the measured and the fitted data cannot be achieved by considering a monomodal dot size distribution within the structure, but is possible by considering a bimodal dot size distribution. The measured data for modal absorption is plotted along with the fitted data for structure with 2ML quantity of deposited quantum dot material grown at $730^{\circ}C$ in Figure 6.3. The spectrum in this figure is covered by four Gaussians to fit the large dots and two to fit the small dots. Each represents a particular state obeying Gaussian distribution. The energy

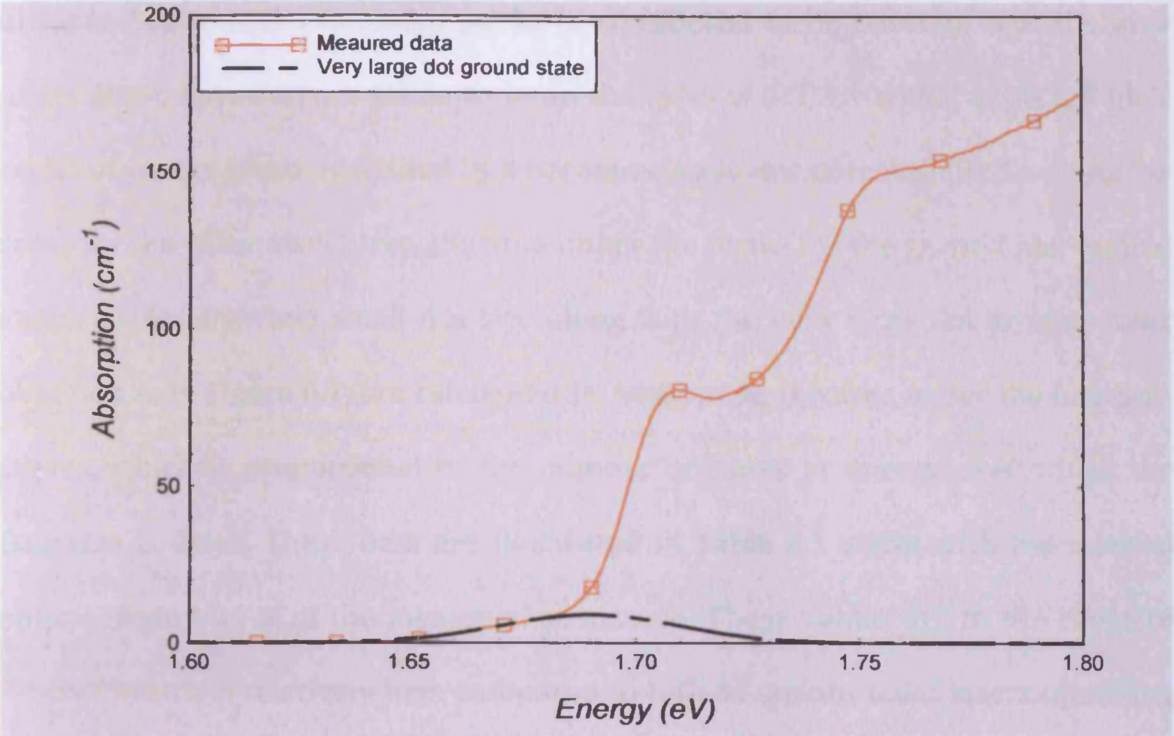

Figure 6.2 *Modal absorption versus photon energy for 3ML structure grown at 730°C fitted with Gaussian curve for ground state very large dot. The symbol marked on the curve is a guide to the eye.*

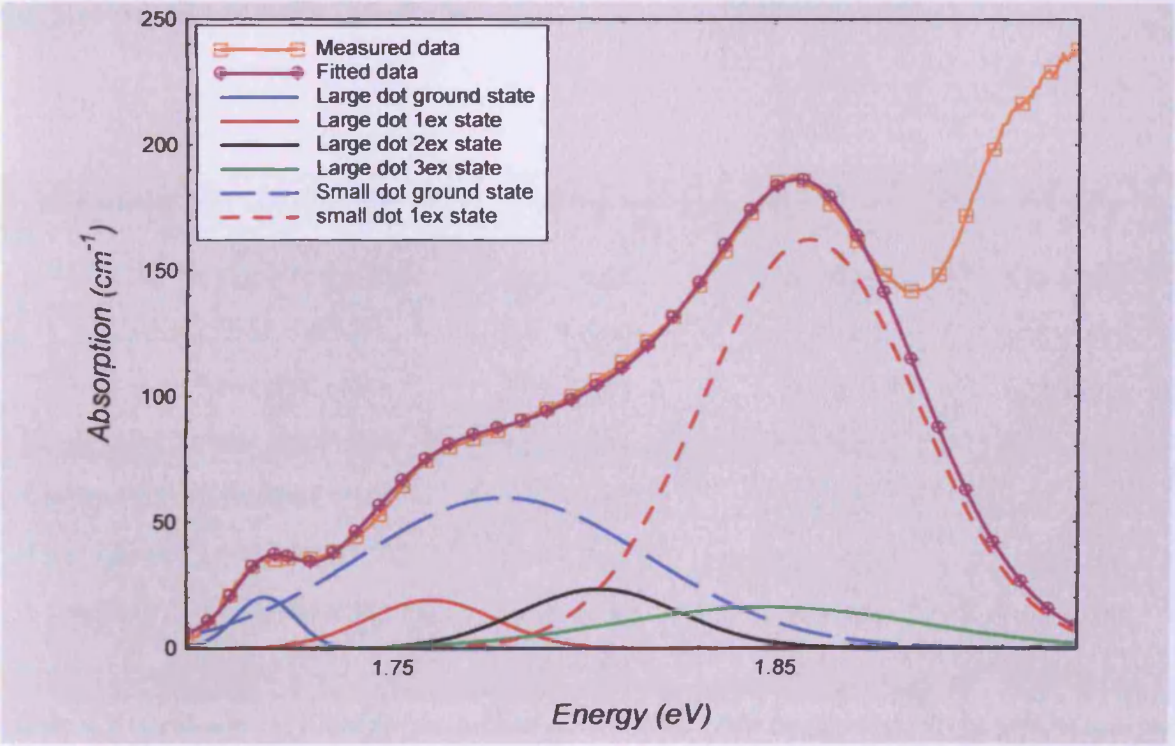

Figure 6.3 *Modal absorption versus photon energy for 2ML structure grown at 730°C fitted with Gaussian curves. The symbols marked on each curve are a guide to the eye.*

distance between the Gaussian peaks is considered to be constant and the area under these Gaussian are taken to be in the ratio of 1:2:3:4 which expected for a series of energy levels described by a harmonic oscillator potential [3]. By doing the same for the other structures, the area under the peaks for the ground and excited states of the large and small dot size along with the very large dot ground state, obtained as in Figure 6.2, are calculated by integrating the area under the Gaussian curves, which is proportional to the number of states at energy over which the Gaussian is fitted. These data are illustrated in Table 6.1 along with the internal optical mode loss α_i of the measured structures. These values are in the range of 3-5cm^{-1}, which is relatively high compared to InGaAs quantum dot lasers operating at 1.3μm, where it is typically in the range of 0-3cm^{-1}. The peak energy separation of the fitted dot states is 44meV for the large dot size subsets and 80meV for the small dot size subsets.

Area under the peak ($eV.cm^{-1}$)	2.0 ML	2.5 ML	3.0 ML
very large dot ground state	0.03 ± 0.05	0.18 ± 0.05	0.45 ± 0.05
large dot ground state	0.41 ± 0.05	0.69 ± 0.05	0.85 ± 0.05
large dot 1st excited state	0.82 ± 0.05	1.38 ± 0.05	1.70 ± 0.05
large dot 2nd excited state	1.23 ± 0.05	2.07 ± 0.05	2.55 ± 0.05
large dot 3ed excited state	1.64 ± 0.05	2.76 ± 0.05	3.40 ± 0.05
small dot ground state	5.70 ± 0.05	5.90 ± 0.05	6.85 ± 0.05
small dot 1st excited state	11.40 ± 0.05	11.80 ± 0.05	13.70 ± 0.05
α_i (cm^{-1})	3.6	3.5	3.0

Table 6.1 *Area under the peaks for ground and excited states of the large and small dot, ground state for the very large dot along with the internal optical mode loss values for structures grown at 730°C.*

6.3.2 Modal Absorption in Low Growth Temperatures

The absorption spectra for structures grown at temperature of 690°C with quantity of deposited quantum dot material of 2, 2.5 and 3ML are plotted in Figure 6.4. The absorption spectra for these structures show similar trends to that for structures grown at temperature of 730°C but in this case the magnitude of absorption at the low energy states is larger and the very low energy states, which are believed correspond to very large dots, have much increased magnitude as compared to structures grown at temperature of 730°C. This can be seen when comparing both Figures 6.1 and 6.4. The higher magnitude of the very large dot peak typically occurs in structures with a higher threshold current density. This

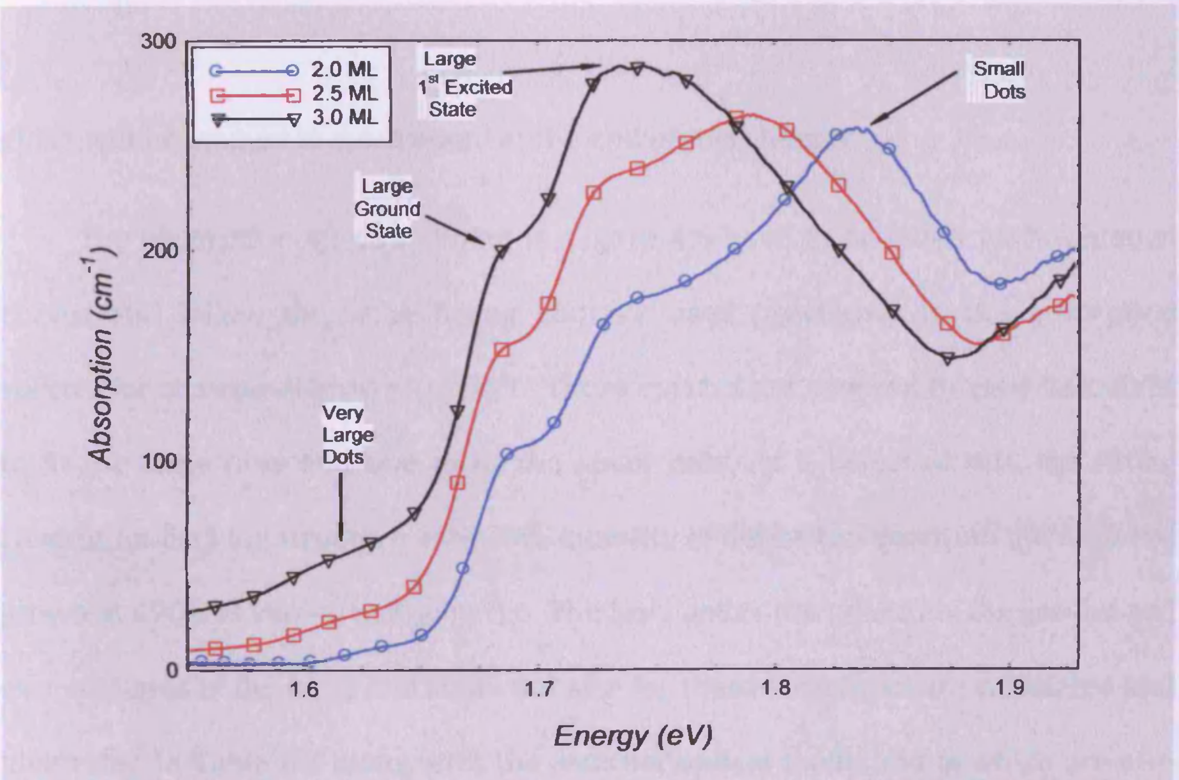

Figure 6.4 *Model absorption versus photon energy for structures grown at 690°C. The symbols marked on each curve are a guide to the eye.*

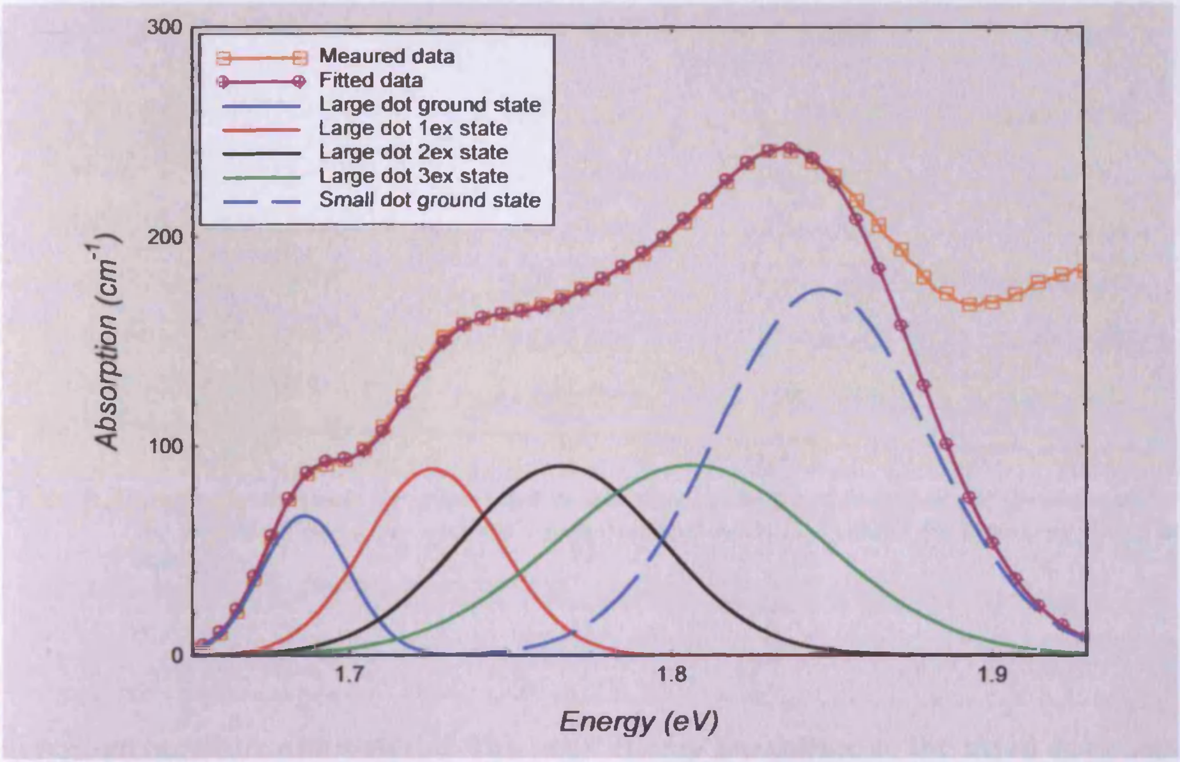

Figure 6.5 *Model absorption versus photon energy for 2ML structure grown at 690°C fitted with Gaussian curves. The symbols marked on each curve are a guide to the eye.*

effect will be studied in more detail at the end of this chapter.

The absorption spectra shown in Figure 4.6 have to be fitted with Gaussian curves and follow the same fitting analysis used previously to the absorption spectra for structures grown at 730°*C*. These spectra are covered by four Gaussians to fit the large dots and one to fit the small dots. As a result of this, the fitting absorption data for structure with 2ML quantity of deposited quantum dot material grown at 690°*C* is shown in Figure 5.6. The area under the peaks for the ground and excited states of the large and small dot size for these structures are calculated and illustrated in Table 6.2 along with the internal optical mode loss α_i which are also higher for these latter structures. These values show an increase with quantity of

Area under the peak (eV.cm^{-1})	2.0 ML	2.5 ML	3.0 ML
very large dot ground state	0.69 ± 0.05	1.23 ± 0.05	2.45 ± 0.05
large dot ground state	2.34 ± 0.05	2.62 ± 0.05	3.11 ± 0.05
large dot 1st excited state	4.68 ± 0.05	5.24 ± 0.05	6.22 ± 0.05
large dot 2nd excited state	7.02 ± 0.05	7.86 ± 0.05	9.33 ± 0.05
large dot 3ed excited state	9.36 ± 0.05	10.50 ± 0.05	12.40 ± 0.05
small dot ground state	14.50 ± 0.05	7.88 ± 0.05	0.00 ± 0.05
α_i (cm^{-1})	3.3	9.6	27.5

Table 6.2 *Area under the peaks for ground and excited states of the large and small dot, ground state for the very large dot along with the internal optical mode loss values for structures grown at 690°C.*

deposited quantum dot material. The peak energy separation of the fitted dot states is $40meV$ for the large dot size subsets.

The very large dot ground state for these structures are estimated similarly as done for structures grown at high temperatures and illustrated in Table 6.2.

6.4 Threshold Current Density

The threshold current density as a function of temperature is studied in this section. The section starts by discussing the light-current characteristics changes with temperature in which the threshold current as a function of temperature can be determined. This is done by using 2*mm* long laser devices with the structures studied in the previous section.

6.4.1 Threshold Current

The light-current characteristics have been investigated using the current voltage light temperature I-V-L-T measurement experiment, which is described in

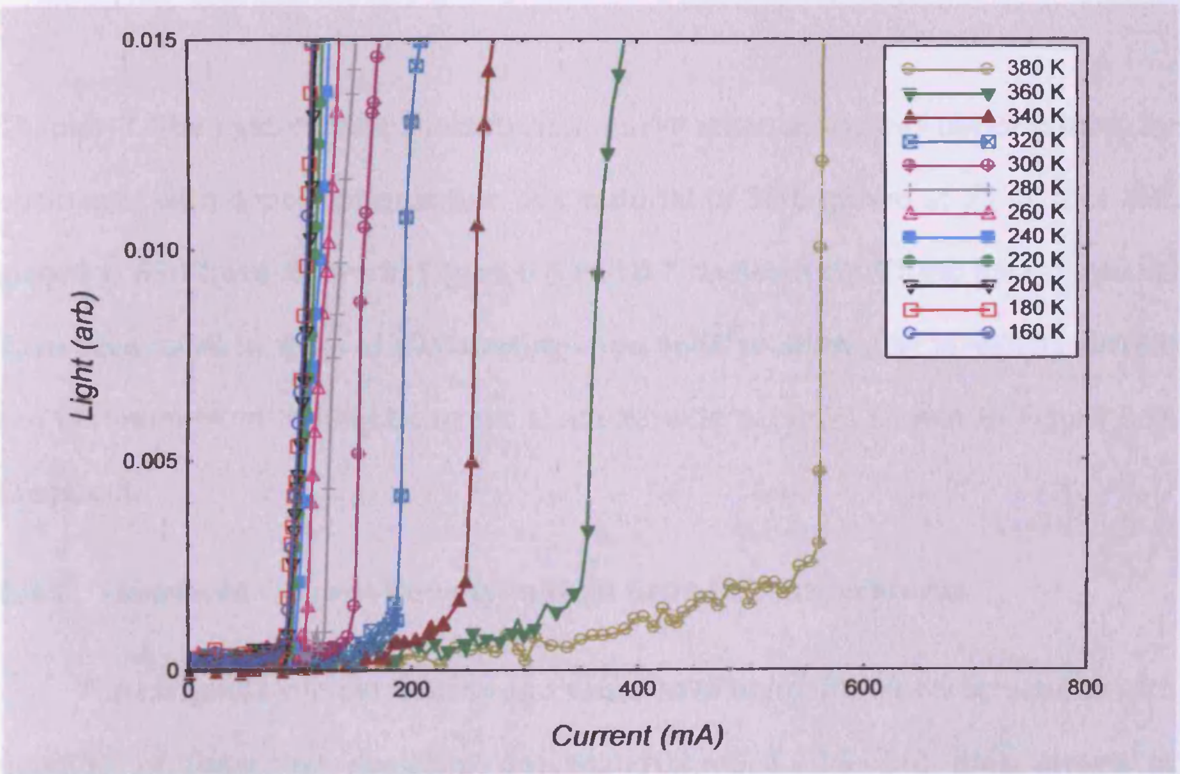

Figure 6.6 *Light-current characteristic curves for structure with deposited QD material of 3ML grown at temperature of 730°C. The symbols marked on each curve are a guide to the eye.*

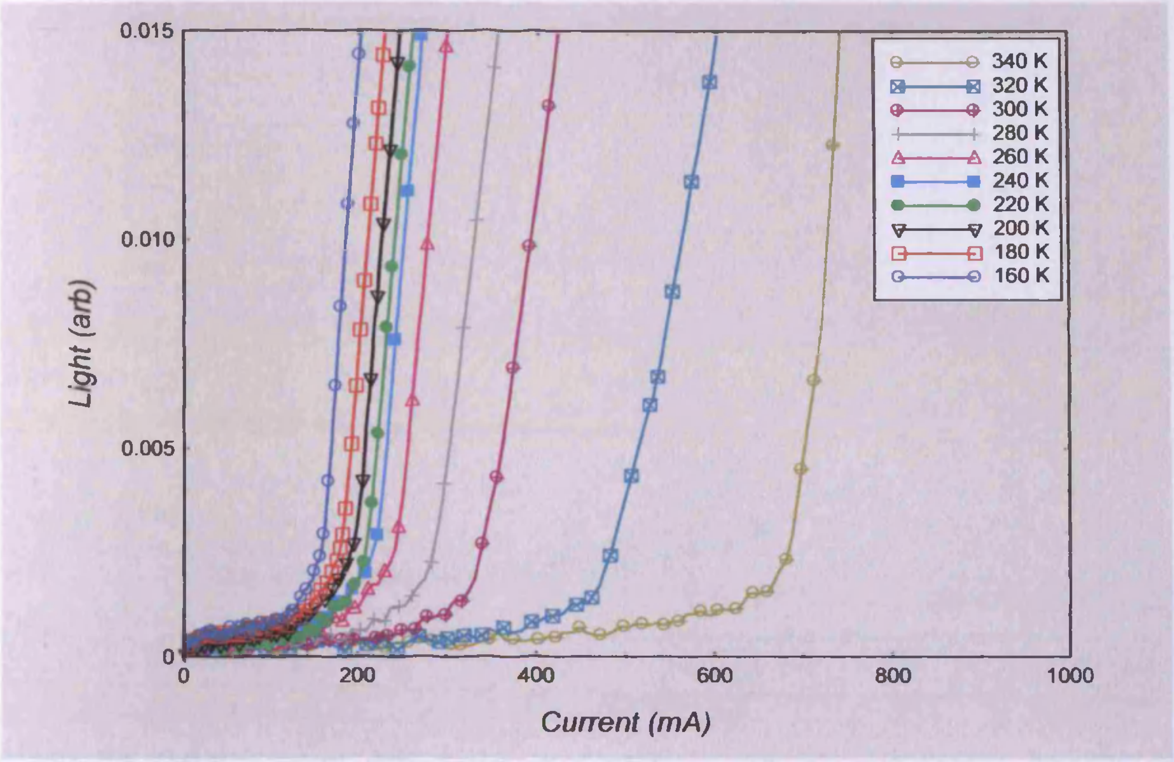

Figure 6.7 *Light-current characteristic curves for structure with deposited QD material of 2ML grown at temperature of 690°C. The symbols marked on each curve are a guide to the eye.*

Chapter 3. The light-current characteristic curve taken at various temperatures for structures with deposited quantum dot material of 3ML grown at 730°C and 2ML grown at 690°C are shown in Figure 6.6 and 6.7 respectively. These measurements have been taken in steps of 10K starting from 160K to 380K. The threshold current can be found from the light-current characteristic curve as shown in Figure 3.16 Chapter 3.

6.4.2 Threshold Current Density in High Growth Temperatures

The threshold current density as a function of temperature for structures with quantity of deposited quantum dot material of 2, 2.5 and 3ML grown at temperature of 730°C obtained from the light–current characteristic curves and

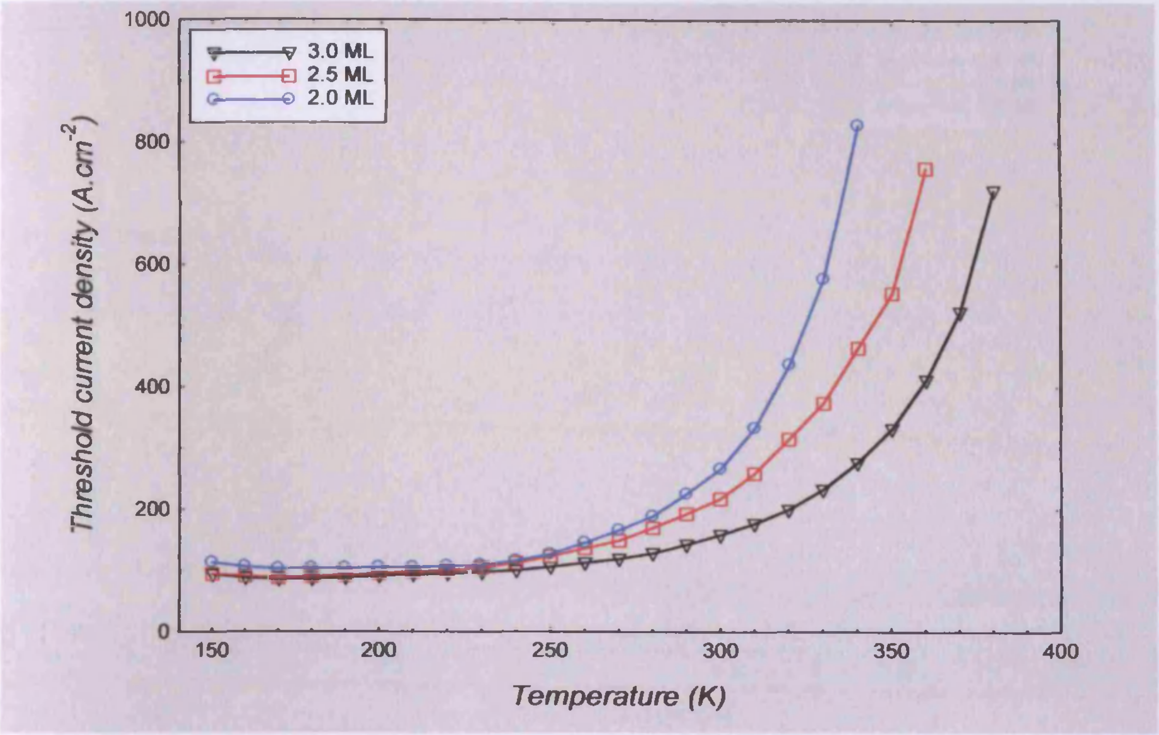

Figure 6.8 *Threshold current density versus temperature for structures with different deposited QD material grown at temperature of 730°C.*

calculated by using Equation 3.3 Chapter 3 are plotted in Figure 6.8. This figure shows a nonlinear increase to the threshold current density as the temperature increases due to thermal energy which has been discussed previously in Chapter 4. The threshold current density in Figure 6.8 shows that the 3ML sample has the lowest threshold current density. The threshold current density increases when the quantity of deposited quantum dot material in the structure decreases. This will be discussed later in this chapter.

6.4.3 Threshold Current Density in Low Growth Temperatures

The threshold current density as a function of temperature for structures with quantity of deposited quantum dot material of 2, 2.5 and 3ML grown at

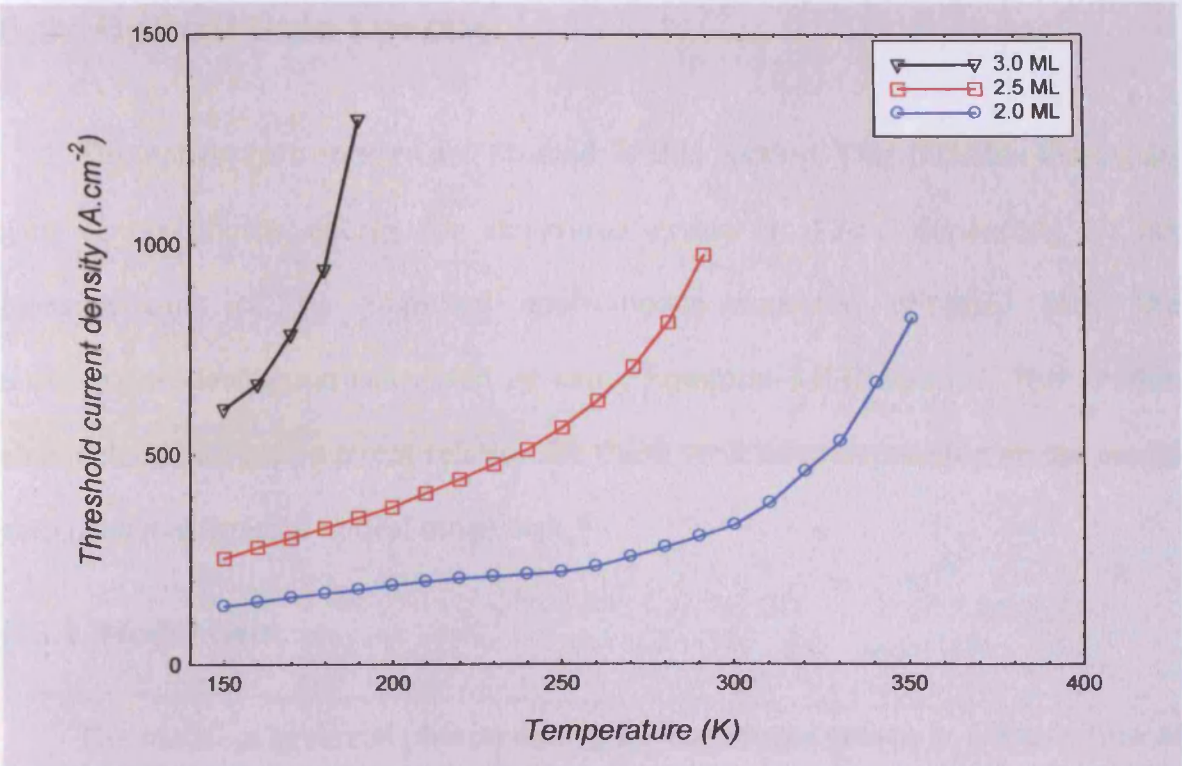

Figure 6.9 *Threshold current density versus temperature for structures with different deposited QD material grown at temperature of 690°C.*

temperature of 690°*C* obtained from the light-current characteristic curves and calculated by using Equation 3.3 Chapter 3 are plotted in Figure 6.9. This figure also shows a nonlinear increase to the threshold current density as the temperature increases due to thermal energy. The threshold current density in Figure 6.9 shows that the 3ML sample exhibits the highest threshold current density, even though they contain the largest number of states available for lasing. This value decreases with the quantity of deposited quantum dot material. The reason for all this will be discussed later in this chapter.

6.5 Optical Gain Spectra

The optical gain spectra are studied in this section. This includes the modal gain versus photon energy for structures grown at 730°C depending on the measurements of the amplified spontaneous emission obtained from the multisection device and calculated by using Equation 3.8 Chapter 3. This section also includes the gain-current relation for these structures depending on the modal gain peak and internal optical mode loss.

6.5.1 Modal Gain

The modal gain versus photon energy for structures grown at temperature of

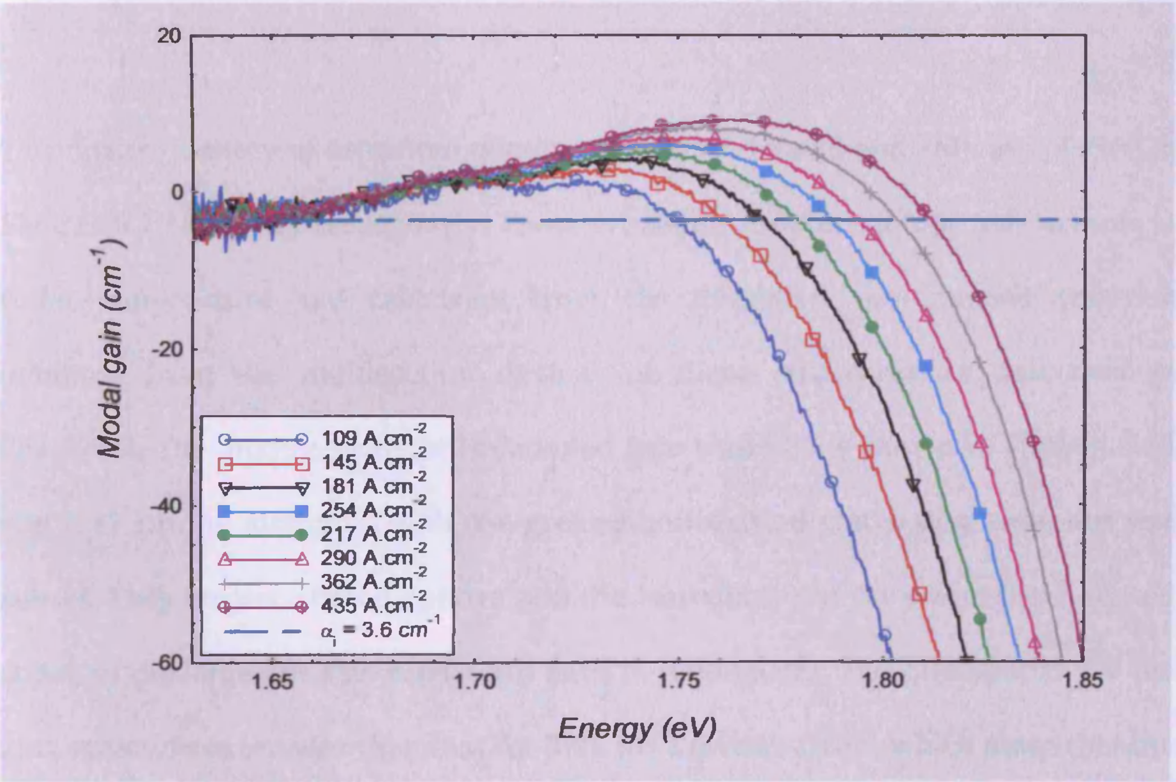

Figure 6.10 *Modal gain versus photon energy for structure with quantity of deposited QD material of 2ML grown at 730°C. The symbols marked on each curve are a guide to the eye.*

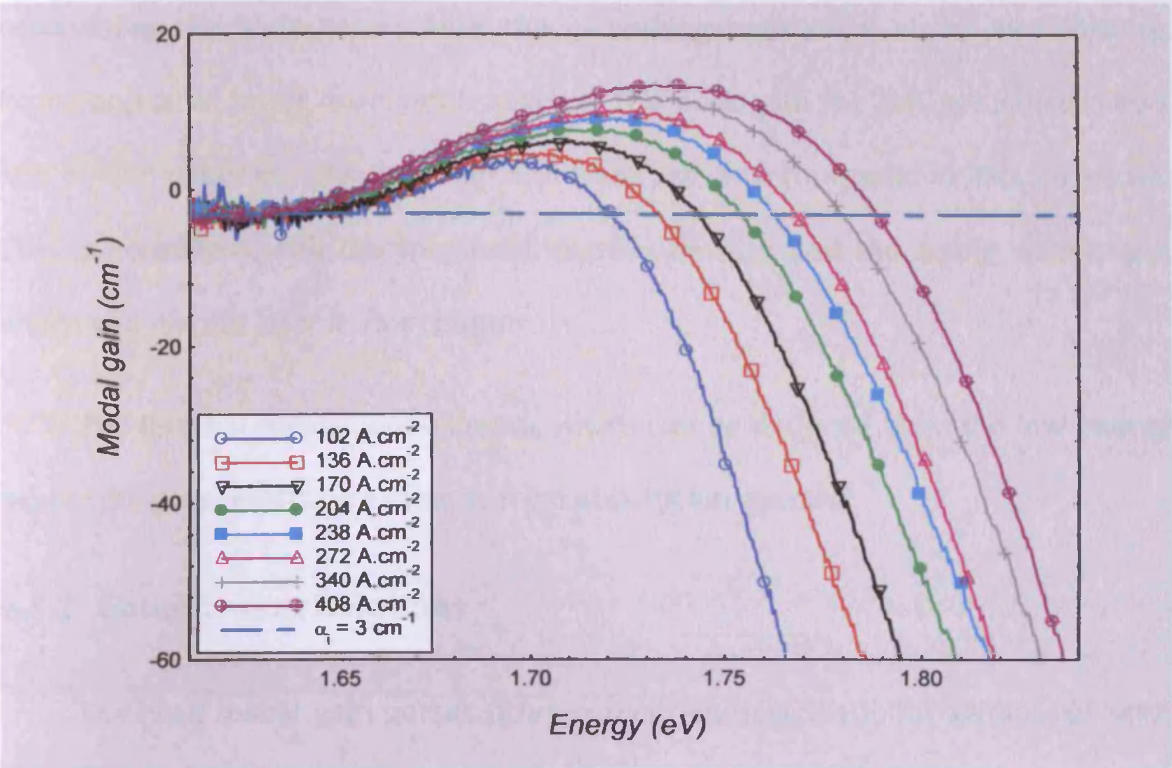

Figure 6.11 *Modal gain versus photon energy for structure with quantity of deposited QD material of 3ML grown at 730°C. The symbols marked on each curve are a guide to the eye.*

730°C with quantity of deposited quantum dot material of 2 and 3ML are plotted in Figures 6.10 and 6.11 respectively. These are taken at different injected currents at room temperature and calculated from the amplified spontaneous emission obtained from the multisection devices of these structures as described in Chapter 3. The inhomogenously broadened gain transitions shown in Figures 6.10 and 6.11 can be identified with the ground and excited states of a large dot size subset. They are very broad spectra and the emission from the ground and excited states of the large dot size subset are hard to distinguish. The gain spectra for the 2ML structure is broader than that for 3ML for a given current which mean that the gain is spread over higher range of photon density due to the inhomogeneous broadening which decreases with the increasing number of states available for lasing appeared in the absorption spectra. The peak gain for 3ML structure shows also higher values at a given current and small red shift compared to 2ML structure. This is consistent with the threshold current density and the lasing wavelength which will discuss later in this chapter.

The internal optical mode loss α_i, which can be deduced from the low energy part of the gain spectra, are same as from absorption spectra.

6.5.2 Gain-Current Relations

The peak modal gain versus drive current characteristic for structures with

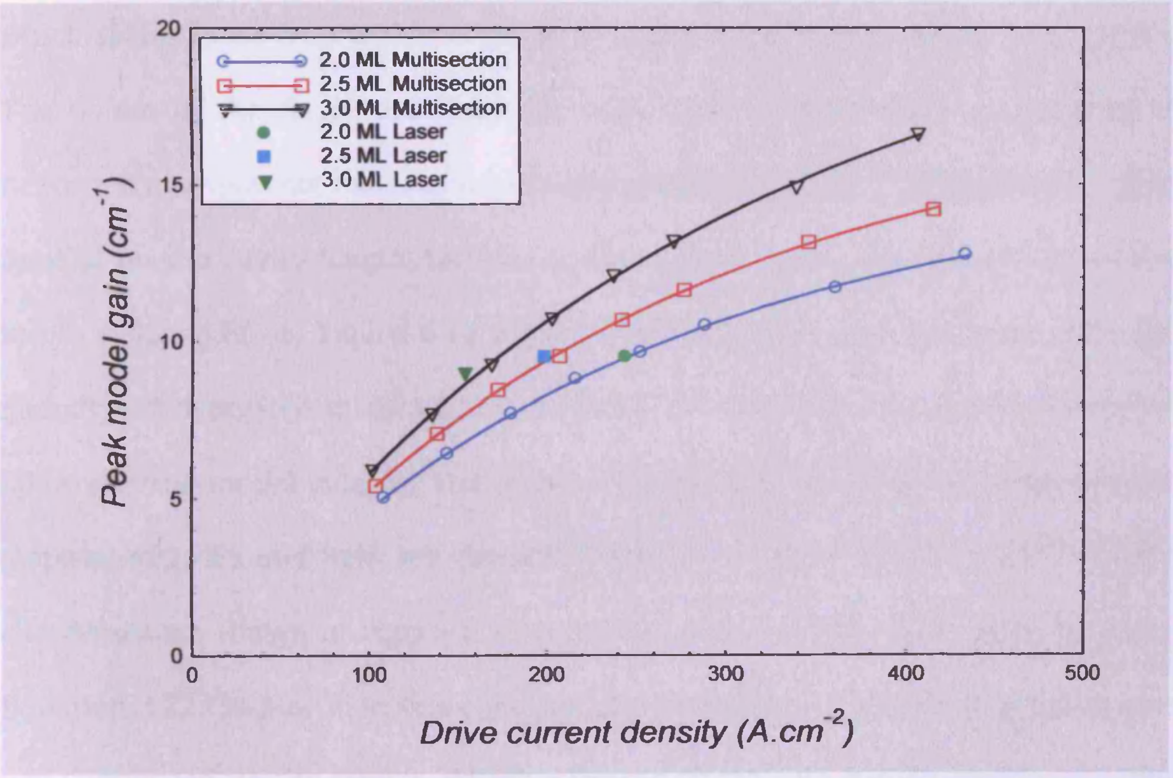

Figure 6.12 *Gain-current relations for structures with different quantity of deposited QD material grown at 730°C. The (solid points) are the gain-current of the lasers at room temperature. The lines are fits of Equation 2.22 of the multisection data.*

Quantity of Deposited QD material	J_t $(A.cm^{-2})$	G_s (cm^{-1})
2.0 ML	10.8 ± 0.5	15.5 ± 0.5
2.5 ML	12.6 ± 0.5	17.8 ± 0.5
3.0 ML	14.2 ± 0.5	22.3 ± 0.5

Table 6.3 *Transparency current density and modal gain saturation list for structures with 16nm barrier width.*

different quantity of deposited quantum dot material grown at temperature of $730°C$ is shown in Figure 6.12. These obtained partially from the peaks of the gain spectra shown in Figures 6.10 and 6.11. As mentioned in Chapter 4, the studying of the gain-current relation of these structures is to check the consistency of their measurements from the laser devices with these from the multisection devices, which seems to be true within error as in Figure 6.12, where the error is $\pm 1cm^{-1}$. The points in the figure are from the laser devices with different quantity of deposited quantum dot material calculated by using Equation 2.12 Chapter 2, which depend on the cavity length, internal optical mode loss α_i and reflectivity of the facets R. In addition, Figure 6.12 shows that the modal gain increases with the quantity of deposited quantum dot material, for example, at current density of $200A/cm^2$ the model gain for structures with quantity of deposited quantum dot material of 2, 2.5 and 3ML are about 8.4, 9.5 and $10.6cm^{-2}$ respectively. The data characteristics shown in Figure 6.12 are fitted with a curve represented by using Equation 2.22 Chapter 2. In this equation, the constants γ for the fitting parameter was estimated to be about 0.048 whereas J_t and G_s which stands for the transparency current density and modal gain saturation respectively are listed in

Table 6.3 for each quantity of deposited quantum dot material. These parameters increase with the quantity of deposited quantum dot material. This is consistent with the increasing number of states when increasing quantity of deposited quantum dot material as seen in the absorption spectra of Figure 6.1.

6.6 Spontaneous Emission Spectra

The spontaneous emission spectra are studied in this section. This includes the spontaneous emission spectra for structures with different quantity of deposited quantum dot material grown at temperature of $690^{\circ}C$ depending on the measurements of the spontaneous emission obtained from the top window of the laser devices. These measurements of the spontaneous emission are taken at different temperatures for each quantity of deposited quantum dot material.

6.6.1 Selection of Currents

In order to compare spontaneous emission spectra of different structures, the injected current densities, at which these spontaneous emissions spectra were taken, are selected at the same value of $100A.cm^{-2}$. These measurements are detected by the experiment described in Chapter 3 through the same collection geometry.

6.6.2 Spontaneous Emission and Temperature

The spontaneous emission spectra taken through a top-contact window of the laser devices with the same injected current densities at temperatures of $100K$, $200K$ and $300K$ for structures with quantity of deposited quantum dot material of 2, 2.5 and 3ML grown at temperature of $690^{\circ}C$ are plotted in Figures 6.13, 6.14 and 6.15 respectively. These show a higher emission from the 3ML sample at $100K$ but the rate of decrease in spontaneous emission spectra (which occurs for all samples) is higher for this sample and results in higher spontaneous emission from the 2ML

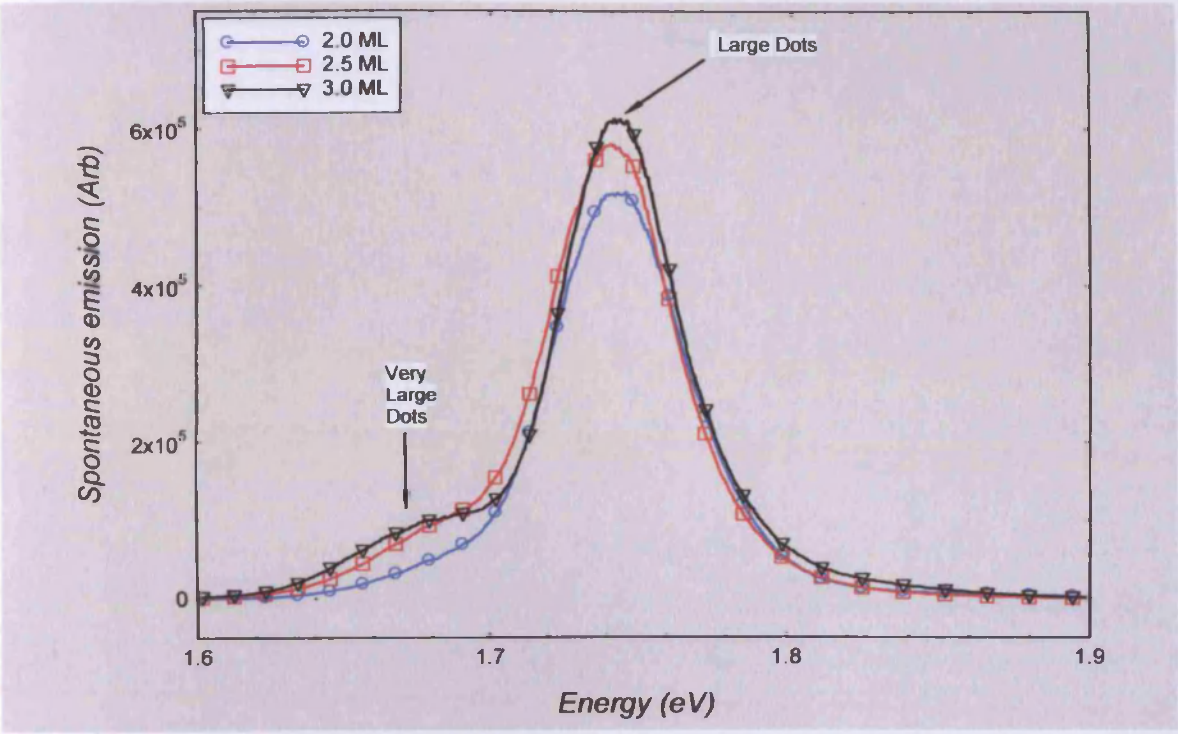

Figure 6.13 *Spontaneous emission spectra at 100K for structures with different quantity of deposited QD material grown at 690°C taken at the same current. The symbols marked on each curve are a guide to the eye.*

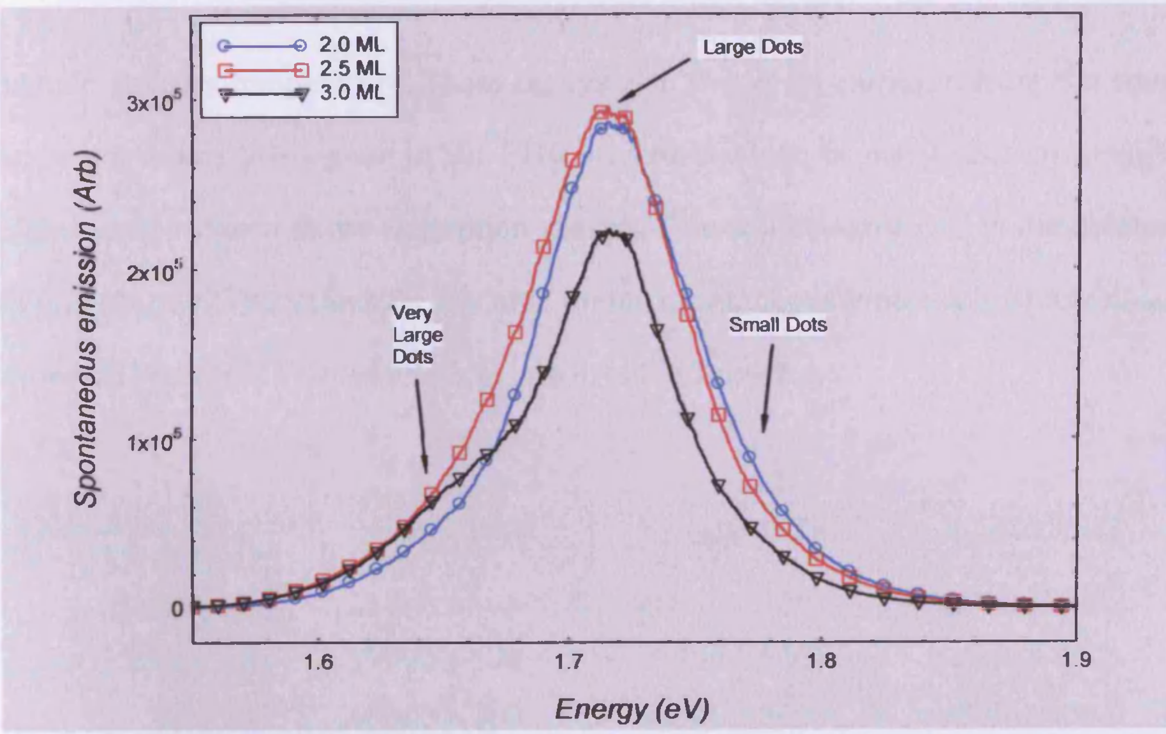

Figure 6.14 *Spontaneous emission spectra at 200K for structures with different quantity of deposited QD material grown at 690°C taken at the same current. The symbols marked on each curve are a guide to the eye.*

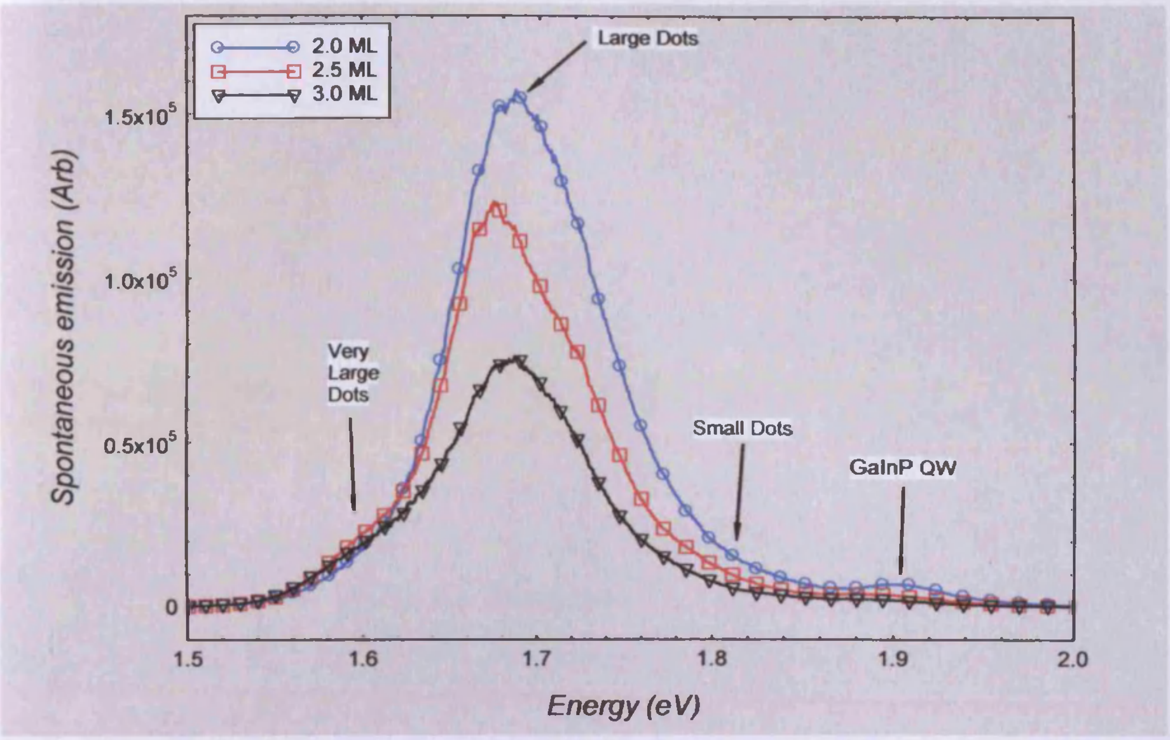

Figure 6.15 *Spontaneous emission spectra at 300K for structures with different quantity of deposited QD material grown at 690°C taken at the same current. The symbols marked on each curve are a guide to the eye.*

sample at room temperature. These figures also shows an emission from the very large dot states are higher in the 3ML structure which is consistent with their higher states shown in the absorption spectra. This will be explained in detail later in this chapter. The values for the area under spontaneous emission spectra A_{spon}, shown in Figures 6.13, 6.14 and 6.15, are listed in Table 6.4.

Quantity of Deposited QD material	A_{spon} at $100K$	A_{spon} at $200K$	A_{spon} at $300K$
2.0 ML	34200 ± 500	26800 ± 500	18700 ± 500
2.5 ML	39000 ± 500	28500 ± 500	14100 ± 500
3.0 ML	40600 ± 500	20500 ± 500	9300 ± 500

Table 6.4 *Area under spontaneous emission spectra for different quantity of deposited QD material taken at different temperatures with the same injected current density.*

6.7 Lasing Wavelength

The lasing wavelength changes with both the temperature and quantity of deposited quantum dot material are studied in this section. The lasing wavelength for structures with quantity of deposited quantum dot material of 2, 2.5 and 3ML grown at temperature of $690°C$ taken at various temperatures are shown in Figure 6.16 depending on the measurements emitted from the laser device using the experimental setup shown in Figure 3.18 Chapter 3. The lasing wavelength is determined by selecting the wavelength of the highest peak in the characteristic of the light intensity versus wavelength, as shown in Figure 3.19 Chapter 3. Figure 6.16 shows that the lasing wavelength increases linearly with temperature

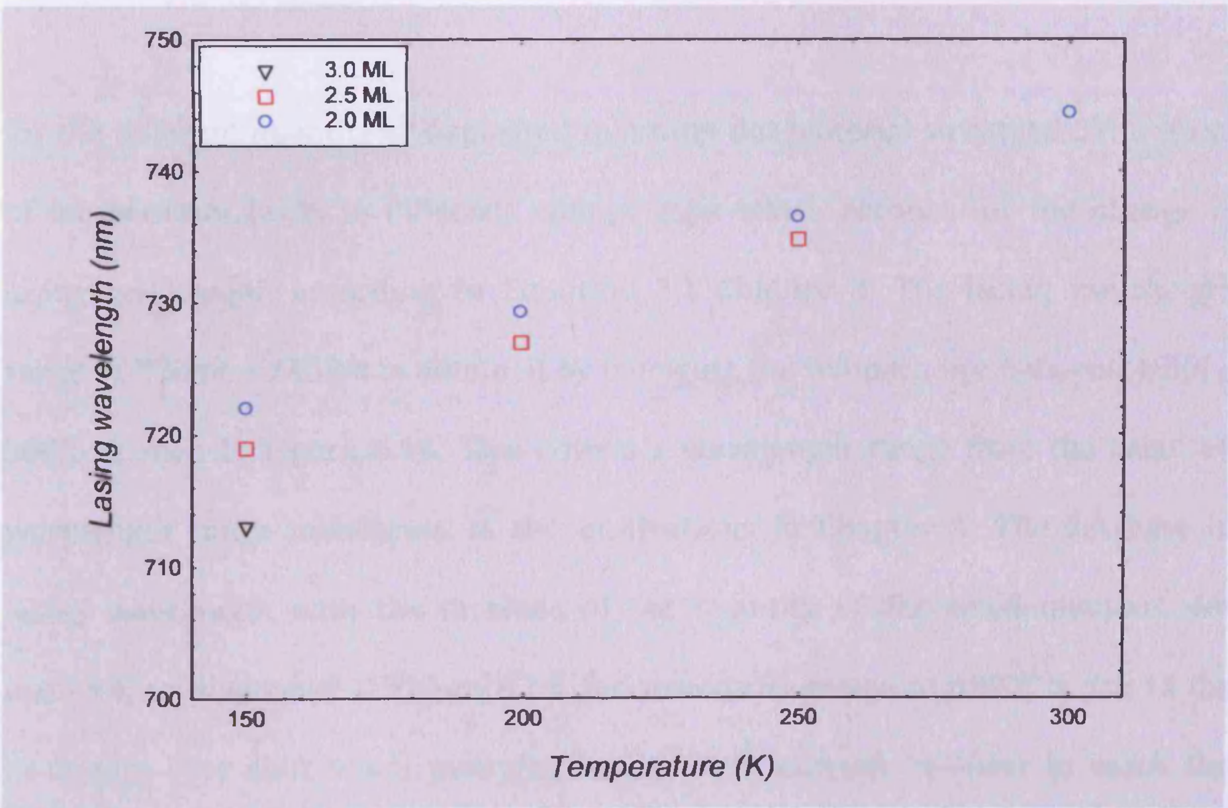

Figure 6.16 *Lasing wavelengths versus temperature for structures with different quantity of deposited QD material grown at 690°C.*

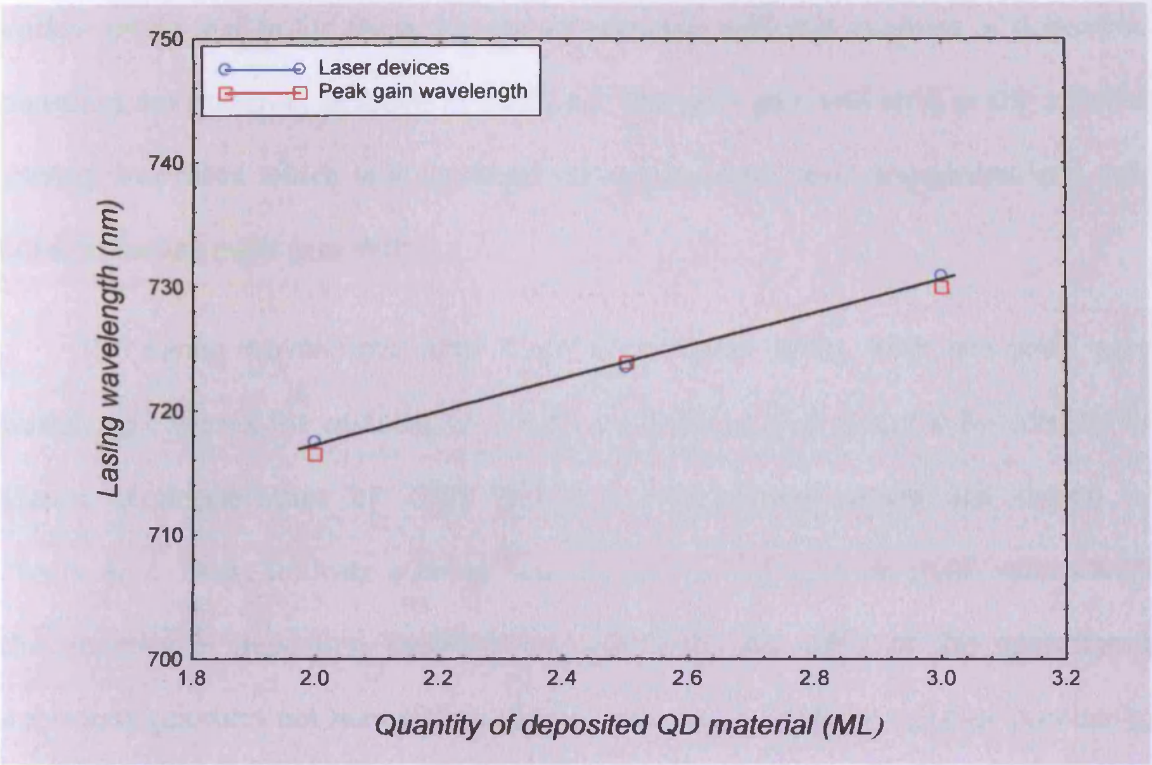

Figure 6.17 *Lasing wavelengths and peak modal gain versus quantity of deposited QD material for structures grown at 730°C taken at room temperature.*

for the different quantity of deposited quantum dot material structures. The effect of temperature leads to different energy gaps which account for the change in lasing wavelength according to Equation 3.1 Chapter 3. The lasing wavelength range of $720nm$ - $745nm$ is obtained by changing the temperature between $150K$ – $300K$ as seen in Figure 6.16. This covers a wavelength range from the required wavelength range mentioned in the motivations in Chapter 1. The decrease in lasing wavelength with the increase of the quantity of deposited quantum dot material, as illustrated if Figure 6.16, for structures grown at $690°C$ is due to the peak gain blue shift when pumping harder with current in order to reach the threshold gain which is about $6cm^{-1}$ for $2mm$ long device and because the internal optical mode loss α_i for these structures increase with the quantity of deposited quantum dot material, as listed in Table 6.2, the peak gain will shift as the injected current increases which will increase the quasi-Fermi level separation and this account for the peak gain shift.

The lasing wavelength from the laser devices along with the peak gain wavelength versus the quantity of deposited quantum dot material for structures grown at temperature of $730^{\circ}C$ taken at room temperature are shown in Figure 6.17. These indicate a linear increase to the lasing wavelength values with the quantity of deposited quantum dot material. The effect of the quantity of deposited quantum dot material on the density of dots leads to a higher number of states which are available for lasing as seen in the absorption spectra. This will allowed the lasing action to take place at lower energy state which account for the increase in lasing wavelength. Moreover, these structures do not contain the very large dot which will reserve the carriers to sustain lasing at low energy state in structure containing high number of states.

6.8 Effect of Deposited Quantum Dot Material

The effect of quantity of deposited quantum dot material on optoelectronic properties is studied in this section. These properties include threshold current density, optical absorption and spontaneous emission for structures with high $730^{\circ}C$ and low $690^{\circ}C$ growth temperature each with different quantity of deposited quantum dot material depending on the measurements obtained from both laser and multisection devices which have been shown in the previous sections. Also use the absorption data to estimate the amount of material contained in the dot and compare this with the amount of material deposited.

6.8.1 Deposited Material in High Growth Temperature

The room temperature threshold current density as a function of quantity of deposited quantum dot material grown at temperature of $730^{\circ}C$ is shown in Figure 6.18. These threshold current density points are taken from Figure 6.8 and indicate a decrease to the threshold current density as the quantity of deposited quantum dot material increases due to higher number of states available for lasing as shown in Figure 6.19 which represents the area under the absorption ground states for different dot size within the structure versus the quantity of deposited quantum dot material obtained from Table 6.1. The number of very large dot, as shown in Figure 6.19, is small and this implies that the effect on the threshold current density is small. The threshold current density for the 3ML structure has the lowest value to date for InP structures grown on GaAs substrate emitting in the

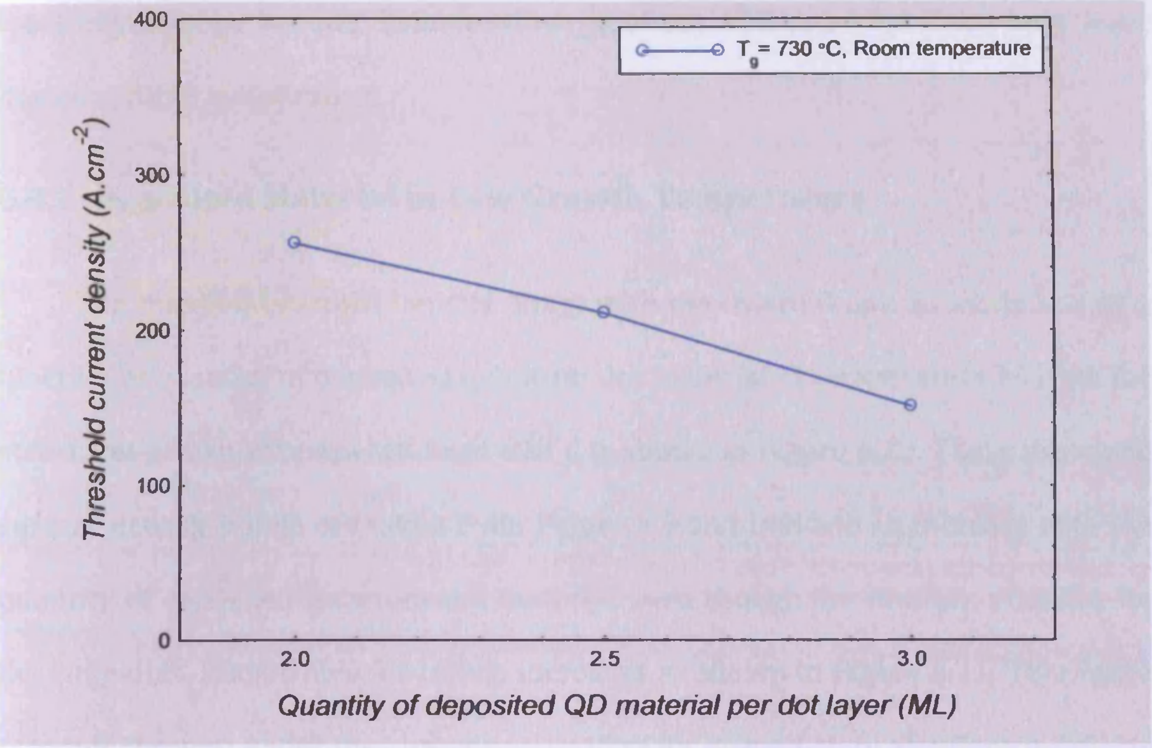

Figure 6.18 *Room temperature threshold current density versus quantity of deposited QD material for structures grown at 730°C.*

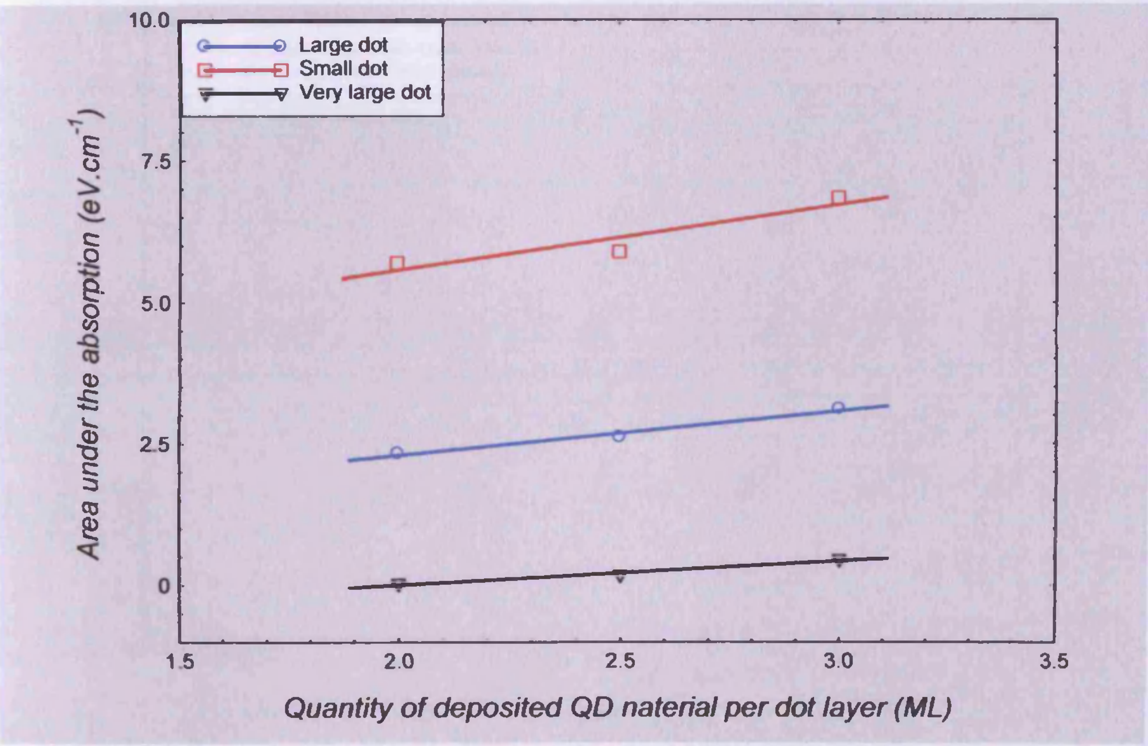

Figure 6.19 *Area under the absorption ground states for different dot size versus quantity of deposited QD material grown at 730°C.*

wavelength range around $730nm$ which is about $150A.cm^{-2}$ for $2mm$ long laser device at room temperature.

6.8.2 Deposited Material in Low Growth Temperature

The threshold current density along with the internal optical mode loss as a function of quantity of deposited quantum dot material at temperature of $150K$ for structures grown at temperature of $690°C$ is shown in Figure 6.20. These threshold current density points are taken from Figure 6.9 and indicate an increase with the quantity of deposited quantum dot material even though the number of states for the large dots, responsible for lasing, increases as shown in Figure 6.21. This figure presents the area under the absorption spectra for ground state of different dot size

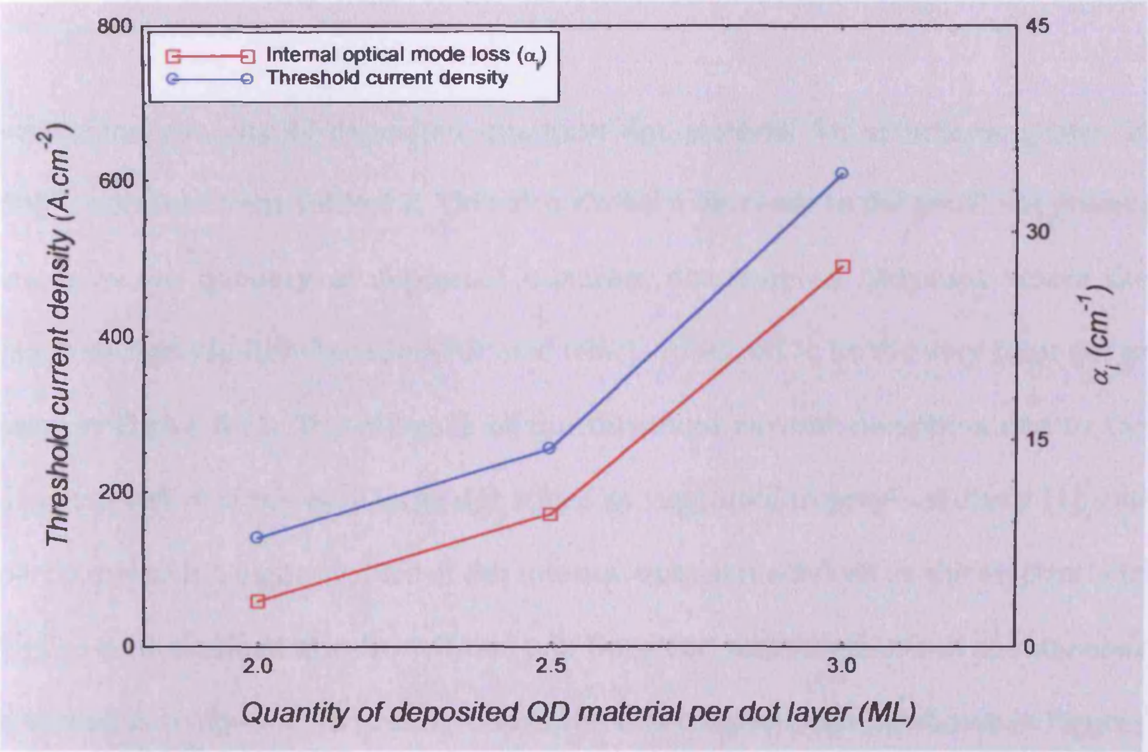

Figure 6.20 *Threshold current density and internal optical mode loss versus quantity of deposited QD material at temperature of 150K for structures grown at 690°C.*

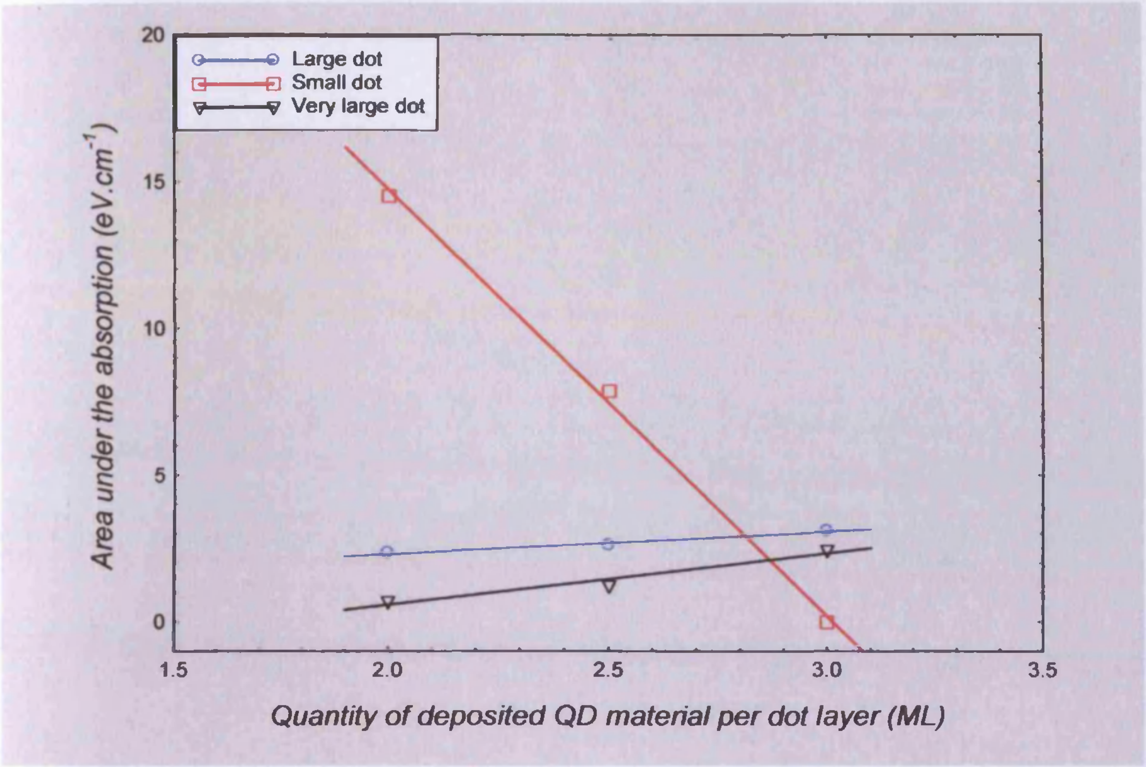

Figure 6.21 *Area under the absorption ground states for different dot size versus quantity of deposited QD material grown at 690°C.*

versus the quantity of deposited quantum dot material for structures grown at 690°C obtained from Table 6.2. This also shows a decrease to the small dot ground states as the quantity of deposited quantum dot material increases where the material starts to form into another size which appeared to be the very large dot as seen in Figure 6.21. The increase of the threshold current density is due to the dramatic effect of the very large dot states as suggested in previous study [1], and partly due to the higher values of the internal optical mode loss as shown clearly in Figure 6.20 obtained also from Table 6.2. However, measurements of spontaneous emission at temperatures greater than 100K and constant current shown in Figures 6.13, 6.14 and 6.15 indicate non-radiative recombination is much higher in

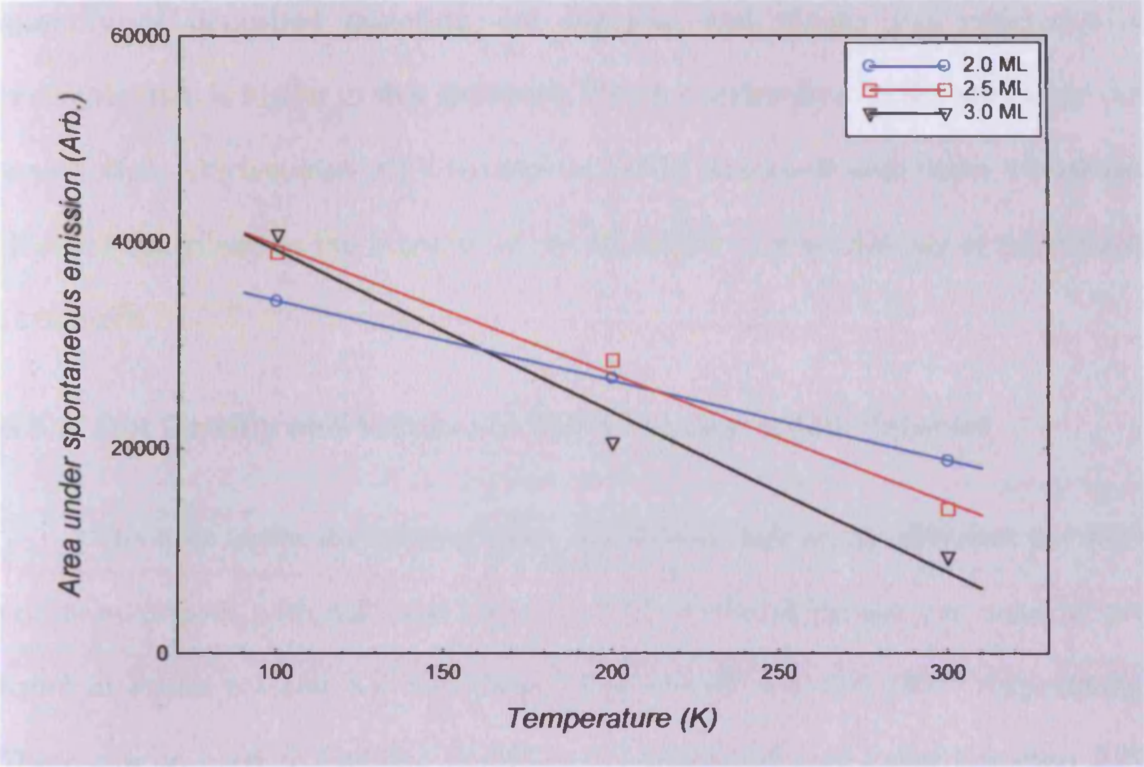

Figure 6.22 *Area under spontaneous emission versus temperature for different quantity of deposited QD material.*

structure with higher quantity of deposited quantum dot material where the very large dots, as believed, also have a number of defects associated with them. At low measurement temperature, structures with high quantity of deposited quantum dot material do not have higher levels of non-radiative recombination and because the carriers at this temperature are localized in the dots and presumably the majority of the very large dots do not contain defects. The areas under the spontaneous emission spectra, which shown in Figures 6.13, 6.14 and 6.15, are calculated and evaluated in Table 6.4. The plot of these areas as a function of temperature for each quantity of deposited quantum dot material is shown in Figure 6.22. These indicate the rate of decrease in radiative recombination is higher in structure with high quantity of deposited quantum dot material and means the non-radiative recombination is higher in this structure. This is consistent with the very large dot assumption, which containing a number of defect associated with them. Therefore, this will contribute to the increase of the threshold current density of the related structures.

6.8.3 Dot Density and Volume in Different Deposited Material

The area under the ground state absorption peak of the different dot sizes within structures with different quantity of deposited quantum dot material are listed in Tables 6.1 and 6.2 for structures grown at 730 and 690°*C* respectively. These can be used to find the density of different dot size using Equation 2.20 Chapter 2. The constant $\sigma_0(E_i)$ are estimated to be about 2.0×10^{-15} $cm^2.eV$ [5], and w_{mod} can be calculated by solving Maxwell's equation for the slab wave guide core system which found to be around 0.434μm and 0.415μm for structures with barrier width of 16 and 8*nm* respectively. As a result of that the density of the different

Quantity of Deposited QD material	N_{Large} (cm^{-2})	N_{Small} (cm^{-2})	$N_{VeryLarge}$ (cm^{-2})
2.0 ML 730°C	$(1.9 \pm 0.1) \times 10^{10}$	$(25.7 \pm 0.1) \times 10^{10}$	$(0.1 \pm 0.1) \times 10^{10}$
2.5 ML 730°C	$(3.1 \pm 0.1) \times 10^{10}$	$(26.6 \pm 0.1) \times 10^{10}$	$(0.8 \pm 0.1) \times 10^{10}$
3.0 ML 730°C	$(3.8 \pm 0.1) \times 10^{10}$	$(30.8 \pm 0.1) \times 10^{10}$	$(2.0 \pm 0.1) \times 10^{10}$
2.0 ML 690°C	$(7.5 \pm 0.1) \times 10^{10}$	$(46.4 \pm 0.1) \times 10^{10}$	$(2.2 \pm 0.1) \times 10^{10}$
2.5 ML 690°C	$(8.4 \pm 0.1) \times 10^{10}$	$(25.2 \pm 0.1) \times 10^{10}$	$(3.9 \pm 0.1) \times 10^{10}$
3.0 ML 690°C	$(9.9 \pm 0.1) \times 10^{10}$	$(0.0 \pm 0.1) \times 10^{10}$	$(7.8 \pm 0.1) \times 10^{10}$

Table 6.5 *Density of different dot size for various quantity of deposited quantum dot material with different barrier widths.*

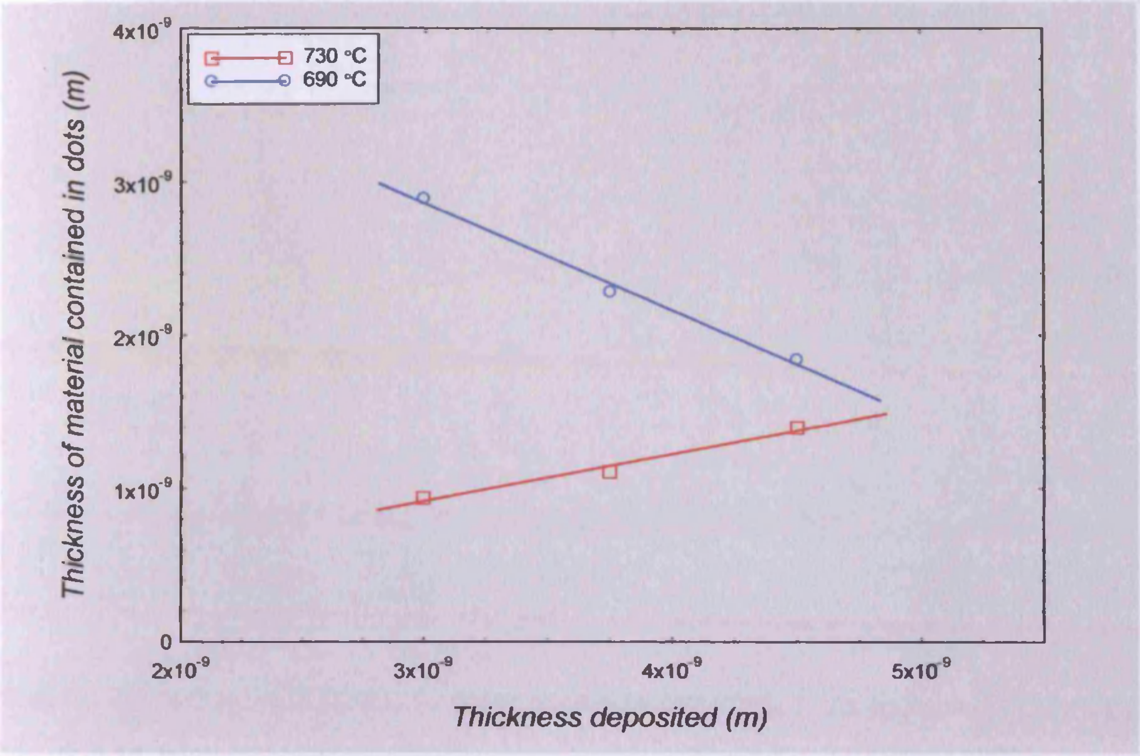

Figure 6.23 *Thickness of dots versus thickness deposited for different quantity of deposited QD material grown at two temperatures.*

dot size for various structures are listed in Table 6.5. These can be used to determine the thickness of the material contained in the dots by multiplying their densities with their volume. The volume can be found by assuming that the dots are formed in the structures as a shape of conical with the same diameter for all dots of 25nm and with different heights for different dots size which are 1, 2 and 3nm for small, large and very large dots respectively [6]. The equation used to find the volume of the dot is seen in Equation 6.1.

$$V_{dot} = \frac{\pi r^2 h}{3} \tag{6.1}$$

The plot of the thickness of the material contained in the dots, summed over all dot

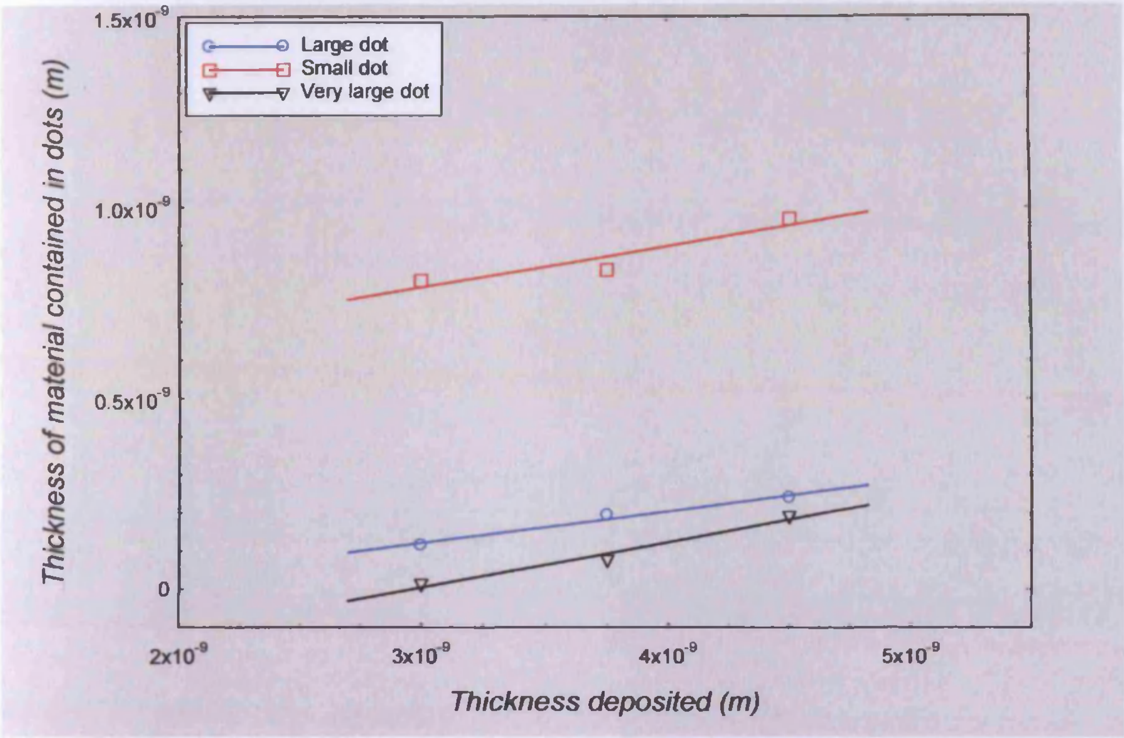

Figure 6.24 *Thickness of dots versus thickness deposited for different dot size grown at 730°C.*

sizes, versus the total thickness of material deposited is shown in Figure 6.23. This was obtained by multiplying the material deposited per dot layer (0.6, 0.75 and 0.9*nm* respectively) by the number of layers (5). This figure indicates an increase to the thickness of the material contained in the dots with the thickness of the quantity of deposited quantum dot material for structures grown at 730°*C*. This due to the equal converting in to different dot size takes place within these structures as shown in Figure 6.24 where all the three dot size increases with the quantity of deposited quantum dot material. On the other hand, Figure 6.23 also show a decrease to the thickness of the material contained in the dots as the thickness of the quantity of deposited quantum dot material increases for structures grown at 690°*C*. This is due to the material loss which takes place in these structures which

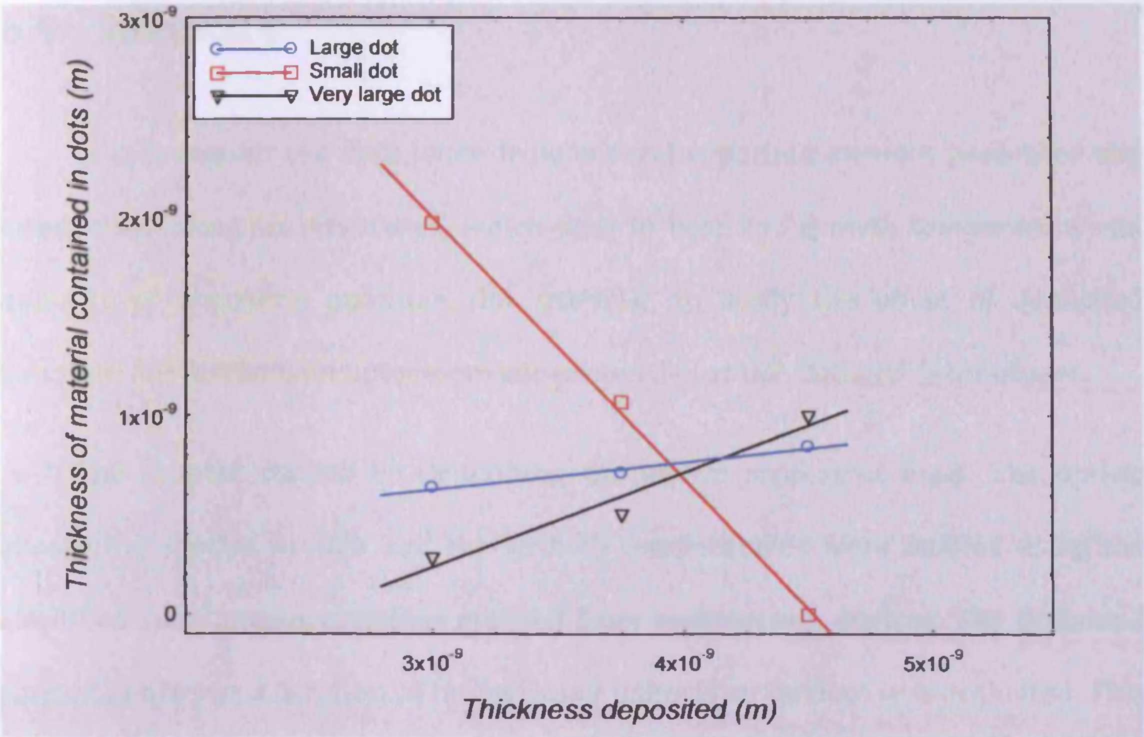

Figure 6.25 *Thickness of dots versus thickness deposited for different dot size grown at 690°C.*

might be responsible for the higher threshold current density in these structure where the material wasted can be converted in to an impurity in these structures which may lead to the increase number of defects in these structures. By looking at the behaviour of each individual dot size for these structures, which shown in Figure 6.25, the loss of the material deposited is coming from the decrease in the small dot as the thickness of deposited material increases. The very large dot shows higher increase in these structures as compared to those grown at 730°*C* where part of the deposited material will start to form more very large dots because the mobility of the atoms to defuse in the barrier surface is low at this growth temperature. This explains the high internal optical mode loss, caused by the scattering light from the very large dot, in structure with high thickness deposited as illustrated in Table 6.2.

6.9 Summary

In this chapter the data taken from several experiments were presented and interpreted using six structures, which vary in both the growth temperature and quantity of deposited quantum dot material, to study the effect of deposited quantum dot material on optoelectronic properties of InP/AlGaInP laser diodes.

The chapter started by describing the device structures used. The optical absorption spectra in high and low growth temperatures were studied using the amplified spontaneous emission emitted from multisection devices. The threshold current density as a function of temperature using laser devices was evaluated. This explains the behaviour of the optical absorption spectra in structures grown at low temperatures especially at low energies. The chapter described the optical gain spectra for structures grown at high temperatures using the amplified spontaneous emission emitted from multisection devices and this verified the threshold current density values by comparing the gain-current relations obtained from both the laser and multisection devices. Afterwards, the chapter described the spontaneous emission spectra for structures grown at low temperatures taken with the same current at different temperatures and this presents the non-radiative recombination in the system which explains the increase of threshold current density at these structures. The lasing wavelength for the studied structures was evaluated. The chapter ended with estimating the amount of material in quantum dot as a function of the amount of deposited quantum dot material.

References

[1] W. Seifert, N. Carlsson, J. Johansson, M-E. Pistol, L. Samuelson, *"In situ growth of nano-structures by metal-organic vapour phase epitaxy"*, Journal of Crystal Growth, 170, pp. 39-46 (1997).

[2] J. Porsche, A. Ruf, M. Geiger, F. Scholz, *"Size Control of self assembled InP/GaInP quantum islands"*, Journal of Crystal Growth, 195, pp. 591- 595 (1998).

[3] M. Grundmann and D. Bimberg, *"Theory of random population for quantum dots"*, Physical Review B, 55, pp.9740-9745 (1997).

[4] P. M. Smowton, J. Lutti, G. M. Lewis, A. B. Krysa, J. S. Roberts and P. A. Houston, *"InP-GaInP quantum-dot lasers emitting between 690-750nm"*, IEEE Journal of Selected Topics in Quantum Electronics, 11, 5, pp.1035- 1040 (2005).

[5] S. W. Osborne, P. Blood, P. M. Smowton, Y. C. Xin, A. Stintz, D. Huffaker and L. F. Lester, *"Optical absorption cross section of quantum dots"*, Journal of Physics Condensed Matter, 16, pp. S3749- S3756 (2004).

[6] James J. Coleman, "Quantum dots: materials, physics and devices" , Short courses, 22nd Annual Meeting of The IEEE Photonics Society, Belek-Antalya, Turkey, 4-8 October (2009).

CHAPTER 7

Conclusions and Further Work

7.1 Conclusions

From all the results and discussions which presented in the last three chapters, the conclusions come from all that are as follow:

- The threshold current density for structures with wide barrier width is lower than that with narrow barrier width because surface of the barriers became smoother in wide barrier width structures which reduces the effect on the other quantum dot layers.
- The number of optical absorption states for large dots decreases and shifted to higher energy as the growth temperature increased.
- The number of very large dot increases as the growth temperature decreased more in structures with narrow barrier width than with wide barrier width.
- The very large dots have a number of defects associated with them which increase the nonradiative recombination in the structure and that will increase the threshold current density.

- The carrier loss from quantum dot to quantum well states increases with growth temperature due to the decreasing number of states available for lasing which play an important role in increasing the threshold current density.

- Optimising threshold current density requires higher number of states, fewer very large dots and less carrier leakage. This appears in structure with 16nm barrier width grown at 710$^{\circ}C$ which is about 170$A.cm^{-2}$.

- The lasing wavelength change by changing the growth temperature take values between 715nm - 745nm which covers a range from the wavelength range required for various application.

- The distinctive behaviour, which is the increase of the threshold current density at low temperatures, in structures grown at high temperature became less pronounced as the growth temperature reduced.

- The carrier distribution in quantum dot states due to inhomogeneous broadening causes this distinctive behaviour and not the carrier loss or the injection level.

- The shift of the lasing wavelength with temperatures agrees with the shift in the absorption edges for different growth temperature structures.

- The number of optical absorption states for large dots increases with the quantity of deposited quantum dot material for structures grown at different temperatures.

- The number of very large and small dots increases with the quantity of deposited material in structures grown at high temperature.
- The number of very large dot shows higher increase with the quantity of deposited material in structures grown at low temperature compared to those grown at high temperature.
- The number of small dot decreases as the quantity of deposited material increase in structures grown at low temperatures. This result in decrease of the total number of dot when the deposited material increases.
- Optimising threshold current density requires more large dots and less very large dots. This appears in structure with 3ML quantity of deposited material grown at $730^{\circ}C$ that has the lowest value to date for InP quantum dot grown on GaAs substrate which is about $150 A.cm^{-2}$.

7.2 Further Work

According to the investigations of the effect of barrier width and growth temperature, it would be interesting to undertake these investigations for different device structures with higher barrier width in order to have more well defined states of the large dot size where the surface of the barrier material will be totally smoothed out. This is preferred for structures grown at low temperatures where the effect from the carrier leakage will be less.

Referring to the studies of the effect of the quantity of deposited quantum dot material, it would be interesting to undertake these studies for structures with more high quantity of deposited quantum dot material especially in structures grown at high temperatures where the number of the very large dot states will be smaller.

Publications List

Conferences :

2009

- Barrier Width and Growth Temperature Effect in InP/AlGaInP Quantum Dot Lasers, M.S. Al-Ghamdi, P.M. Smowton, S. Shutts, P. Blood and A.B. Krysa, 22nd Annual Meeting of the IEEE Photonics Society, Belek-Antalya, Turkey, 4 – 8 October 2009.

- InP/AlGaInP 730nm Quantum Dot Lasers, P.M. Smowton, M.S. Al-Ghamdi, S. Shutts, G.T. Edwards, M. Hutchings and A.B. Krysa, 9th IEEE International Conference on Nanotechnology, Genoa, Italy, 26 – 30 July 2009.

- InP/AlGaInP 730nm Emission Quantum Dot Lasers, M.S. Al-Ghamdi, P.M. Smowton, S. Shutts, M. Hutchings, P. Blood and A.B. Krysa, Conference on Lasers and Electro Optics, Baltimore, Maryland, USA, 31 May – 05 June 2009.

- Optimising Threshold Current Density in InP/AlGaInP Quantum Dot Laser Structures, M.S. Al-Ghamdi, P.M. Smowton, S. Shutts, P. Blood and A.B. Krysa, Semiconductor Integrated Optoelectronics, Cardiff, U.K., 6 – 8 April 2009.

- The Origin of The Temperature Dependence of Threshold Current Density in InP/AlGaInP Quantum Dot Laser Structures, S. Shutts, M.S. Al-Ghamdi, G.T. Edwards P.M. Smowton and A.B. Krysa, Semiconductor Integrated Optoelectronics, Cardiff, U.K., 6 – 8 April 2009.

2008

- InP/AlGaInP Short Wavelength Quantum Dot Lasers, P.M. Smowton, M.S. Al-Ghamdi, S.N. Elliott, G.T. Edwards, P. Blood and A.B. Krysa, International Semiconductor Laser Conference, Sorrento, Italy, 14 - 18 September 2008.

- InP/AlGaInP Quantum Dot Laser structures, P.M. Smowton, M.S. Al-Ghamdi, G.T. Edwards, P. Blood and A.B. Krysa, Conference of the Optics and Photonics, Edinburgh, U.K., 26 – 29 August 2008.

- Effect of Growth Temperature on Threshold Current Density in InP/AlGaInP Quantum Dot Laser Structures, M.S. Al-Ghamdi, P.M. Smowton, G.T. Edwards, P. Blood and A.B. Krysa, International Conference in Nanotechnology, Jeddah, Saudi Arabia, 17 – 19 June 2008.

- The Temperature Dependence of Threshold Current Density in InP/AlGaInP Quantum Dot Laser structures, M.S. Al-Ghamdi, P.M. Smowton, G.T. Edwards, P. Blood and A.B. Krysa, Semiconductor Integrated Optoelectronics, Cardiff, U.K., 31 Marsh – 2 April 2008.

2007

- InP/AlGaInP on GaAs Quantum Dot Lasers, P.M. Smowton, M.S. Al-Ghamdi and A.B. Krysa, Conference on Lasers and Electro Optics, Baltimore, Maryland, USA, 6 – 11 May 2007.

- InP/AlGaInP on GaAs Quantum Dot Lasers, M.S. Al-Ghamdi, P.M. Smowton and A.B. Krysa, Semiconductor Integrated Optoelectronics, Cardiff, U.K., 2 – 4 April 2007.

PAPERS :

2010

- P. M. Smowton, M. S. Al-Ghamdi, S. Shutts, G. Edwards, M. Hutchings and A. B. Krysa, "*Effect of Growth Temperature on InP QD Lasers*", IEEE Photonics Technology Letters, Vol. 22, No. 2, pp. 88-90 (2010).

2009

- M. S. Al-Ghamdi, P. M. Smowton, P. Blood and A. B. Krysa, "*Effect of temperature on threshold current density in InP/AlGaInP quantum dots laser structures*", Int. J. Nano and Biomaterials, Vol. 2, Nos. 1-5, pp. 147-154 (2009).